

Jagiellonian University

Faculty of Physics, Astronomy and Applied Computer Science



DEUTERATED MOLECULES IN STAR-FORMING REGIONS

Magdalena Jastrzębska

DISSERTATION FOR THE DEGREE DOCTOR OF PHILOSOPHY

Promotor: **prof. dr hab. Ryszard Szczerba**

co-promotor: **dr Agata Karska**

"Not all who wander are lost."

J.R.R. Tolkien—*Lord of the Rings*

Rodzicom

Danucie i Antoniemu

*Chciałabym serdecznie podziękować Panu profesorowi Darkowi Lisowi,
bez którego moja rozprawa doktorska by nie powstała.*

*Pani profesor Maryvonne Gerin, która wprowadzała mnie w tajniki redukcji
danych spektroskopowych i której wyjątkowe zaangażowanie przyczyniło się
do powstania moich artykułów.*

*Panu profesorowi dr hab. Ryszardowi Szczerbie za cierpliwość i merytoryczną
pomoc podczas pisania pracy.*

*Paniom dr Agacie Karskiej i dr Nataszy Siódmiak za wnikliwą analizę tekstu.
Rodzinie za wsparcie, Kindze i Stasiowi za twórczą obecność,
a sobie za kosmiczną determinację.*

OŚWIADCZENIE

Ja niżej podpisana Magdalena Jastrzębska (nr indeksu: WFAI-D-150) doktorantka Wydziału Fizyki, Astronomii i Informatyki Stosowanej Uniwersytetu Jagiellońskiego oświadczam, że przedłożona przeze mnie rozprawa doktorska pt. „Deuterated Molecules in Star-Forming Regions” jest oryginalna i przedstawia wyniki badań wykonanych przeze mnie osobiście, pod kierunkiem prof. dr hab. Ryszarda Szczerby. Pracę napisałam samodzielnie.

Oświadczam, że moja rozprawa doktorska została opracowana zgodnie z Ustawą o prawie autorskim i prawach pokrewnych z dnia 4 lutego 1994 r (Dziennik Ustaw 1994 nr 24 poz. 83 z późniejszymi zmianami).

Jestem świadoma, że niezgodność niniejszego oświadczenia z prawdą ujawniona w dowolnym czasie, niezależnie od skutków prawnych wynikających z ww. ustawy, może spowodować unieważnienie stopnia na podstawie tej rozprawy.

.....

Data

.....

Podpis autora pracy

Contents

1	ABSTRACT	2
2	SUMMARY IN POLISH	4
3	SYNOPSIS	6
3.1	A brief history	7
3.2	Infrared and sub-millimetre astronomy	8
3.3	Molecular clouds	11
3.4	Interstellar dust	14
3.5	Star formation	19
3.6	Preface to the included publications	26
	References	30
	Appendices	33

1. Abstract

This document summarises the work done in partial fulfilment of the requirements for the degree Doctor of Philosophy. All my observations analysed in these work were obtained using the Caltech Submillimeter Observatory. This dissertation consists of abstracts in English and Polish, a synopsis in English and three appendices that are peer-reviewed papers published in journals from the JCR list: Acta Astronomica and the Astrophysical Journal. I am the only author of these three publications.

Appendix A contains paper *Observations of HDO in the High-Mass Star Forming Regions*, which was published in 2016 in Acta Astronomica. In this work I analyse my observations of the ground state transition of HDO at 464.925 GHz toward high-mass star forming regions: Sgr B2(N), Sgr B2(M), W33A, W31C, and DR 21(OH). The spectra are modelled together with observations of higher-energy HDO transitions and sub-millimetre dust continuum fluxes from the literature. The Zmuidzinas' spherically symmetric model was used to derive the radial distribution of the HDO abundance in the target sources. The abundance profile is divided into an inner hot core region, with kinetic temperatures higher than 100 K, and a cold outer envelope. This limiting temperature is related to the temperature of water ice evaporation. The HDO abundance with respect of H₂ was derived to be $(0.6\text{--}3.5)\times 10^{-8}$ and $(0.1\text{--}25)\times 10^{-11}$ in the hot inner region and the cold outer envelope, respectively. It clearly shows that evaporation of deuterated water from dust particles increase significantly its abundance in the hot inner region. My analysis showed also that ground-state HDO transition at 464.925 GHz is a very good probe of a cold, outer envelope.

Appendix B contains paper *Analysis of Low Excitation Transition toward the High-mass Star-forming Regions G34.26+0.15, W51e₁/e₂ and W49N*, which was published in 2017 in the Astrophysical Journal. In this work I analyse the two lowest rotational transitions of HDO: $1_{0,1}\text{--}0_{0,0}$ at 464.925 GHz and the $1_{1,0}\text{--}1_{0,1}$ at 509.292 GHz toward three high-mass star forming regions: G34.26+0.15, W51e₁/e₂ and W49N. For the first time, the transition of HDO at 509.292 GHz is observed from the ground. The spectra are modelled, together with observations of higher-energy HDO transitions, as well as sub-millimetre dust continuum fluxes from the literature, using the radiative transfer code of Zmuidzinas to derive the radial distribution of the HDO abundance in the target sources. Similarly as in the first paper, the abundance profile is divided into an inner hot core region, with kinetic temperatures higher than 100 K, and a cold outer envelope with lower kinetic temperatures. The derived HDO abundance with respect of H₂ is $(0.3\text{--}3.7)\times 10^{-8}$ in the hot inner region ($T > 100\text{K}$) and $(7.0\text{--}10.0)\times 10^{-11}$ in the cold outer

envelope. I also used two H_2^{18}O fundamental transitions to constrain the H_2O abundances in the outer envelopes. The $\text{HDO}/\text{H}_2\text{O}$ ratios in these cold regions are found to be $(1.8\text{--}3.1)\times 10^{-3}$ and are consequently higher than in the hot inner regions of these sources, and much larger than the cosmic D/H ratio of about 10^{-5} .

Appendix C contains *Deuterated molecules in Star-Forming Regions*, which was published in 2018 in *Acta Astronomica*. In this paper I show the spatial distribution of deuterated molecules in several nearby low-mass star-forming regions, traced by the DCO^+ (3–2) emission. These images suggest that the deuterated material is often displaced with respect to the highest column density regions, as traced by sub-millimetre dust continuum emission and sometimes appears to be associated with the low-velocity CO (2–1) emission, tracing outflow activity. High deuterated levels in isolated prestellar core can be explained by gas-phase or grain surface chemistry in dense, cold regions, where abundant gas-phase species are frozen onto dust grains. However, I argue that an alternative mechanism may operate in dense gas in the vicinity of embedded young stellar objects, where slow C-type shocks associated with molecular outflow may produce conditions favourable for deuterium fractionation either by increasing the gas volume density in the post-shock gas and thus shortening the depletion and gas-phase reaction time-scale, or by evaporating grain mantle ices.

2. Summary in Polish

Niniejszy dokument jest rozprawą doktorską realizowaną w tak zwanym nowym trybie, gdzie forma klasycznej tezy została zastąpiona opublikowanymi pracami recenzowanymi, uzupełnionymi streszczeniami w języku angielskim i polskim oraz obszernym opisem w języku angielskim. W skład rozprawy wchodzi trzy załączniki, które są recenzowanymi pracami opublikowanymi w czasopismach z listy JCR: *Acta Astronomica* i *Astrophysical Journal*. Jestem jedynym autorem tych trzech publikacji. Wszystkie moje obserwacje analizowane w tych pracach uzyskano za pomocą teleskopu Caltech Submillimeter Observatory.

Appendix A zawiera artykuł *Observations of HDO in the High-Mass Star Forming Regions*, który został opublikowany w 2016 roku w *Acta Astronomica*. W tej pracy analizuję moje obserwacje najniższego przejścia rotacyjnego HDO na 464.925 GHz w kierunku regionów formowania się gwiazd masywnych: Sgr B2 (N), Sgr B2 (M), W33A, W31C i DR 21 (OH). Przejścia te są modelowane razem z przejściami HDO z poziomów o wyższej energii oraz kontinuum pyłu znalezionymi w literaturze. Do oszacowania rozkładu przestrzennego obfitości HDO w tych źródłach został wykorzystany sferycznie symetryczny model Zmuidzinasa. Modelowane obszary zostały podzielone na wewnętrzny obszar gorącego rdzenia z temperaturami kinetycznymi wyższymi niż 100 K i zimną otoczkę zewnętrzną. Ta graniczna temperatura jest związana z temperaturą odparowania lodu wodnego. Otrzymana obfitość HDO w stosunku do H_2 wyniosła odpowiednio $(0.6-3.5) \times 10^{-8}$ i $(0.1-25.0) \times 10^{-11}$ w gorącym obszarze wewnętrznym i zimnej zewnętrznej otoczce. Wyraźnie widać, że parowanie HDO z cząstek pyłu znacznie zwiększa jego obfitość w gorącym obszarze wewnętrznym. Moja analiza wykazała, że przejście HDO na 464.925 GHz jest bardzo użytecznym narzędziem do badania struktury i warunków w zewnętrznej otoczce.

Appendix B zawiera artykuł *Analysis of Low Excitation Transition toward the High-mass Star-forming Regions G34.26+0.15, W51e₁/e₂ and W49N*, który został opublikowany w 2017 roku w *Astrophysical Journal*. W tej pracy analizuję dwa najniższe przejścia rotacyjne HDO: $1_{0,1}-0_{0,0}$ na 464.925 GHz i $1_{1,0}-1_{0,1}$ na 509.292 GHz w kierunku trzech regionów gwiazdotwórczych o dużej masie: G34.26+0.15, W51e₁/e₂ i W49N. Do celów tej pracy wykorzystano po raz pierwszy zaobserwowane z Ziemi przejście HDO na 509.292 GHz. Podobnie jak w pierwszej pracy, widma były modelowane wraz z obserwacjami przejść HDO z poziomów o wyższej energii oraz sub-milimetrowymi obserwacjami kontinuum pyłu znalezionymi w literaturze. Wykorzystując model transferu promieniowania Zmuidzinasa uzyskałam przestrzenny rozkład obfitości HDO w badanych źródłach. Podobnie jak w pierwszym artykule, modelowane otoczki zostały podzielone na wewnętrzny obszar gorącego rdzenia z temperaturami kinety-

cznymi wyższymi niż 100 K i zimną otoczką zewnętrzną o niższych temperaturach kinetycznych. Uzyskana obfitość HDO w porównaniu z H_2 wynosi $(0.3-3.7)\times 10^{-8}$ w gorącym obszarze wewnętrznym i $(7.0-10.0)\times 10^{-11}$ w zimnej zewnętrznej otoczce. W pracy wykorzystałam również dwa podstawowe przejścia $H_2^{18}O$, aby wyznaczyć obfitość H_2O w zewnętrznych obszarach. Stosunki HDO/ H_2O w tych zimnych otoczkach wynoszą $(1.8-3.1)\times 10^{-3}$ i są znacząco wyższe niż w gorących wewnętrznych obszarach tych źródeł, a także znacznie większe niż kosmiczny stosunek D/H, który wynosi około 10^{-5} .

Appendix C zawiera artykuł *Deuterated Molecule in Star-Forming Regions*, który został opublikowany w 2018 roku w Acta Astronomica. W tym artykule analizuję rozkład przestrzenny zdeuteryzowanych molekuł w kilku pobliskich obszarach tworzących gwiazdy o małych masach, w oparciu o emisję DCO^+ (3–2). Otrzymane obrazy pokazują, że zdeuteryzowany materiał jest często przemieszczony w stosunku do obszarów o najwyższych gęstościach kolumnowych próbkowanych przez sub-milimetrową emisję pyłu, a ponadto wydaje się, że niekiedy koreluje z wpływami widocznymi w linii CO (2–1). Proces deuteracji zachodzi w gęstych i chłodnych przedgwiazdowych jądrach zarówno w fazie gazowej jak i na powierzchni ziaren. Jednak w pracy argumentuję, że możliwy jest alternatywny mechanizm wyjaśniający wysoki poziom deuteracji. W sąsiedztwie młodych gwiazd, będących źródłem wpływów molekularnych, towarzyszące im wolne szoki typu C mogą istotnie zwiększyć gęstość gazu i skrócić czas wymrażania się molekuł z fazy gazowej lub przyczynić się do odparowania molekuł z deuterem z powierzchni ziaren pyłu.

3. Synopsis

This thesis is based on the following publications:

I. *Observations of HDO in the High-Mass Star Forming Regions*

Magda Kulczak-Jastrzębska

Acta Astronomica 66, 313 (2016)

II. *Analysis of Low Excitation HDO Transitions toward the High-mass Star-forming Regions G34.26+0.15, W51e₁/e₂, and W49N*

Magda Kulczak-Jastrzębska

Astrophysical Journal 835, 121 (2017)

III. *Deuterated Molecules in Star-Forming Regions*

Magda Kulczak-Jastrzębska

Acta Astronomica 68, 125 (2018)

I have also participated in the following publications, not included in the thesis.

1. *The tight correlation of CCH, and c-C₃H₂ in diffuse and translucent clouds*

Maryvonne Gerin, Maja Kazmierczak, Magda Jastrzebska, et al.

Astronomy & Astrophysics 525, 116 (2011)

2. *A Comparison of c-C₃H₂ and l-C₃H₂ in the Spiral Arm Clouds*

Magda Kulczak-Jastrzębska, Darek Lis, Maryvonne Gerin

Acta Astronomica 62, 313 (2012)

3.1. *A brief history*

The existence of interstellar matter was first established around the beginning of the 20th century. In 1904, Johannes Hartmann (1865-1936) noted stationary absorption lines of the CaII ion in the spectrum of the binary star δ Orionis: all of the normal absorptions arising in the atmospheres of these stars shifted periodically in wavelength owing to the Doppler effect from orbital motion. Hartmann suggested that he might be seeing absorptions in a cloud of ionised calcium lying between us and that star system. In 1929, Otto Struve (1897-1963) showed a systematic increase in the strength of sharp interstellar absorption lines in stellar spectra with distance. It follows that the atoms responsible for their formation are not related to stars, but fill the space between them, which confirms Hartmann's conclusions. In the 1930s, Robert J. Trumpler (1886-1956) found that the brightness of the more distant open clusters was lower than expected, and the stars appeared redder (the Trumpler Effect). This was inferred to be a result of the absorption and scattering of starlight by small solid particles in the intervening interstellar medium (ISM). By the late 1930s, the existence of an ISM was generally accepted, but it was viewed as largely homogeneous and diffuse, spreading through the space with nearly constant density. High-resolution spectroscopy of the so-called "stationary" lines revealed that they had very complex structures, resolving into many narrower line components with different radial velocities. This led to the recognition that the ISM was clumpy and arranged into clouds. The year 1930 accordingly marked the approximate starting point of the study of interstellar matter as a new branch of astronomy.

For nearly 30 years after Hartmann's discovery of interstellar absorption lines the atomic species CaII and NaI were the only identified components of interstellar gas. Then, Merrill (1934) noted four new diffuse interstellar absorptions. A number of other diffuse and sharp absorption features were found during the next few years: cyanide CN (McKellar 1940), the methyladine radical¹ CH and its ion CH⁺ (Adams 1939, Dunham 1937). The next major advance in spectroscopy of interstellar gas resulted from the Dutch astronomer

¹ In chemistry a radical is an atom, molecule, or ion that has an unpaired valence electron. With some exceptions, these unpaired electrons make free radicals highly chemically reactive.

van der Hulst's prediction of a radio-frequency transition between the hyperfine sub-levels² of ground state of atomic hydrogen. Observational confirmation of this line emission of interstellar H at 21 cm wavelength was obtained by Ewen and Purcell (1951) and six weeks later by Muller and Oort. In the next decade, radio-astronomical techniques extended to the molecular domain with the discovery of interstellar hydroxyl radical OH ($\lambda = 18$ cm; Barrett, Meeks & Weinreb 1963). In 1968 Cheung (Cheung et al. 1968) discovered the first polyatomic molecule NH₃ ($\lambda = 1.25$ cm) and a year later formaldehyde (HCHO) was identified by Snyder and colleagues (Snyder et al. 1969). The rapid development of radioastronomy at high frequencies led to a lot of molecular identifications in the 1970s. In particular, the identification of mm-wavelength emission line of ¹²CO ($J = 1-0$, $\lambda = 2.6$ mm; Wilson, Penzias & Jefferts 1970) in the Orion Nebula provided a widespread tracer of molecular gas and led to discovery of giant molecular clouds. Using CO as a tracer, in 1977 Solomon, Sanders and Scoville identified about 3000 Giant Molecular Clouds (GMCs) in the Galaxy, with dimension 10 - 80 pc (30 - 250 ly). The most abundant and famous molecular clouds in our Galaxy are the Orion Molecular Cloud and Sagittarius B2 Cloud near the center of the Milky Way. With the introduction of telescope and receiver systems capable of observing in the 100 - 300 GHz frequency range (corresponding to wavelengths of 3 - 1 mm), many molecules with increasingly complex structure were detected in a rapid pace. The reason for this rapid development is the richness of molecular rotational transitions with energies corresponding to this wavelength range, coupled with the cold excitation conditions of interstellar space as depicted by McKellar and Adams 40 years earlier.

3.2. Infrared and sub-millimetre astronomy

Because the star forming process occurs behind so much intervening dusty material, visible-light telescopes cannot see what is happening. The visual magnitudes of extinction ($A_V = 10$) corresponds to only 1 magnitude of extinction at $2.2 \mu\text{m}$ and much less in thermal infrared (3 - $30 \mu\text{m}$). A region which is completely opaque optically may be

² Hyperfine structure refers to small shifts and splittings in the energy levels of atoms, ions and molecules, due to interaction between the state of the nucleus and the state of the electron clouds.

relatively transparent at longer wavelengths. So the infrared and sub-millimetre ranges are important simply to look deeper into the clouds and observe the processes taking place in the early life of a star. The millimetre-wave range is especially useful for studying the characteristics of enormous cold gas clouds in which stars form. In these cold clouds ($T \sim 20$ K), chemical reactions occur, producing a plenty of molecules. The molecules emit radio waves in the millimetre range and studying these species tells astronomers about the physical conditions within clouds associated with formation of stars, and about chemical reactions peculiar to astronomical environments that cannot be duplicated in laboratories on earth. Millimetre emission from many species can be mapped across an extended cloud with high spectral resolution, but modest spatial resolution, but some species without permanent dipole moments³ cannot be detected. However, these species, as well as one with permanent dipoles can be detected through their ro-vibrational transitions in the infrared, if substantial column densities lie in front of a source of infrared continuum. Millimetre emission spectroscopy and infrared absorption spectroscopy are complementary probes of molecular clouds.

Vibrational absorption of molecules such as H_2O , O_2 , CO_2 , N_2O , CH_4 , and so on remove much of the celestial infrared radiations and prevent them from reaching the Earth (Fig.1). However, there exist a number of atmospheric windows where the opacity is relatively low through which observations can be carried out from the ground. In the near infrared, observations are carried out through the J ($1.1 - 1.3\mu m$), H ($1.5 - 1.8\mu m$), K ($2 - 2.4\mu m$), L ($3.2 - 3.8\mu m$), M ($4.6 - 5\mu m$), N ($8 - 13\mu m$), and Q ($16 - 24\mu m$) band windows. In the sub-mm region, at low elevation, ambient atmospheric water vapour will absorb any incoming sub-millimetre photons before they can reach the telescope. At higher elevations, however, the water content decreases substantially. By minimising the atmospheric water vapour, one improves the transparency of the atmosphere and makes astronomical observations possible. It is for this reason that infrared and sub-millimetre observatories are built as high as possible and by being above some of the atmosphere, the radiation

³ Permanent dipoles occur when two atoms in a molecule have substantially different electronegativity. One atom attracts electrons more than another, becoming more negative, while the other atom becomes more positive. A molecule with a permanent dipole moment is called a polar molecule.

from astronomical sources is much less attenuated.

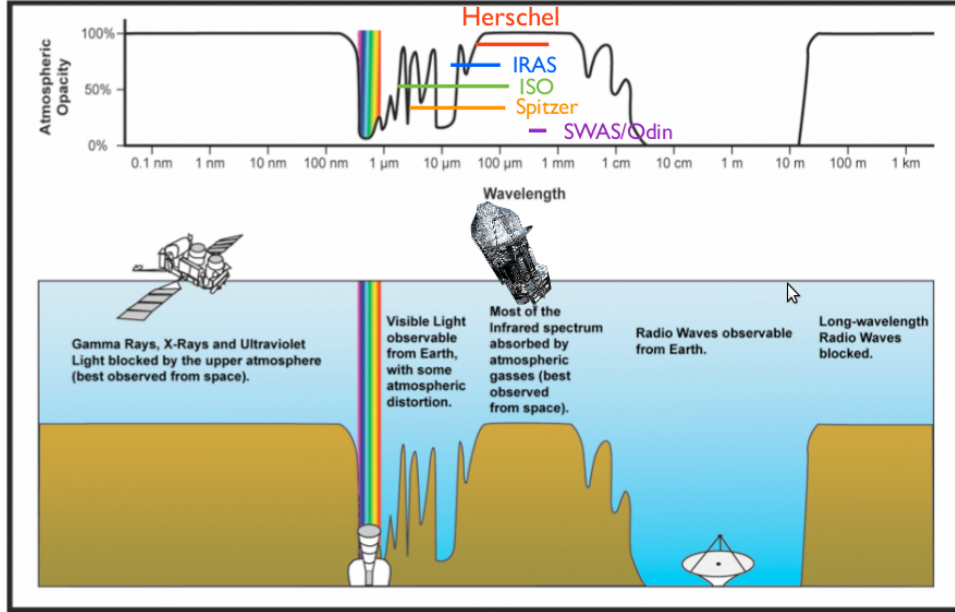


Figure 1. Atmospheric windows. Two main atmospheric windows are seen: the optical and radio window. There is a partial transmission between 1 and 25 μm .

Radio telescopes equipped with high-frequency receivers and spectrometers were the major impetus for the development of molecular astronomy. Increasing size of the dishes coupled with decreasing noise temperatures of the receivers led to better sensitivity needed to detect weak signals. Better surface accuracy of the dishes and the developments of solid-state junctions operating at higher frequencies allow observational coverage from mm to sub-mm wavelengths.

All my observations presented in this thesis were obtained using the **Caltech Sub-millimeter Observatory (CSO) telescope**. The Caltech Sub-Millimeter Observatory was the first sub-millimetre telescope located at Mauna Kea (4200 m). It had a 10.4-m Leighton Telescope (Fig. 2) and was equipped with a variety of sub-millimetre wave receivers operating between λ : 300 to 1000 μm . CSO began operations in 1988, and was closed in September 2015.



Figure 2. Caltech Sub-millimeter Observatory, (*credit*: CSO Home page).

3.3. *Molecular clouds*

In 1784 William Herschel's (1738 - 1822) sister Caroline (1750 - 1848) observed "a hole in the heavens". Herschel reported her discovery a year later and for the next century astronomers debated about the nature of these dark starless areas. It was 1919 when Edward Emerson Barnard (1857 - 1923) published the first modern and systematic photographic survey, the "Dark Marking of the Sky". Thanks to the rich photographic documentation containing 182 such dark places Barnard concluded that these were not regions empty of stars but rather concentration of dark, obscuring matter that blocked out the light of all more distant stars. These regions were called dark nebulae (nebula is Latin word for cloud). Bart J. Bok (1906 - 1983) was the first person who noticed relation between the dark clouds and the formation of stars. He suggested that isolated dark clouds, known as Barnard objects or Bok globules, could be the sites of star birth (Bok and Reilly 1947). Bok globules are probably the nearest and simplest structures in the interstellar medium. Optically they appear as dark, roundish patches against the stellar background and have well defined edges and high visual extinction. The observational evidence for star formation in Bok globules was late in coming. From an analysis of the IRAS data of 248 Bok globules, Yun and Clemens (1990) found that 23% of them are associated with IRAS point sources. A comparison of these source with field sources indicates that star inside the globules are young stellar objects.

The discovery of molecules in space and first of all H_2 as the dominant constituent of Dark Clouds (Weinreb et al. 1963, Wilson et al. 1970) caused that they were also called Molecular Clouds. The terms Molecular Cloud and Dark Cloud are often used interchangeably. Molecular clouds are dark not because they contain molecular hydrogen, but because their component is also a population of tiny solids (dust grains). The dust grains absorb the optical starlight, and lead to high visual extinction ($A_v > 1^m$). Bergin & Tafalla (2007) proposed to use the term Cold Dark Clouds to refer to those molecular clouds that are close enough (< 500 pc) to be seen in silhouette against the background galactic starlight. These clouds are observed to be forming low mass stars either in isolation or in small compact groups and have gas temperatures $\sim 10\text{--}20$ K. Molecular clouds are not uniform but highly structured with large variations in density. A common feature of molecular clouds is that they show a partly hierarchical structure, with smaller subunits appearing within larger ones when observed with increasing spatial resolution (Table 1). Dark clouds stand in contrast to diffuse clouds in the Milky Way, which contain molecular material but are not forming stars. At the other end of the spectrum of galactic star formation lie the more distant and more massive Giant Molecular Clouds that form rich stellar clusters and contain embedded massive stars that heat the surrounding gas to temperatures > 20 K.

Table 1. Properties of Dark Clouds, Clumps, and Cores (adapted from Bergin & Tafalla, 2007)

	Clouds ^a	Clumps ^b	Cores ^c
Mass (M_\odot)	$10^3\text{--}10^4$	50–500	0.5–5
Size (pc)	2–15	0.3–3	0.03–0.2
Mean density (cm^{-3})	50–500	$10^3\text{--}10^4$	$10^4\text{--}10^5$
Velocity extent (km s^{-1})	2–5	0.3–3	0.1–0.3
Gas temperature (K)	10	10–20	8–12
Examples	Taurus, Oph	B213, L1709	L1544, B68

^(a) Cambre sy (1999).

^(b) Williams et al. (1994).

^(c) Caselli et al. (2002a).

Diffuse Clouds

Diffuse stellar clouds are regions of relatively low density $n \sim 50 \text{ cm}^{-3}$ and temperature $T \sim 80 \text{ K}$. Typical sizes and masses of diffuse clouds are $\sim 10 \text{ pc}$ and $\sim 500 M_{\odot}$. With total hydrogen column densities of $N_H \sim 10^{21} \text{ cm}^{-2}$ they are quite transparent to the ambient interstellar radiation field. Hence, UV photons play an important role in their physics and chemistry. In addition, these low column densities and extinction allow sensitive absorption line studies against bright stellar or extragalactic background sources in the UV, visible, infrared, and millimetre wavelengths regions (Snow & McCall 2006). Molecular hydrogen can be observed directly in diffuse clouds through the Lyman and Werner bands in the UV. The observations also reveal significant rotational and vibrational excitation of H_2 . Diffuse clouds show a wide variety of simple species (e.g., CO , C_2H , C_3H_2 , H_2CO), radicals (e.g., C_2 , CH , CN , CH^+), and ions (e.g., HCS^+ , C^+ , H_3^+). The most abundant molecular species, CO , locks up only 1% of the elemental carbon.

Giant Molecular Clouds

The CO J=1-0 transition at 2.6 mm is commonly used as a tracer of molecular gas in the Galaxy. This simple, stable diatomic molecule of carbon monoxide has played an essential role in the study of molecular gas in space generally because H_2 itself, devoid of a permanent electric dipole moment, is almost impossible to observe directly in the cold, generally obscured interstellar regions where molecules form and survive. The CO emission lines are produced by collisions with H_2 molecules. In general, the higher the density of H_2 in particular region, the higher the so-called velocity integrated CO emission intensity W_{CO} . Usefully, the column density of molecular hydrogen $N(\text{H}_2)$ along a specific line of sight can be expressed as the approximate constant ratio: $N(\text{H}_2)/W_{\text{CO}} \approx 2 \times 10^{20}$ (e.g. Gerin and Liszt 2017) molecules per square centimetre per Kelvin per km/s. The integrated intensity W_{CO} is expressed as the brightness temperature (in Kelvin) integrated over the radial velocity (km/s) variation encompassed by the emission line profile.

Surveys in this line have shown that much molecular gas in the Milky Way is localised in discrete Giant Molecular Clouds with typical sizes of 40 pc, masses of $4 \times 10^5 M_{\odot}$,

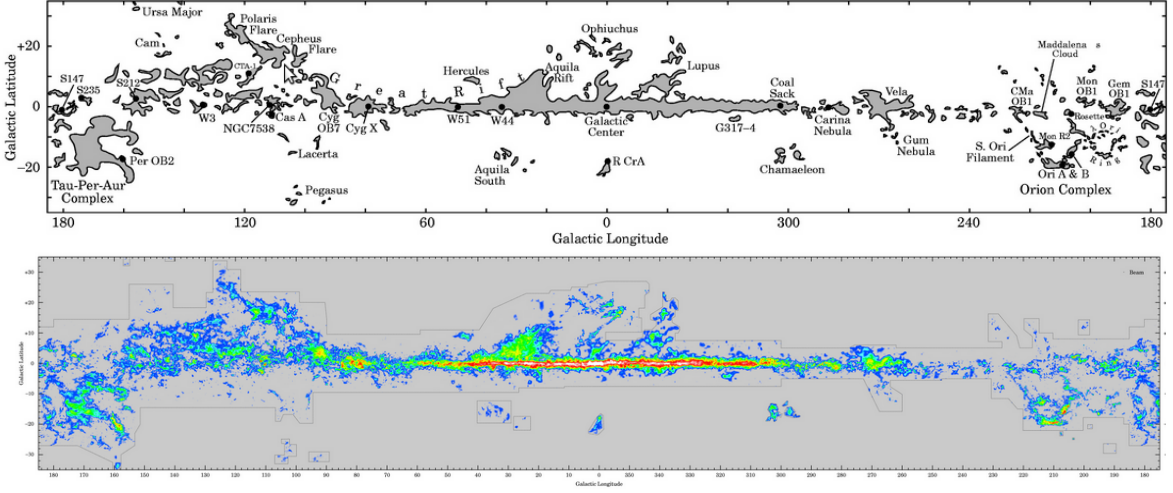


Figure 3. A composite CO map of many individual surveys obtained throughout the last decades containing 488,000 spectra. The horizontal scale is ± 180 deg Galactic longitude, the vertical scale is ± 30 deg. Galactic latitude. *credit:* from Dame et al. (2007)

densities of $\sim 150 \text{ cm}^{-3}$, and temperatures of 10 K (Dame et al. 1987). They form so-called Galactic Molecular Ring, an important region for the formation of massive stars at galactocentric distance of 5 kpc. Collected detailed information on individual molecular clouds clearly display the main structural features of the molecular Galaxy (Fig. 3).

3.4. Interstellar dust

An important part of interstellar matter is the interstellar dust. This consists of microscopic solid particles, formed in the mass-losing envelopes of red giant stars, novae, and supernovae, and blown throughout the interstellar space by the winds in which they condense. Stellar winds contain oxides of aluminium, silicates, and crystalline or amorphous carbon. Silicates are the most common form of minerals, they consist of silica tetrahedras (SiO_4 , i.e. 4 oxygen atoms around a silicon atom) which are combined with metal cations, such as Mg_2^+ or Fe_2^+ in a lattice structure. Crystalline silicates have ordered lattice structures, the tetrahedras can share their oxygen atoms with other tetrahedras. Crystalline silicates are: olivines: $(\text{Mg, Fe, ...})_2\text{SiO}_4$, pyroxenes: $(\text{Mg, Fe, ...})\text{SiO}_3$ or quartz:

SiO₂. Amorphous silicates have unordered structures, the number of shared oxygen-atoms may vary for each silica anion. Absorption features in the spectra are used to constrain the chemical composition of refractory grain. For example, the strong 9.7 and 18 μm absorption bands are attributed to amorphous silicate grains, while the 2175 \AA absorption feature is attributed to graphite.

The characteristic size of a dust grain is $\sim 0.1\mu\text{m}$. However, dust particles are very rare by number: on average there is only one of them for every 10^{12} hydrogen atoms in the gas, and as fraction of the interstellar mass is concerned, the grains account only for about 1 % of the total mass. On the other hand, large fractions of all heavy elements in interstellar space are locked up in this solids most of the time.

These particles are very effective at absorbing and scattering (scattering means reflecting in all directions) of UV and optical light. The combined effect of absorption and scattering of starlight is called *extinction*. In general, the extinction depends inversely on wavelength, which means that blue light is extinguished more severely than red light. This causes the effect of *reddening* of starlight (the Trumpler Effect). Observations (Mathis 1996), numerical simulations (Ossenkopf 1993; Ormel et al. 2009) and analyses of Solar System bodies have provided the evidence that interstellar grain particles have highly fluffy and porous structures. Furthermore, it is believed that dust coagulation, increasing with total density induces an increase of the grain sizes, especially when they are covered by ices: solidified gases of such molecules as H₂O, CO₂, CO, CH₄, NH₃, etc. (Ormel et al. 2009).

Gas phase particles approaching a surface can be bonded either via a van der Waals interaction (physisorption - with energies approximately 0.01 eV) at large distances or via an interaction in which a chemical bond is formed (chemisorption - with energies of a few eV) at shorter scales (Tielens & Allamandola 1987, Tielens 2005). For instance, in molecular clouds, H₂ forms only on grain surfaces due to chemisorption, while ices form via physisorption. It is believed that most solid molecules observed in interstellar ices are formed thanks to the mobility of light particles (H, D, H₂, HD, D₂) on the surface. Interstellar grains provide a surface on which accreted species can meet and react and to which they can donate excess reaction energy (Tielens, 2005). Grain-surface chemistry is thus governed by the accretion rate, which sets the overall time scale for the process,

and the surface migration rate, which governs the reaction network. Generally, reactive species have to wait for a (mobile) co-reactant to arrive.

Finally, H_2 coverage of grain plays a key role in the binding energy of light species with the surface because interactions with an H_2 molecule are much weaker than with water: the binding energy of light atoms (H, D) on H_2 substrate is approximately 10 times smaller than with H_2O (Pierre et al. 1985). Molecules show higher binding energy than atoms, induced by their higher mass and the formation of new types of interactions.

The interstellar ices are mainly composed of water, but contain other compounds, such as carbon dioxide (CO_2), carbon monoxide (CO), or methanol (CH_3OH) in significant quantities. Observational studies of ices and comparison with laboratory spectra have shown that ice composition depends on the physical conditions inside molecular clouds. For example, interstellar water ice is observed in the Taurus molecular cloud above a visual extinction threshold of 3.2 mag (Whittet et al. 1988). The linear increase of its column density with A_V suggests that water starts to form already in translucent regions (Whittet et al. 2011). The column density of solid CO_2 increases linearly with the column density of water ice in dark clouds (Whittet et al. 2007), suggesting that most CO_2 forms in parallel with H_2O at low visual extinctions. Solid CO is also observed, but with higher visual extinction above a threshold of $A_V > 8\text{--}9$ mag, and is present in several ice mixtures. Finally, methanol is observed above a threshold of $A_V \sim 15$ mag (Whittet et al. 2011) and most methanol is likely formed after the formation of water and CO_2 , when CO is already located in the ices. Figure 4 presents a cartoon picture depicting the ice composition deduced from observations.

Formation and deuteration of water ice

As noted above, water is main constituent of interstellar ices. Tielens & Hagen (1982) proposed a chemical network for formation of H_2O by sequential hydrogenation of atomic and molecular oxygen. The simplest formation pathway toward solid water is sequential hydrogenation of atomic oxygen:



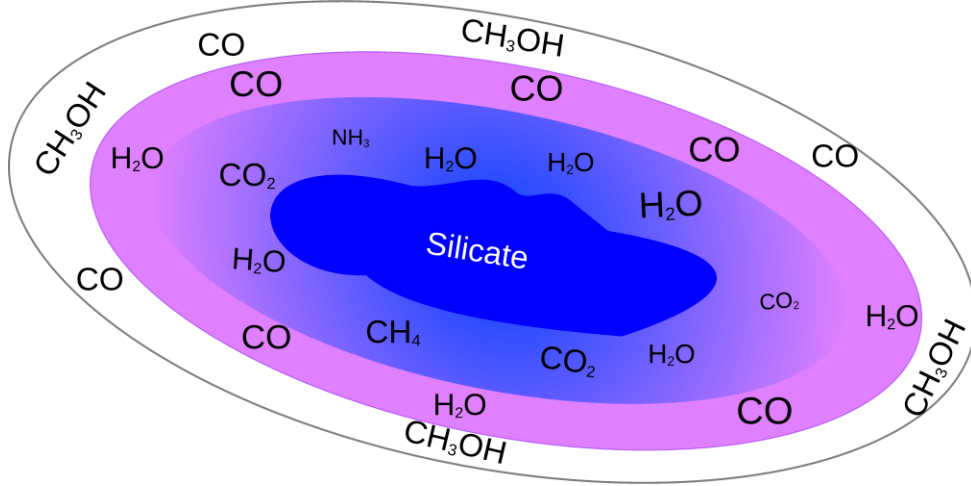


Figure 4. Cartoon of a typical interstellar ice deduced from infrared observations: the blue component refers to the polar water-rich mixture formed at low visual extinction, the violet component shows the CO-rich ice either mixed with CO or pure CO ice, the white ice is the outer part of grain mantles probably composed of CO and methanol.

Deuterated isotopologues are also thought to form via similar reactions, involving OH, OD, H and D. Water and its deuterated isotopologues: HDO and D₂O can also be formed from molecular oxygen, either directly coming from the gas phase or formed on interstellar grains following the reactions channels:



These pathway have been experimentally demonstrated by Miyauchi et al. (2008), Ioppolo et al. (2008) and Cuppen et al. (2010) at very low temperatures (~ 10 K). Cuppen & Herbst (2007) have claimed that molecular hydrogen plays a key role in the formation of water ice in molecular clouds. When hydrogen is mostly in its molecular form, ~ 70 % of all of the water is formed by the reaction:



Oba et al. (2012) experimentally showed that water can indeed be formed from molecular hydrogen in this way at low temperatures.

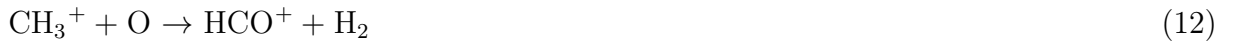
In cold molecular clouds much of the hydrogen is molecular, the temperature is low, and UV radiation from the interstellar radiation field is largely excluded by the shielding effects of dust. The main driver of gas phase chemistry in such clouds is the ion H_3^+ , which initiates a rich and rapid chemistry based on proton donation. Once H_2 is formed on grains and desorbed into interstellar gas, it can be ionised by reactions with cosmic rays. The dominant process is single cosmic ray ionisation: $\text{H}_2 + \text{c.r.} \rightarrow \text{H}_2^+ + \text{e}^- + \text{c.r.}$. The H_2^+ ion produced is reactive with ubiquitous molecular hydrogen, and reacts quickly to form H_3^+ : $\text{H}_2^+ + \text{H}_2 \rightarrow \text{H}_3^+ + \text{H}$. The H_3^+ ion is relatively abundant because it does not react with H_2 . The ion can react with other primary neutral atoms and is the precursor for much of the gas-phase chemistry that occurs in dense clouds. For example, oxygen chemistry can be initiated by proton donation to oxygen atoms from H_3^+ , followed by H-abstraction reactions:



The sequence is terminated here by dissociative recombination:



While there is no definite solution if deuterated cation of HCO is produced by reactions on the grain surfaces, I would like to mention that carbon chemistry in dark clouds may proceed through a similar route: $\text{C}^+ \rightarrow \text{CH}_2^+ \rightarrow \text{CH}_3^+$. The next stage of hydrogen abstraction to form CH_4^+ is endothermic and the sequence generally terminates at CH_3^+ . However, a slow radiative association of this ion with H_2 may occur: $\text{CH}_3^+ + \text{H}_2 \rightarrow \text{CH}_5^+ + h\nu$, and dissociative recombinations of these ions give CH_n , $n = 1, 2, 3$. Methane is produced by a competitive reaction with abundant CO: $\text{CH}_5^+ + \text{CO} \rightarrow \text{CH}_4 + \text{HCO}^+$. The CO molecule is formed itself by a wide variety of reactions including processes such as:



More detailed discussion on the chemical reactions important for formation of HDO and DCO^+ is given in the 3 papers included as appendices.

3.5. Star formation

Star formation occurs in the densest regions of the interstellar medium. Both giant molecular clouds and dark clouds contain smaller and denser regions, the dense cores, whose collapse leads ultimately to the formation of a single star or a group of stars. While general picture is understood, many details of this process are still unknown.

The formation of stars is initiated by a gravitational collapse in the densest parts of molecular clouds, where gravity overcomes the magnetic, turbulent, and thermal pressure of the interstellar medium. The collapse occurs when the minimum mass for which gravity dominates over other forces is reached (Jeans 1928). In the simplest case gravity has to overcome the gas pressure, which results in a Jeans mass (depending on the gas temperature T_{gas} and density ρ):

$$M_{Jeans} \simeq 1.1 M_{\odot} \left(\frac{T_{gas}}{10K} \right)^{3/2} \left(\frac{\rho}{10^{-19} \text{gcm}^{-3}} \right)^{-1/2} \quad (14)$$

Neglecting other forms of forces, once the Jeans mass is reached in an optically thin gas capable of radiating compressional heat, the gas collapses on a free-fall timescale (Shu et al. 1987):

$$t_{ff} \simeq 2.1 \times 10^5 \text{year} \left(\frac{\rho}{10^{-19} \text{gcm}^{-3}} \right)^{-1/2} \quad (15)$$

The gas collapses until the densest parts become optically thick. As a result of the conservation of angular momentum, centrifugal forces increase during the collapse, which results in flattened structures. Material flows onto a central, quasi-hydrostatic core, until the hydrogen burning starts. In this phase, the core contracts on the Kelvin-Helmholtz timescale (t_{KH}) that is dependent on the mass, radius, and luminosity of the protostellar object (M_{\star} , R_{\star} , and L_{\star} respectively):

$$t_{KH} \sim \frac{GM_{\star}^2}{R_{\star}L_{\star}} \quad (16)$$

The timescale for the accretion phase (t_{acc}) is approximately the mass of the protostar (M_{\star}) divided by the accretion rate of matter onto the protostar \dot{M} , with a typical value

of $\dot{M} \sim 10^{-5} M_{\odot} \text{yr}^{-1}$ (Palla & Stahler 1993). For low-mass stars the accretion phase ($t_{\text{acc}} \sim 1.5 \cdot 10^5$ years) ends by the time the star enters the hydrogen burning phase. In such case $t_{\text{acc}} < t_{KH} \sim 3 \cdot 10^6$ years for $2 M_{\odot}$ star. For high-mass stars, of about $30 M_{\odot}$ star these two timescales are: $t_{\text{acc}} \sim 1.2 \cdot 10^7$ and $t_{KH} \sim 10^3$ years (Palla & Stahler 1993). This means that accretion continues for high-mass protostellar objects even after the hydrogen burning starts.

Low mass stars

A young stellar object (YSO) is typically defined as any star in the earliest stage of development. The broad YSO class objects are then divided into two sub-classes: protostars and pre-main sequence stars. Protostars are heavily embedded in dust and gas. Pre-main sequence (PMS) stars are defined to be low mass stars in the post-protostellar phase of evolution. These stars have yet to enter the hydrogen-burning phase of their life and are still surrounded by remnant accretion disks called "protoplanetary" disks. The star formation process has been divided into several phases through the study of Spectral Energy Distribution (SED) (Lada & Wilking 1984, Adams et al. 1987). As a protostar evolves toward the Zero Age Main Sequence (ZAMS), the system geometry (and thus the SED) will evolve as well. Therefore, the stage of evolution of a protostar is often classified according to both the general shape and the features of the SED. Protostellar SEDs are divided into four classes, from Class 0 to Class III. The distinction between these different classes was initially defined by the slope of the SED (named the "spectral index") at infrared wavelengths, α :

$$\alpha = \frac{d \log(\lambda S_{\lambda})}{d \log(\lambda)} \quad (17)$$

where S_{λ} is the flux density measured at particular wavelength λ .

A graphical overview of the four stages of protostellar evolution are shown in Figure 5. Class 0 objects are extremely faint in the optical and near-IR and have a significant sub-millimetre luminosity. Class I sources ($\alpha > 0$) typically have SEDs which rise in the far- and mid-infrared, while Class II sources ($-2 < \alpha < 0$) have flat or falling SEDs in the mid-infrared. Class III sources ($\alpha < -2$) have weak or no emission lines and negligible excesses. However, this quantitative distinction is not always clear and is not an effective way to unambiguously distinguish between the different object classes.

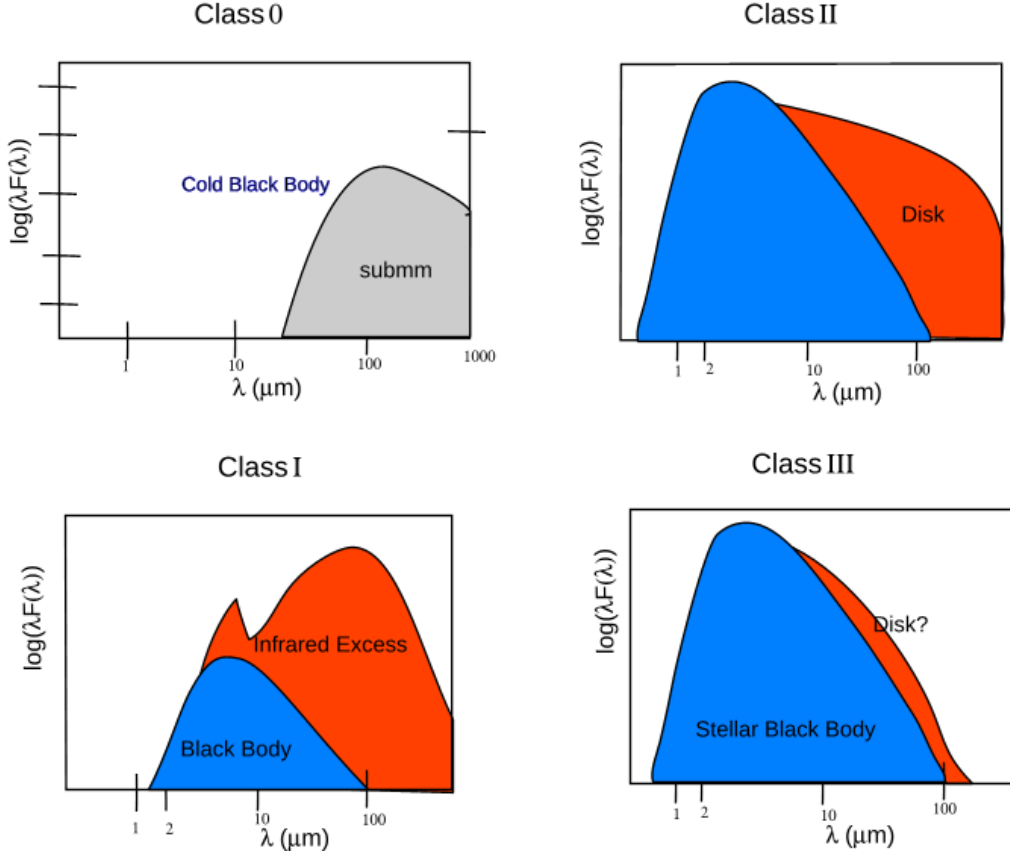


Figure 5. Spectral energy distribution (SED) at each stage of evolution. The different colours highlight the different components: the cold envelope is the grey (Class 0), the warm disk/envelope emission is orange, and star is blue.

The formation process of low-mass stars is quite well characterised observationally and theoretically (e.g. McKee & Ostriker 2007). Once the gravitational collapse of prestellar core is onset, a central protostar forms at the centre of the envelope, following a cold (10 - 30 K) black body emission in the sub-millimetre and millimetre domains. At this stage, most of the mass is still located in the envelope (Fig. 6b). Some Class 0 protostars are also identified by a bipolar outflow triggered by the interaction of collimated jet and winds coming from the protostar with surrounding envelope. The Class 0 phase last typically $\sim 10^4 - 10^5$ yr (André et al. 2000, Maury et al. 2011). The earliest phases of low-mass star formation (i.e. pre-stellar core and Class 0 protostars) are crucial to be studied because they are holding the key to the final mass of the star (André et al. 2000).

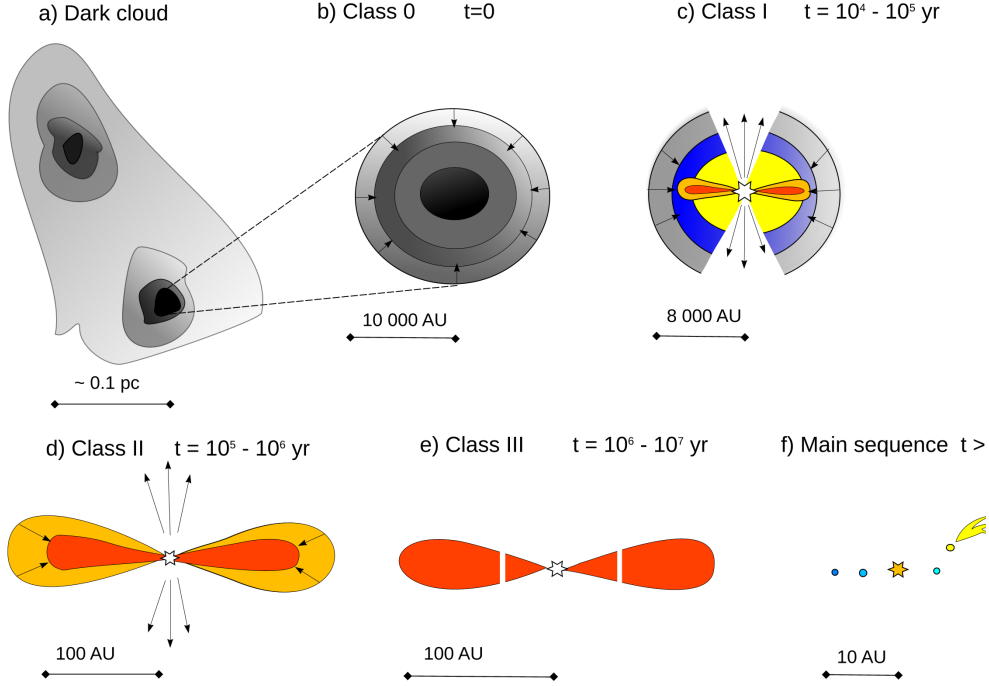


Figure 6. Evolutionary stages of low-mass star formation.

The newborn protostar gradually heats its surrounding, affecting its physical and chemical structure. The Class I phase refers to protostar that show an evolved accretion. Most of the spherical envelope has either been accreted by the protostar or is forming a protoplanetary disk. Bipolar outflows are still observed. The SED is shifted to the mid- and far-infrared domains, indicating warmer regions. The SED includes black-body emission from the protostar and IR excess coming from the disk. The Class I phase last typically $\sim 10^5 - 10^6$ yr (Fig. 6c).

During the Class II phase star shows no (or almost no) spherical envelope and an evolved circumstellar disk. The SED is a result of a black body emission from the star, starting from the visible and an IR excess coming from the circumstellar disk. The Class II phase last $\sim 10^6 - 10^7$ yr (Fig. 6d). In Class III phase, the gas is dissipated from the disk and the dust is likely in form of larger grains than in ISM (Fig. 6e).

Massive stars

Studying the formation of massive stars is not easy and their early lives are not fully understood. Though hard to miss once fully grown, massive stars spend their infancy hidden deep within thick cocoons of gas and dust, making difficult for us to observe them directly (McKee & Tan 2002). They also grow up fast, so spotting them whilst they are still being formed has proven to be very tricky. Through decades of study we have learned much about the process of massive stars formations, but the picture is still incomplete.

Based on the observations, four evolutionary stages of massive-star forming regions are distinguished, which are schematically shown in Figure 7. Massive star formation starts in High-Mass Starless Cores (HMSCs) within dense molecular clouds where the density reaches a local maximum ($> 10^6 \text{ cm}^{-3}$), and the temperature a local minimum ($< 20 \text{ K}$). Their typical masses are $100 - 1000 M_{\odot}$, and sizes: $0.25 - 0.5 \text{ pc}$ (Phase I; Fig. 7a). The mean densities of these clumps are about 10^5 cm^{-3} and the derived average temperatures are around 15 K . Millimetre and sub-millimetre molecular studies reveal that some condensations within Infrared Dark Clouds have parameters suggesting that IRDCs have the potential of harbouring the earliest stages of massive stars formation (Evans 2002, Beuther & Shepherd 2005).

In the second phase, so-called high-mass protostellar objects (HMPOs) form, hosting an actively accreting protostar(s) with mass $> 8 M_{\odot}$, which already shows an internal emission source(s) at mid-infrared wavelengths (Phase II, Fig. 7b). The central temperature rises and the temperature profile starts to deviate from the isothermal case. The physically homogeneous HMPO phase is being followed by the much warmer hot molecular core phase (HMC) (Phase III; Fig. 7c). The hot molecular cores have sizes in the order of $0.1 - 0.01 \text{ pc}$, density about $10^7 \text{ cm}^{-3} - 10^8 \text{ cm}^{-3}$ and temperatures that reach values: $100 - 300 \text{ K}$. This phase is distinguished from the earlier HMPO phase from a chemical point of view. In the HMC stage the central source(s) heats the surrounding environment, evaporating molecular-rich ices and giving rise to molecular complexity in the gas. Finally, the UV-radiation from the embedded protostar(s) ionises the surrounding gas and a hypercompact, unresolved, most likely thick HII (HCHII) region is formed (Phase IV; Fig. 7d). The HCHII region may still be partially quenched by infalling gas which can hinder the

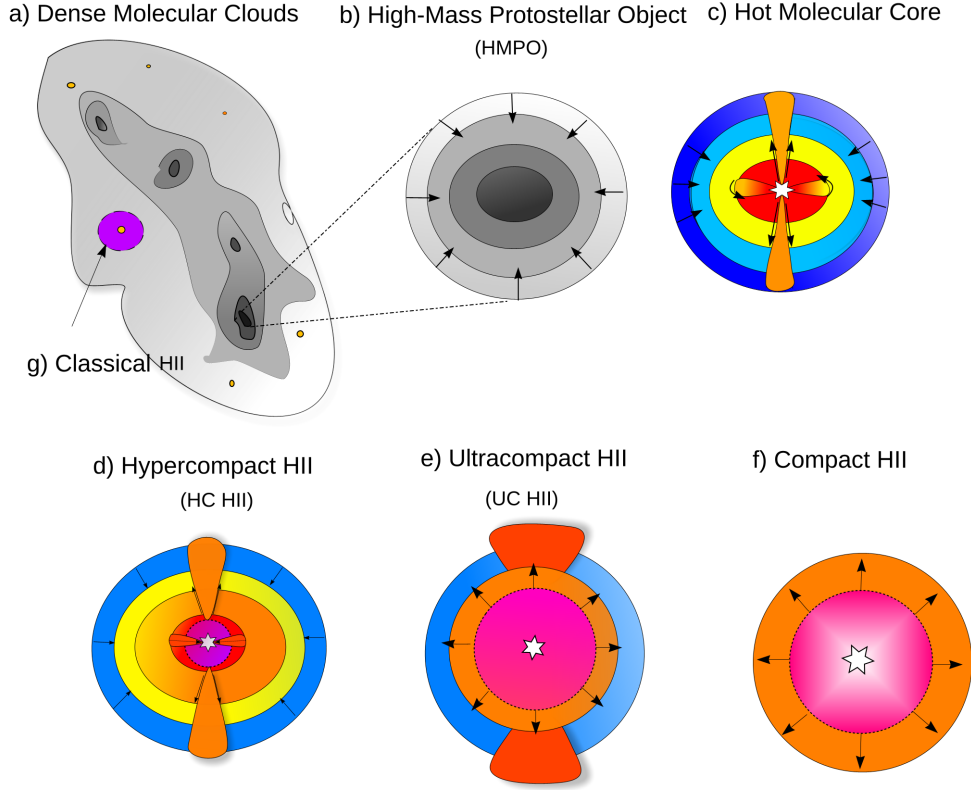


Figure 7. Observational classification of massive star-forming cores.

expansion of the hyper-compact HII region (Walmsley 1995, Keto 2003). Eventually, the HCHII region begins to expand forming well-studied ultracompact HII region (UCHII, Fig. 7e) and later a more evolved HII region (Fig. 7f). The difference between the HCHII regions and the UCHII regions is their size, typical from 0.01 pc to 0.1 pc (Keto 2007). Physically the ultracompact HII regions have probably stopped accretion at this point, but this class is not entirely homogeneous either an accretion may still continue in some UCHII regions (Kurtz et al. 1994, Gerner et al. 2014).

Because the evolution in high-mass star formation takes place on rather short timescales and in clustered environments, the transitions from one into next stage are smooth and not always clearly distinct.

Bipolar outflows from young stars

Young stars are associated with prominent outflows of molecular gas (Frank et al. 2014). The ejection of gas via these outflows is believed to remove angular momentum from protostellar system, thus permitting young stars to grow by accretion of material from the protostellar disk. The underlying mechanism for outflow ejection is not yet understood, but believed to be closely linked to protostar disk (Cabrit et al. 1990). Assorted scenarios have been proposed to explain protostellar outflows, and the main difference between these models is the region where acceleration of material takes place: *i*) close to the protostar itself e.g. X-wind or stellar wind; *ii*) in a larger region throughout the protostar disk e.g. disk wind; *iii*) or at the interface between them. Theoretically, X-winds naturally produce fast, well collimated outflows (Shu et al. 1994), stellar winds are effective at spinning down the central protostar (Bouvier et al. 2014), while slow outflows and wide opening angles are more easily explained by disk wind models (Pudritz et al. 2007).

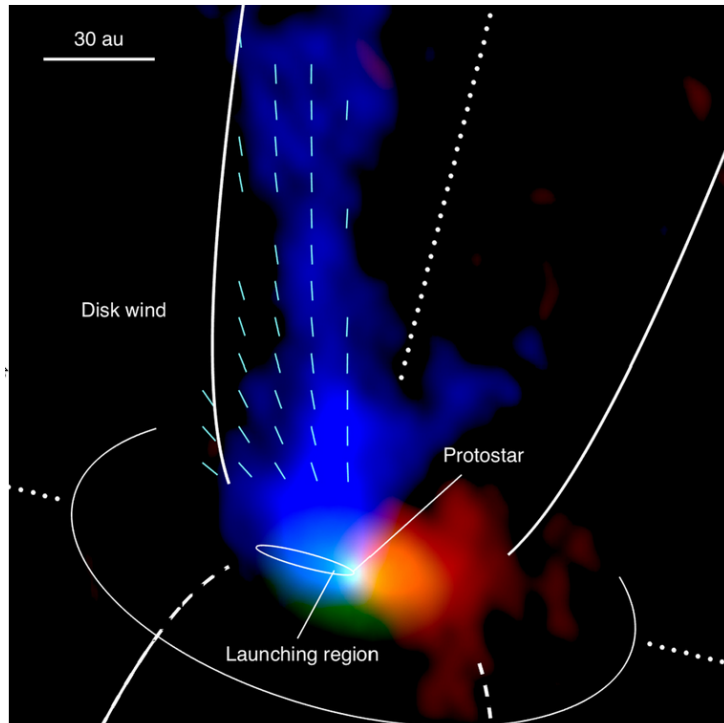


Figure 8. Resolved image of a protostellar outflow in TCM1A launched by an extended disk wind (*credit: Nature*)

Recently Bjerkeli et al. (2016) obtained high-resolution millimetre-wave observations of the region surrounding the protostar TCM1A which is located in Taurus Molecular Cloud, using the Atacama Large Millimetre Array. They observed the $J = 2-1$ rotational transition of the carbon monoxide isotopologues ^{12}CO , ^{13}CO , and C^{18}O . The observations suggest that CO outflow is launched from a region extending up to a radial distance of 25 astronomical units from the central protostar, and the wind, like a tornado, lifts material and gas up from the rotary disc (Fig. 8). In order to slow down the rotation, the energy must be carried away. This happens when the new star emits wind. The wind is formed in the disc around the protostar and thus rotates together with it. When this rotating wind moves away from the protostar, it thus takes part of the rotational energy with it and the dust and gas close to the star can continue to contract.

It has been suggested that a combination of different mechanism is needed to explain all of the observations, where the disk wind might be important for driving a wide-angle outflow capable of removing a large portion of the infalling envelope (Arce et al. 2006).

3.6. Preface to the included publications

Water is one of the most important molecules in the interstellar medium. It plays a dominant role in gas cooling processes, it is a substrate for many chemical reactions, but above all it is the basis of life. Unfortunately, strong absorption in the Earth's atmosphere makes it impossible to observe the majority of its rotational transitions. An alternative solution for terrestrial observatories is the observation of its isotopologue: HDO molecule. It arises at the early stages of star birth, when low temperatures and high densities favour the processes of deuteration and the formation of icy mantles around dust grains. When the radiation of the young star leads to the evaporation of ice coatings it becomes possible to observe the HDO rotational transitions. The semiheavy water molecule is of great diagnostic importance.

Previous research and observations about HDO have been carried out almost 20 years ago, when millimetre observation technology was just beginning to develop. Observations of authors such as Jacq et al (1990) or Gensheimer et al. (1996) led to determining the frac-

tional abundance of HDO, $X(\text{HDO})^4$, but only in the inner regions of massive protostars, e.g. G34.26, W51 or DR21(OH). In recent years abundance of HDO was determined both in hot molecular cores ($T > 100$ K) and in cold protostellar envelopes ($T < 100$ K): Sgr B2 (M) (Comito et al 2010), G34.26+0.15 (Liu et al. 2013, Coutens et al. 2014), AFGL 2591 (van der Tak et al. 2006) and in intermediate mass protostar NGC 7129 FIRS2 (Fuente et al., 2012).

In search of an answer to the question what processes led to the formation of water in the interstellar medium, the deuterium fractionation $[\text{HDO}]/[\text{H}_2\text{O}]^5$ is used as a diagnostic tool. Flagey et al. (2013) has observed H_2^{18}O as part of the *Herschel* / PRISMAS program. Thanks to the courtesy of the authors, already reduced observations of two low-energy water transitions were obtained. During the first series of observations, rotational transitions of HDO ($1_{0,1}-0_{0,0}$) at 464.925 GHz were obtained for the sources: Sgr B2(N), Sgr B2(M), W31C, DR21(OH), and W33A with a 10 m telescope CSO in 2007 on Mauna Kea (Hawaii, USA). During the second series of observations, made in 2011, in addition to the 464.925 GHz line, a rotational transition ($1_{1,0}-1_{0,1}$) was observed at 509.292 GHz of the following sources: G34.26+0.15, W49N and W51 e1/e2. Rotational HDO transitions which were observed by Jacq et al (1990) at other frequencies were also used in the presented work. Using our data, an abundance of $X_{out}(\text{HDO})$ has been determined in the cool envelopes of these sources. Based on to the reduced observations of the two low energy transitions of H_2^{18}O , obtained from N.Flagey, I determined an abundance of $X(\text{H}_2\text{O})$ and the ratio $[\text{HDO}]/[\text{H}_2\text{O}]$ in the outer, cold shells of the sources studied.

The numerical code of Zmuidzinas (Zmuidzinas et al., 1995) was used in my work. In the model calculations, which are matched to the observed spectra, the ALI method (Accelerated Lamda-Iteration method - Rybicki and Hammer 1991) was used. Despite the use of a very simple model, the obtained values of HDO abundance in the outer shell are comparable to those obtained by other authors. The lowest HDO rotational transition $1_{0,1}-0_{0,0}$ at 464.925 GHz is a very good "tester" of conditions prevailing in the

⁴ Fractional abundance (X) is understood as the ratio of the column density of a given molecule to the column density of molecular hydrogen, ie: $X(\text{HDO}) = N(\text{HDO})/N(\text{H}_2)$

⁵ Deuterium fractionation or fractionation abundance ratio is defined as: $[\text{XD}]/[\text{XH}] = N(\text{XD})/N(\text{XH}) = X(\text{XD})/X(\text{XH})$

cool ($T < 100$ K) outer shell. The situation looks different with the modeling of the 509 GHz line. This line is formed in a complex region, and the Zmuidzinias' model does not take into account either the velocity field nor the presence of any accretion disk. Note that the rotational transition at 509 GHz along with the 465 GHz line would enable, after refining the source code, modeling the physical conditions and dynamics of the processes taking place in the outer layers of the protostar.

The obtained results confirm that HDO's abundance is higher in central regions ($T > 100$ K). This is consistent with other observations of regions where low mass and massive stars are formed (e.g., NGC 1333 IRAS2A, IRAS 16293-2422, AFGL 2591, G34.26). In the case of high-mass protostars, the abundance of HDO are lower than in low-mass sources. This is most likely due to the fact that the period when the temperature is below the CO sublimation temperature is shorter in massive protostars than in the low mass ones. From a chemical point of view, this results in a shortening of time when deuteration reactions are effective (Caselli et al 2008). The $[\text{HDO}]/[\text{H}_2\text{O}]$ ratios were found to be higher in the cold outer envelopes than in the hot cores, as already determined for two high-mass sources.

Young stellar objects, deeply immersed in molecular clouds, are the source of bipolar molecular outflows. The impact of the ejected material on the surrounding clouds causes shock fronts which play a crucial role in the chemical evolution of star-forming regions because they induce large variations of temperature and density in the surrounding medium (Arce et al. 2007). The shock velocity, derived from high-J CO data, is only 8 - 10 km/s, insufficient to destroy dust grains, but sufficient to evaporate grain mantles (Lis et al. 2012, 2016). The shock-compressed, dense gas cools efficiently and the increase in density and low temperature shortens the depletion time-scale and produces conditions which favour the deuteration process. The slow C-type shocks may release deuterated material present in the grain mantles to the gas-phase. In this case, CO would also be released into the gas-phase, resulting in a quick destruction of at least deuterated ions. DCO^+ is an example of a molecule that is formed in the gas-phase deuteration process associated with shocks. The increased emission of DCO^+ is observed in regions with temperatures of 20 - 30 K. The formation of this molecule requires the presence of the H_2D^+ ion and carbon monoxide, which under these conditions is frozen on dust grains. The availability

of CO is possible due to the shock front which eject CO from the icy surface of grains. In such cases the emission of DCO^+ is observed in the border region between the shock and the matter of the cloud. It is rather a short phase in the course of the evolution of the dense core because already at temperatures 30 - 80 K the ions CH_2D^+ and C_2D^+ take the dominant role in the deuteration processes (Roberts & Millar 2000). At a temperature of 50 K the contribution of the H_2D^+ ion to deuteration is practically inhibited.

The analysed observations were carried out in the years 2002 - 2007 with a 10-meter CSO telescope on Mauna Kea. In the presented dissertation, emission maps of DCO^+ have been presented together with CO(2–1) emission contours and dust emission on frequency $350\ \mu\text{m}$ in the regions of low-mass star formation: B1, NGC 1333, LDN 1251, LDN 1630, LDN 1641 and S 68. It can be concluded from the observations that DCO^+ is a marker of cool, dense gas and deuteration processes. However, in many situations it is difficult to determine whether the maximum of emission is associated with a protostar hidden inside or with the condensation of matter in the molecular cloud. There is a need for observations with a higher spatial resolution, which would allow to prove whether the separation of the maxima of emissions is real, caused by the propagating shock front or apparent, and in fact related to the emerging star.

References

- Adams, W. S. 1939, *ApJ*, 93, 11
- André, R. I., Ward-Thompson, D. & Barsony, M. 2000, *Protostars and Planets IV*, Tucson: AZ: Univ. Arizona Press, ed. Mannings, V., Boss, A. P., Rusell, S.S., p.59
- Arce, H. G., Shepherd, D., Gueth, F., et al. 2007, *Protostars and Planets V*, Tucson, AZ: Univ. Arizona Press, ed. Reiputh, V. B., Jewiit, D., Keil, K., p.245
- Arce, H. G., Sargent, A. I. 2006, *ApJ*, 646, 1070
- Bergin, E., & Tafalla, M. 2007, *ARAA*, 45, 339
- Beuther, H., & Sheperd, D. 2005, *A&SSL*, 324, 105
- Bjerkeli, P., van der Wiel, M. H.D., Harsono, D., et al. 2016, *Nature*, 540, 406
- Bok, B. J. & Reilly, E. F. 1947, *ApJ*, 105, 255
- Bonnell, I. A., Bate, M. R., Clarke, C. J. 2001, *MNRAS*, 323, 785
- Bouvier, J., Matt, S. P., Mohanty, S., et al. 2014, *Protostars and Planets VI*, Tucson, AZ: Univ. Arizona Press, ed. Beuther, H. Klessen, R. S., Dullemond, C. P. & Henning, T., p.433
- Cabrit, S., Edwards, S., Strom, S. E., et al, 1990, *ApJ*, 354, 687
- Cambrésy, L. 1999, *A&A*, 345, 965
- Casali, M. M.; Eiroa, C.; Duncan, W. D.1993, *A&A*, 275, 195
- Caselli, P. Walmsley, C. M. Zucconi, A. et al. 2002, *ApJ*, 565, 344
- Cheung, A. C., Rank, D. M., Townes, C. H., et al. 1968, *Phys. Rev. Letters*, 21, 1701
- Comito, C., Schilke, P., Rolffs, R., et al. 2010 *A&A*, 521, L38
- Coutens, A., Vastel, C., Hincelin, U., et al. 2014, *MNRAS*, 445, 1299
- Cuppen, H. M. & Herbst, E. 2007, *ApJ*, 668, 294

- Dunham, T. Jr. 1937, PASP, 49, 26
- Ewen, H. I., Purcell, E. M. 1951, Nature, 168, 356
- Evans, N.J., et al. 2003, PASP, 115, 965
- Frank, A., Ray, T. P., Cabrit, S., et al. 2014, Protostars and Planets VI, p.451
- Fuente, A., Caselli, P., Coey, C. M. 2012, A&A, 540, 75
- Gensheimer, P. D., Mauersberger R., Wilson, T. L. 1996, A&A, 314, 281
- Gerner, T., Beuther, H., Semenov, D., et al. 2014, A&, 563, 97
- Ioppolo, S., van Boheemen, Y., Cuppen, H. M., et al. 2008, ApJ, 686, 1474
- Jacq, T., Walmsley, C. M., Henkel, C., et al. 1990, A&A, 228, 447
- Keto, E. 2003, ApJ, 599, 1196
- Kurtz, S., Churchwell, E., Wood, D. O. S., Myers, P. 1994, AAS, 184, 3013
- Lis, D.C., Gerin, M., Phillips, T.G., & Motte, F. 2002, ApJ, 569, 322
- Lis, D.C., Wootten, H.A, Gerin, M., et al. 2016, ApJ, 827, 133
- Liu, F. C., Parise, B., Wyrowski, F., Zhang, Q., Gusten, R. 2013, A&A, 550, A37
- Mathis, J. S. 1996, ApJ, 472, 643
- Maury, A. J., André, P., Menshchikov, A. et al. 2011, A&, 535, 77
- Merrill, P. W. 1934, PASP, 46, 206
- McKellar, A. 1940, PASP, 52, 187
- Oba, Y., Watanabe, N., Hama T., et al. 2012, ApJ, 749, 67
- Ormel, C. W., Paszun, D., Dominik, C. et al. 2009, A&A, 502, 845
- Ossenkopf, V. 1993, A&A, 280, 617
- Palla, F. & Stahler, S. W. 1993, ApJ, 418, 414

- Pierre, L., Guignes, H. & Lhuillier, C. 1985, JCP, 82, 496
- Pudritz, R. E., Ouyed, R., Fendt, C., et al. 2007, *Protostars and Planets V*, p.277
- Roberts, H., Millar, T. J. 2000, A&A, 361, 780
- Rybicki, G. B. & Hummer, D. G. 1991 A&A, 245, 171
- Shu, F. H., Najita, J., Ostriker, E. et al, 1994, ApJ, 429, 781
- Shu, F. H., Adams, F. C., Lizano, S. 1987, ARA&A, 25, 23
- Snow, T. P., McCall, B. J. 2006, ARA&, 44, 367
- Snyder, L. E., Zuckerman, B., Buhl, D., Palmer, P. 1969, BAAS, 1, 363
- Solomon, P. M., Sanders, D. B., Scoville, N. Z. 1977, BAAS, 9, 554
- Tielens, A. G. G. M. 2005, *The Physics Chemistry of the ISM* (Cambridge Univ. Press)
- Tielens, A. G. G. M. & Allamandola, L. J. 1987, in *Interstellar Processes*, ed. D.J. Hollenbach & H. A. Thronson, p.397
- Tielens, A. G. G. M. & Hagen, W. 1982, A&A, 114, 245
- van der Tak, F. F. S., Walmsley, C. M., Herpin, F., et al. 2006, A&A, 447, 1011
- Walmsley, C. M., Cesaroni, R., Olmi, L., et al. 1995, Ap&SS, 224, 173
- Weinreb, S. Barrett, A. H., Meeks, M. L. et al. 1963, Nature, 200, 829
- Whittet, D. C. B., Bode, M. F., Longmore, A. J., et al. 1988, MNRAS, 233, 321
- Whittet, D. C. B., Shenoy, S. S., Bergin, E., et al. 2007, ApJ, 655, 332
- Whittet, D. C. B., Cook, A. M., Herbst, E. 2011, ApJ, 742, 22
- Williams, J. P., de Geus, E. J., Blitz, L. 1994, ApJ, 428, 693
- Wilson, R. W., Jefferts, K. B. & Penzias, A. A. 1970, ApJ, 161, L43
- Yun, J. L. & Clemens, D. P. 1990, ApJ, 365, 73

Zmuidzinas, J., Blake, A., Carlstrom, J. 1995, ApJ, 447, L125

Appendices:

Appendix A

Observations of HDO in the High-Mass Star Forming Regions

Observations of HDO in the High-Mass Star Forming Regions

M. Kulczak-Jastrzębska

Astronomical Observatory of the Jagiellonian University, Orla 171, 30-244 Kraków,
Poland
e-mail: kulczak@oa.uj.edu.pl

Received November 8, 2014

ABSTRACT

I present observations of the ground state ($1_{0,1}-0_{0,0}$) rotational transition of HDO at 464.925 GHz toward several high-mass star forming regions carried out with the Caltech Submillimeter Observatory. The spectra are modeled together with observations of higher-energy HDO transitions and submillimeter dust continuum fluxes present in the literature. Spherically symmetric radiative transfer model was used to derive the radial distribution of the HDO abundance in the target sources. The abundance profile is divided into an inner hot core region, with kinetic temperatures higher than 100 K, and a cold outer envelope. The derived HDO abundances relative to H_2 are: $(0.6-3.5) \times 10^{-8}$ and $(0.1-25) \times 10^{-11}$ in the hot inner region and the cold outer envelope, respectively.

Key words: *Stars: pre-main sequence – ISM: molecules – ISM: lines and bands*

1. Introduction

Massive stars have a profound effect on the Galactic environment and are responsible for recycling and enriching interstellar matter. Contrary to solar-type stars, massive stars arrive on the main sequence while they are still accreting matter from their protostellar surroundings (Iben 1965). In the embedded stage of high-mass star formation, the central source is surrounded by a collapsing envelope that spans a wide range in densities and temperatures (André *et al.* 2000). The intense ultraviolet radiation emitted at that moment by the central object first heats then ionizes its parental molecular clouds leading to formation and development of a hot core ($T > 100$ K, Walmsley and Schilke 1992) and an ultra-compact HII region. Massive stars evolve more rapidly and are more rare compared to low-mass stars. These makes studying them challenging. Hot cores are the best laboratories for interstellar chemistry, their high column densities allow the detection of the less abundant species. Water is one of the most important molecule in the interstellar

space. Water plays essential role in the cooling of warm gas, in the oxygen chemistry and in the chemistry of the atmospheres of exoplanets. Unfortunately, the H_2O low-energy lines are almost invisible from the ground due to a very strong absorption. Given the difficulty of detecting water, several alternatives have been pursued. The most natural is to observe rare isotopologues like HDO (deuterium hydrogen monoxide, so called semiheavy water). This molecule suffers much less telluric absorption and has some lines at sub-mm and mm-frequencies. Furthermore if HDO is formed on the surfaces of grains before the heating due to radiation from an accreting protostar (*e.g.*, Parise *et al.* 2005, and reference therein) then its emission can also be used to trace the past history of water formation. Although the process leading to the water deuteration are not fully understood, it is clearly related to grain surface chemistry and reveals the chemical and physical history of protostars (Cazaux *et al.* 2011, Taquet *et al.* 2013)

Previous studies of the water fractionation in the high-mass hot cores were performed almost twenty years ago, when the submillimeter spectrum was difficult to observe (Jacq *et al.* 1990, Gensheimer *et al.* 1996, Helmich *et al.* 1996). HDO abundance has been recently determined toward high-mass hot cores (Coutens *et al.* 2012, Liu *et al.* 2013). We present observations of the ground state rotational transition of HDO at 464.925 GHz toward five high-mass star forming regions: SgrB2(N), SgrB2(M), W33A, W31C, and DR21(OH). This is the first time when $1_{0,1} - 0_{0,0}$ rotational transition of HDO is used to probe the outer envelope in this sources. We aim here to determine the HDO fractional abundances relative to H_2 in the inner and outer region of the core in our target sources using the static radiative transfer code of Zmuidzinas *et al.* (1995).

2. HDO Chemistry

The chemical fractionation process arises from differences in the molecular binding energies caused by the different zero-point vibration energy. In the molecular clouds, hydrogen and deuterium are predominantly in the form of H_2 and HD

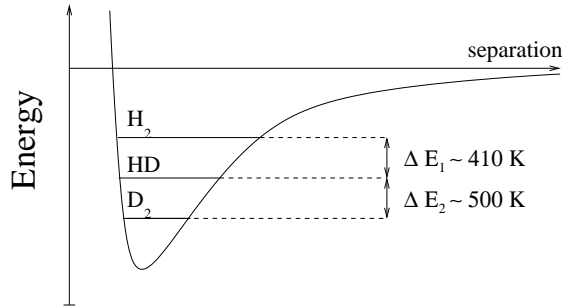


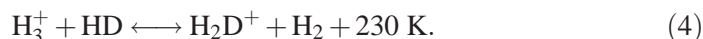
Fig. 1. H_2 , HD and D_2 potential energy diagram. E_i is the difference between the zero point energies relative to the minimum of the molecular potential curve (reproduced with permission of Phillips and Vastel 2003).

respectively. Since zero-point energies of HD and H₂ differ greatly (Fig. 1), the chemical fractionation will favor production of HD compared to H₂ (Solomon and Woolf 1973).

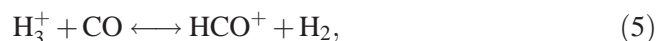
Deuterium is initially removed from the atomic phase through charge exchange with H⁺, followed by reaction with abundant H₂ (Solomon and Woolf 1973). HD can further interact with D⁺ again to give D₂:



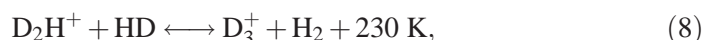
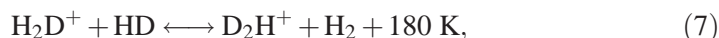
H₂ molecule is very light and vibrates rapidly. The ground state is considerably higher in energy than it is observed in the HD molecule (Fig. 1), so the second reaction above will proceed to the right. Thus, initially in cold regions most of D will be in the form of HD. During collapse, in the early protostellar stages, the temperature stays low at $\approx 10 \text{ K}$ while the density increases to $n(\text{H}_2) \geq 10^8 \text{ cm}^{-3}$. Under these conditions the line emission of many molecules is dominated by a warmer outer envelope around the pre-stellar core. As the density increases gaseous molecules start to freeze out onto the cold dust grain forming water dominated ice mantles dirtied with several other molecules. In the innermost and densest regions of the condensation, heavy elements bearing molecules are thought to be virtually all frozen out. Eventually, only H₂, H₃⁺, and their isotopomers HD and H₂D⁺ will remain in the gas phase (Bergin and Tafalla 2007). This leads to a significant enhancement of H₂D⁺ to the deuterium exchange reaction:



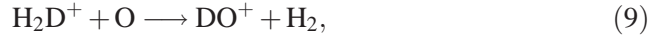
However, the H₃⁺ abundance is limited by reaction with other molecules, such as CO, which are abundant, *e.g.*, :



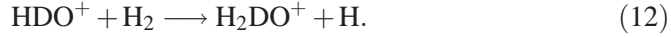
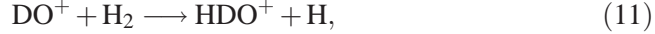
Thus, the deuteration moves into heavy molecules and the H₂D⁺ abundance is limited. The role of dust grain must be considered since it is known that many molecules will condense out on the grains and will be depleted in the cold dense regions. The deuteration reactions do not stop with H₂D⁺, rather they continue toward the formation of both D₂H⁺ and D₃⁺ via the similar reactions sequence (Vastel *et al.* 2003):



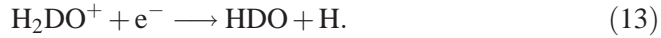
The freeze-out of CO which is primary destroyer of both H_3^+ and H_2D^+ increases the rate of gas phase fractionation reactions. This inference is strongly supported by the detection of H_2D^+ and D_2H^+ in starless cores (Vastel *et al.* 2004). A study of gas phase of hot cores provides an insight into both the gas phase and the surface chemistry of cold, dense clouds. It is believed that the gas phase abundances in hot cores reflect, to a large degree, the grain mantle composition in a cold dense cloud. The mantles evaporate as the region's temperature increases. At the temperatures deduced for hot cores regions (100 K–300 K) very little fractionation is expected to occur because the energy barriers inhibiting the reverse route of reactions may be overcome by the elevated temperature (Millar *et al.* 1989). The major pathway for forming HDO is also initiated by H_2D^+ (the heart of the fractionation of deuterated molecules). There are two possible channels:



The next two stages:



Finally dissociative recombination of H_2DO^+ yields several possible channels, but HDO is thought to be formed through this one:



3. HDO Observations

3.1. Sources Characteristics

The $1_{0,1} - 0_{0,0}$ ground state rotational transitions of HDO at 464.925 GHz were observed in the five high-mass star forming regions listed in Table 1. All the sources are characterized by strong millimeter continuum and mid-infrared emission characteristic of the early stage of high-mass stars formation.

Sgr B2(N) and Sgr B2(M): The Sgr B2 complex represents a burst of high-mass star formation in the central region of our Galaxy. The main signposts of star formation activity are located within three dust condensations labeled as Sgr B2(N), (M), and (S). They contain all the tracers of ongoing star formation: UCHII, hot cores embedding protostars, molecular masers and far-IR continuum intensity (Scoville *et al.* 1975, Goldsmith *et al.* 1987 and references therein).

W31C (G10.62–0.38) is a well studied region of massive stars formation. The bright continuum emission seen in the new high angular resolution observations of G10.62–0.38 (Sollis 2005) is identified as a dense accretion disk or torus rather than a classical ionization bounded HII region.

Table 1

Coordinates and kinematic distances of the target sources

Source name	α (J2000)	δ (J2000)	D [kpc]
Sgr B2(N)	17 ^h 47 ^m 20 ^s .2	−28°22′21″	8.5 ^a
Sgr B2(M)	17 ^h 47 ^m 20 ^s .13	−28°23′06″.1	8.5 ^a
W31C	18 ^h 10 ^m 28 ^s .7	−19°55′51″.5	4.9 ^b
DR21(OH)	20 ^h 39 ^m 00 ^s .8	+42°22′48″	2.0 ^c
W33A	18 ^h 14 ^m 37 ^s .3	−17°52′02″.5	4.0 ^d

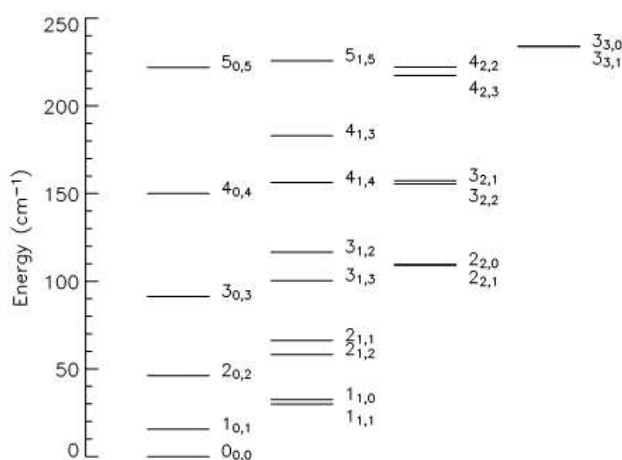
^aReid *et al.* (2009), ^bSanna *et al.* (2014),^cRygl *et al.* (2012), ^dFaundez *et al.* (2004)

Fig. 2. The HDO energy levels diagram.

DR21(OH) region is a condensation of dense molecular gas within the Cygnus-X complex. Numerous observations of *DR21(OH)* identify it as a very young massive star formation region with multiple OB star clusters forming. Both star-forming cores MM1 and MM2 in *DR21(OH)* are young, with no visible HII region and only very weak continuum emission at the centimeter wavelengths. The region is characterized as a high-mass star-forming region due to the detection of centimeter and millimeter maser emission from numerous transitions, *e.g.*, H₂O, OH and Methanol, which traces the very early stages of star formation (Araya *et al.* 2009, Mangum *et al.* 1992).

W33A (G12.90−0.25) is known as Massive Young Stellar Object (MYSO). MYSOs represent the phase in massive star's formation just before the star reaches the main sequence but while it is still accreting. De Vit *et al.* (2007) found evidence for a rotationally flattened cool envelope or torus, at a radius of 2000 a.u. from the central star. *W33A* is recognized as a region with very high far infrared luminosity, but faint radio continuum emission.

Table 2

Observed and modeled HDO rotational transitions

HDO transitions*	Freq [GHz]	E_{up} [K]	A_{ul} [s ⁻¹]	Telescope	FWHM ["]
1 _{0,1} –0 _{0,0}	464.925	22.29	1.69×10^{-4}	CSO ^a	15.7
2 _{1,1} –2 _{1,2}	241.562	95.22	1.18×10^{-5}	IRAM ^b	12.0
3 _{1,2} –2 _{2,1}	225.897	167.56	1.31×10^{-5}	IRAM ^b	13.0
4 _{2,2} –4 _{2,3}	143.727	319.17	2.80×10^{-6}	IRAM ^b	17.0

*JPL spectral line catalog (Pickett *et al.* 1998), ^athis work, ^bJacq *et al.* (1990).

3.2. Data Analysis and Processing

Observations of the 464.925 GHz HDO emission presented here were carried out in 2007, using the 10.4 m Leighton Telescope of Caltech Submillimeter Observatory (CSO) on Mauna Kea in Hawaii. We used the 460 GHz facility SIS receiver and acoustooptical spectrometers with a total bandwidths 1 GHz. The frequency scale of the spectrometer (the reference channel and the channel width) was established by injecting calibration signals from a 100 MHz frequency comb generator. Pointing of the telescope was checked by performing five-point continuum scans of planets and strong dust continuum sources. The spectra were obtained in antenna temperature units, T_A^* , and then converted to the main beam brightness temperature, T_{mb} , via the relation $T_A^* = \eta_{\text{mb}} T_{\text{mb}}$, η_{mb} – the CSO main-beam efficiency at 460 GHz determined from total-power observations of planets is ≈ 0.45 . The absolute calibration uncertainty of individual measurements is $\approx 20\%$. We also used SCUBA data at 353 GHz which provide an accurate determination of the source continuum flux.

Table 3

Line Gaussian parameters of the CSO HDO data

Source name	V_{LSR} [km/s]	ΔV [km/s]	$T_{\text{mb}}^{\text{peak}}$ [K]
Sgr B2(N)	67.89 (0.39)	11.00 (0.93)	0.97
Sgr B2(M)	63.27 (0.40)	3.70 (1.18)	0.37
W33A	38.14 (0.60)	6.40 (1.50)	0.19
W31C	−1.94 (0.86)	9.80 (2.09)	0.36
DR21(OH)	−2.50 (0.58)	2.50 (1.2)	0.15

The data processing was done using the IRAM GILDAS software package (Pety 2005). We measured the line parameters (central velocity: V_{LSR} , line emission velocity width at FWHM: ΔV , peak intensity: $T_{\text{mb}}^{\text{peak}}$) by fitting a single Gaus-

sian profile. The line parameters of the CSO observations of the HDO $1_{0,1}-0_{0,0}$ transition are shown in Table 3.

We combine the CSO 464.925 GHz data with previously published observations of higher-energy HDO transitions: $2_{1,1}-2_{1,2}$, $3_{1,2}-2_{2,1}$, $4_{2,2}-4_{2,3}$ for SgrB2(N) and $3_{1,2}-2_{2,1}$ for SgrB2(M) (Jacq *et al.* 1990, Table 2). The line parameters are shown in Table 4.

Table 4

Line Gaussian parameters of the IRAM HDO data

Source name	Freq [GHz]	V_{LSR} [km/s]	ΔV [km/s]	$T_{\text{mb}}^{\text{peak}}$ [K]
Sgr B2(N)	143	63.4 (0.7)	14 (1.6)	0.4
	225	63.9 (1.5)	14 (4.0)	1.3
	241	62.3 (1.6)	6.0 (3.1)	1.2
Sgr B2(M)	225	68.0 (7.5)	22.0 (20)	0.4

4. Determination of the HDO Abundance

4.1. HDO Line Modeling

The goal of this study is to determine the HDO fractional abundance in the high-mass star formation region studied. To reproduce the observed line intensities (listed in Table 3) the static radiative code described by Zmuidzinas *et al.* (1995) is used. The model cloud is divided into 200 radial shells and the code uses a multilevel accelerated lambda-iteration method (Rybicki *et al.* 1991) to solve for the HDO level populations and the line and continuum radiative transfer in a self-consistent fashion. This radiative transfer program takes into account the excitation of HDO molecules by collisions, line radiation, and dust continuum radiation at the HDO line frequencies. However, IR radiative pumping through HDO vibrationally excited levels and the large-scale velocity field, characteristic of infall or expansion, are not included. The HDO collisional coefficient with H_2 used in this study were recently computed by Faure *et al.* (2012) and Wiesenfeld *et al.* (2011) in the temperature range 5–300 K and for all rotational transitions with upper energies less than 444 K.

We carried out model calculations from inner core radius, r_{min} , to outer radius, r_{max} ($\frac{r_{\text{min}}}{r_{\text{max}}} \approx 100$, Hatchell and van der Tak 2003). The distance of the edge of the core from the star is set at $r_{\text{min}} \approx 2.0 \times 10^{16}$ cm or ≈ 1000 a.u., with no dust emission seen at the smaller radius. The lack of submillimeter emission in the core centers could be due to optical depth effects or a central cavity (van der Tak *et al.* 2000).

We adopted a dust-to-gas ratio of 1:100 and a power-law H_2 density distribution of the form:

$$n(r) = n_0 \left(\frac{r}{r_{\min}} \right)^{-1.5} \quad (14)$$

n_0 is the H_2 density at the reference radius ($r_{\min} = 1000$ a.u.). The power-law index was set to 1.5 according to the static infall theory in the inner part of the object (Shu 1977, Beuther *et al.* 2002, Marseille *et al.* 2010). We assumed that the gas and dust radial temperature profile follow a power law (Viti and Williams 1999):

$$T(r) = T_0 \left(\frac{r}{r_{\min}} \right)^{-0.5} \quad (15)$$

where T_0 represents the maximum temperature of dust grains. We assumed that at densities found in hot cores the gas temperature is equal to the dust temperature.

Table 5

Continuum flux densities and grain emissivity exponents

Source	F_{353}^a [Jy/beam]	F_{660}^a [Jy]	F_{250}^b [Jy]	β
SgrB2(N) ^c	1.10
SgrB2(M) ^c	1.40
W33A	2.90	53.3	1.6	1.70
W31C	27.5	1100.0	27.9	1.85
DR21(OH) ^d	1.50

^aSCUBA (Hill *et al.* 2006), the accuracy is about 6% (Thompson *et al.* 2006), ^bSIMBA (Hill *et al.* 2006),

^cLis *et al.* 1993, ^dZapata *et al.* 2011

We approximated the radial variation of the HDO fractional abundance, $X = n(\text{HDO})/n(\text{H}_2)$ as a one-step model with an enhanced abundance X_{in} in the inner region where $T \geq 100$ K, and a lower value X_{out} for the outer envelope where $T < 100$ K. Laboratory studies indicate that the evaporation temperature lies in the 90–110 K range, depending on ice composition and structure (Fraser *et al.* 2005). In this work the sublimation temperature of water, $T = 100$ K (Fraser *et al.* 2001), is applied as the jump temperature. The model uses the following free parameters: n_0 , T_0 and X_{in} (for $T \geq 100$ K) and X_{out} (for $T < 100$ K). We take $r_{\min} = 1000$ a.u. in all sources. We determine the continuum flux density per beam at 353 GHz (850 μm), from the model. A comparison of these values with SCUBA observations provides additional constraints on the physical parameters of the model (Table 5). Finally, the synthetic spectra and continuum emission are convolved to the telescope beam size for comparison with the observations. The best model of a source is a model with the lowest value of the “figure of merit”

(FOM, Jacq 1990). FOM is computed from the observed and modeled spectra according to the following formalism for the set of n spectral lines:

$$\text{FOM} = \sum_n \frac{(A_{\text{obs}} - A_{\text{mod}})^2}{(A_{\text{obs}})^2} + \frac{(F_{\text{obs}} - F_{\text{mod}})^2}{(F_{\text{obs}})^2} \quad (16)$$

where $A_i = \int T_{\text{mb}_i} dV \equiv \int T_i dV$ (i : obs, mod) – integrated line intensity (velocity integrated area). Model parameters describing the density and temperature distribution are constrained primarily by the continuum SED, while the inner and outer HDO abundances are constrained by the spectral line data.

4.2. Dust Emissivity Index β

When molecules are depleted inside pre-stellar cores, dust emission may represent the best tracer of the gas density distribution just prior to the onset of gravitational collapse. The dust continuum optical depth is described by a power-law frequency dependence, $\tau \propto \nu^\beta$, and to fit the dust continuum emission the knowledge of the grain emissivity exponent, β , is required. The dust emissivity (and hence the dust grain index β) is strongly influenced by grain size, grain shape, grain mantles, grain mixture and the dust temperature (Hildernand 1983, Goldsmith *et al.* 1997). Observationally, there have been many attempts at determining and explaining β . Typical value of β range between 1 and 2, but further support for $\beta = 1.5\text{--}2.0$ comes from observations: Wright *et al.* (1992), Minier *et al.* (2005) and Gordon *et al.* (2010). Details of the dust modeling process can be found in the review by Draine *et al.* (2003). We can estimate the dust grain emissivity exponent from observations at two frequencies ν_1 and ν_2 :

$$\beta = \frac{\log \frac{F_{\nu_2}}{F_{\nu_1}} + \log \frac{(e^{h\nu_2/kT_{\text{dust}}} - 1)}{(e^{h\nu_1/kT_{\text{dust}}} - 1)}}{\log \frac{\nu_2}{\nu_1}} - 3 \quad (17)$$

where F_ν is the source flux density, ν the frequency of the observations, and T_{dust} the dust temperature. In this work the dust grain emissivity index β is determined for W31C and W33A using the millimeter ($\lambda_1 = 1.2$ mm; $\nu_1 = 250$ GHz) data obtained with SIMBA and submillimeter ($\lambda_2 = 450$ μm ; $\nu_2 = 660$ GHz) SCUBA data. We derive $\beta = 1.85 \pm 0.55$ (W31C) and $\beta = 1.7 \pm 0.50$ (W33A). The uncertainty in β is typically 30% for the 20–50 K temperature range (Hill *et al.* 2006). The spectral indices for the other sources are taken from literature: Lis *et al.* (1993) for SgrB2(N) and SgrB2(M) and Zapata *et al.* (2011) for DR21(OH). The HDO lines studied here are seen in emission and the model intensities are not sensitive to the exact value of β , especially for $T > 30$ K. Therefore the dust grain emissivity index is fixed, and not a free parameter in the fits. The known values of β in our target sources with the continuum data from SCUBA observations were used to constrain the density and temperature distributions.

5. Results

5.1. SgrB2(N)

Observed spectrum and Gaussian fit of the 464.925 GHz HDO line toward SgrB2(N) together with the best-fit model are shown in Fig. 3 by black, blue and red lines, respectively. Model results for SgrB2(N) are presented in Table 6. We obtain the best fit for: $T_0 = 270$ K, $n_0 = 2.5 \times 10^8 \text{ cm}^{-3}$, $X_{\text{in}} = 3.0 \times 10^{-8}$ and $X_{\text{out}} = 4.0 \times 10^{-11}$. Assuming an observational uncertainty of 20% for the HDO line measurement at 465 GHz we obtained $X_{\text{in}} = (2.4\text{--}3.6) \times 10^{-8}$ and $X_{\text{out}} = (3.2\text{--}4.8) \times 10^{-11}$.

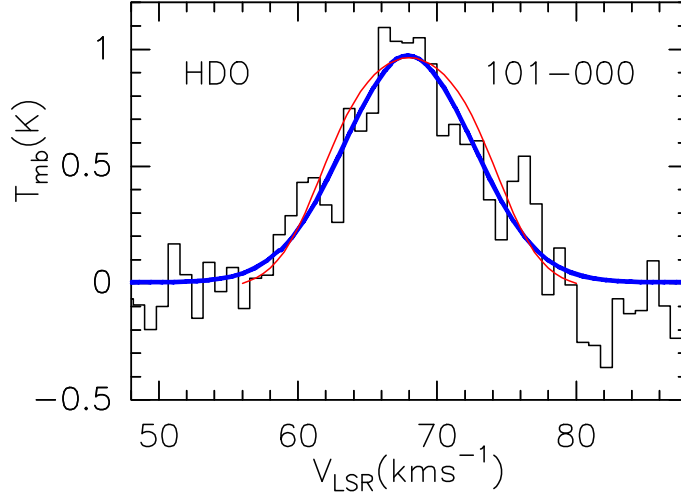


Fig. 3. Observed spectrum of the 464.925 GHz HDO line toward SgrB2(N). Gaussian fit is shown in blue, together with the best-fit model in red.

Table 6

Line intensities for the best fit model of SgrB2(N)

HDO transitions	Freq [GHz]	$T_{\text{obs}}^{\text{peak}}$ [K]	$T_{\text{mod}}^{\text{peak}} *$ [K]	A_{obs} [K km/s]	A_{mod} [K km/s]	$\frac{(A_{\text{obs}} - A_{\text{mod}})^2}{(A_{\text{obs}})^2}$
1 _{0,1} –0 _{0,0}	464.925	0.97	0.97	11.30	14.70	0.1
2 _{1,1} –2 _{1,2}	241.562	1.2	1.15	8.30	12.5	0.2
3 _{1,2} –2 _{2,1}	225.897	1.3	1.10	17.9	15.67	0.01
4 _{2,2} –4 _{2,3}	143.727	0.4	0.18	6.00	2.69	0.3
FOM = 0.61						

* $T_{mb_i}^{\text{peak}} \equiv T_i^{\text{peak}}$ where i : obs, mod

Fig. 4 shows fractional population of the HDO levels of the relevant features in our dataset calculated in our model. The bulk of emission in the high energy transitions is produced in the inner hot-core region where $T > 100$ K. The high-energy transitions are sensitive to changes in X_{in} . In the SgrB2(N) source this region has radius equal to $1.''2$, which corresponds to 0.05 pc (≈ 10000 a.u.).

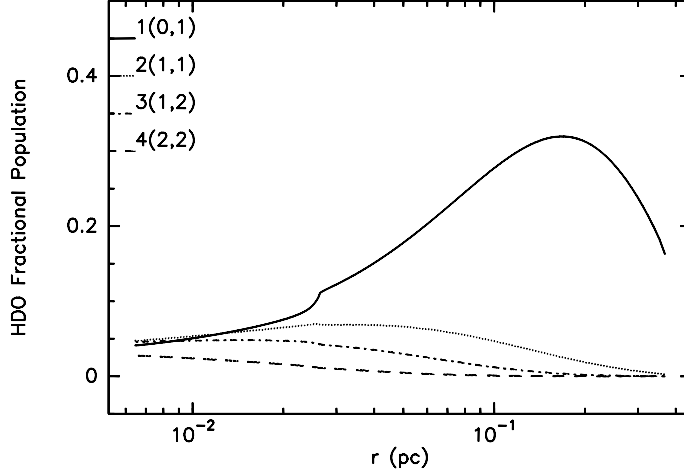


Fig. 4. Fractional population of the HDO energy levels as a function of the cloud's radius.

This is the reason why the high-energy transitions are sensitive to changes in X_{in} . On the other hand the 464.925 GHz transitions are sensitive primarily to X_{out} . This line arises predominantly in the cold envelope ($T < 100$ K). We conclude that the ground state rotational transition of HDO at 464.925 GHz is a very good probe of the fractional abundance in the outer envelope (consistent with the results of observed for the solar-type protostar IRAS 16293-2422, Parise 2005). The model reproduces very well the observed intensities of other transitions in our target source.

5.2. Others Sources

Observed spectra, Gaussian fits and the best-fit models of the ground state ($1_{0,1}-0_{0,0}$) rotational transition of HDO toward other target sources are shown in Fig. 5 by black, blue and red lines, respectively. Model results are presented in Table 7. We obtain the best fit for (Table 8):

SgrB2(M) : $T_0=200$ K, $n_0=1.2 \times 10^8 \text{ cm}^{-3}$, $X_{\text{in}}=2.0 \times 10^{-8}$, $X_{\text{out}}=1.1 \times 10^{-11}$,
W33A : $T_0=110$ K, $n_0=1.0 \times 10^7 \text{ cm}^{-3}$, $X_{\text{in}}=3.5 \times 10^{-8}$, $X_{\text{out}}=2.5 \times 10^{-10}$,
W31C : $T_0=150$ K, $n_0=8.0 \times 10^7 \text{ cm}^{-3}$, $X_{\text{in}}=2.0 \times 10^{-8}$, $X_{\text{out}}=4.6 \times 10^{-11}$,
DR21(OH) : $T_0=110$ K, $n_0=2.0 \times 10^6 \text{ cm}^{-3}$, $X_{\text{in}}=6.0 \times 10^{-9}$, $X_{\text{out}}=1.0 \times 10^{-12}$.

Table 7

Line intensities for the best fit models

HDO transitions	Freq [GHz]	$T_{\text{obs}}^{\text{peak}}$ [K]	$T_{\text{mod}}^{\text{peak}}$ [K]	A_{obs} [K km/s]	A_{mod} [K km/s]	$\frac{(A_{\text{obs}} - A_{\text{mod}})^2}{(A_{\text{obs}})^2}$
SgrB2(M)						
$1_{0,1}-0_{0,0}$	464.925	0.37	0.37	1.46	2.00	0.14
$3_{1,2}-2_{2,1}$	225.897	1.30	1.10	9.30	1.68	0.67
FOM = 0.81						
W33A						
$0_{0,1}-0_{0,0}$	464.925	0.19	0.19	1.30	1.70	0.10
Flux [Jy/beam]	509 GHz ^a	2.90	3.10		$\frac{(F_{\text{obs}} - F_{\text{mod}})^2}{(F_{\text{obs}})^2} =$	0.00
FOM = 0.10						
W31C						
$1_{0,1}-0_{0,0}$	464.925	0.36	0.36	3.80	4.20	0.01
Flux [Jy/beam]	509 GHz ^a	27.5	27.6		$\frac{(F_{\text{obs}} - F_{\text{mod}})^2}{(F_{\text{obs}})^2} =$	0.00
FOM = 0.01						
DR21(OH)						
$1_{0,1}-0_{0,0}$	464.925	0.15	0.15	0.40	0.48	0.04
FOM = 0.04						

^a SCUBA

Table 8

Best fit model parameters

Source	n_0 [cm ⁻³]	T_0 [K]	X_{in} [HDO]	Range	X_{out} [HDO]	Range
SgrB2(N)	2.5×10^8	270	3.0×10^{-8}	$2.4 - 3.6 \times 10^{-8}$	4.0×10^{-11}	$3.2 - 4.8 \times 10^{-11}$
SgrB2(M)	1.2×10^8	200	2.0×10^{-8}	$1.6 - 2.4 \times 10^{-8}$	1.1×10^{-11}	$0.9 - 1.3 \times 10^{-11}$
W31C	7.5×10^7	150	2.0×10^{-8}	$1.6 - 2.4 \times 10^{-8}$	4.6×10^{-11}	$3.7 - 5.5 \times 10^{-11}$
W33A	1.0×10^7	110	3.5×10^{-8}	$2.8 - 4.2 \times 10^{-8}$	2.5×10^{-10}	$2.0 - 3.0 \times 10^{-10}$
DR21(OH)	2.0×10^6	110	6.0×10^{-9}	$4.8 - 7.2 \times 10^{-8}$	1.0×10^{-12}	$0.8 - 1.2 \times 10^{-12}$

Assuming an observational uncertainty of 20% for the HDO line measurement at 464.925 GHz we obtained:

$$\begin{aligned}
X_{\text{in}} &= (1.6 - 2.4) \times 10^{-8} \text{ and } X_{\text{out}} = (0.9 - 1.3) \times 10^{-11} \text{ (SgrB2(M))}, \\
X_{\text{in}} &= (2.8 - 4.2) \times 10^{-8} \text{ and } X_{\text{out}} = (2.0 - 3.0) \times 10^{-10} \text{ (W33A)}, \\
X_{\text{in}} &= (1.6 - 2.4) \times 10^{-8} \text{ and } X_{\text{out}} = (3.7 - 5.5) \times 10^{-11} \text{ (W31C)}, \\
X_{\text{in}} &= (4.8 - 7.2) \times 10^{-9} \text{ and } X_{\text{out}} = (0.8 - 1.2) \times 10^{-12} \text{ (DR21(OH))}.
\end{aligned}$$

As data on the high excitation lines are missing for: W33A, W31C and DR21(OH) the inner abundance X_{in} is not as well constrained as in the other sources. Nevertheless the best fit values are similar.

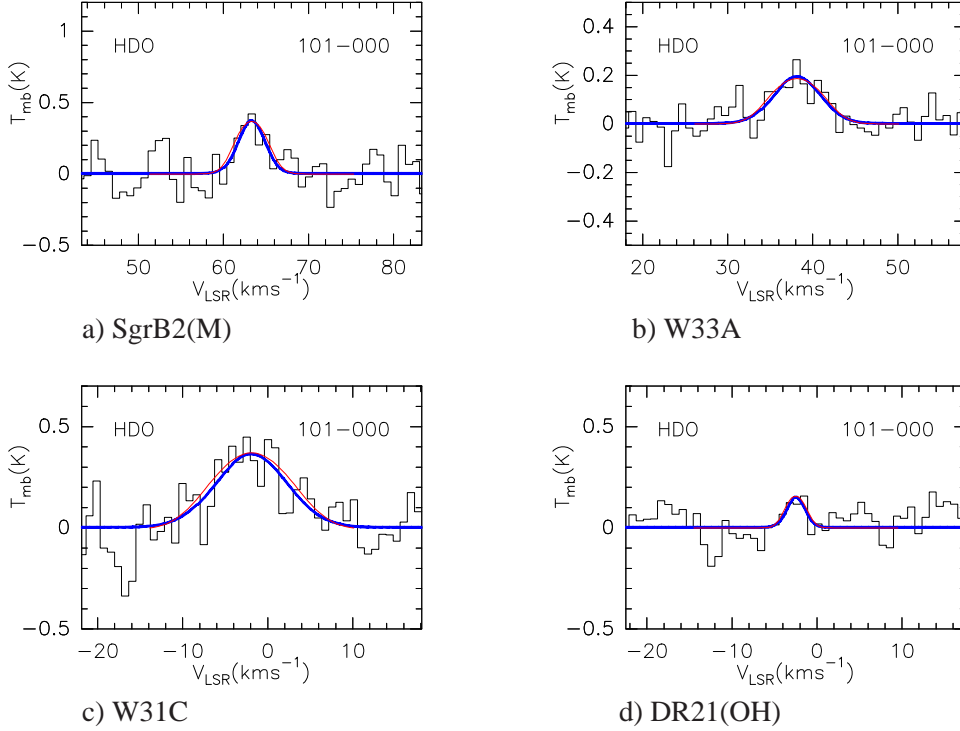


Fig. 5. Observed spectrum of the 464.925 GHz HDO line toward: *a)* SgrB2(M), *b)* W33A, *c)* W31C, *d)* DR21(OH). Gaussian fits are shown in blue, together with the best-fit models in red.

6. Discussion

The best fit HDO abundance in the cores ($T \geq 100$ K) and the outer envelopes ($T < 100$ K) of high-mass protostars are shown in Table 8. The HDO abundance ratio is varying between the inner and outer regions with HDO higher in the hot region and lower in the outer region. The high HDO abundance is interpreted as material recently desorbed from dust grains, thus the low HDO abundance indicates that most semiheavy water is still frozen-out onto dust grains. We could find in our sources the youngest DR21(OH) (Marseille *et al.* 2010) with the lowest value: $X_{\text{out}} = 1.0 \times 10^{-12}$ and the oldest W33A (de Wit *et al.* 2009) with the highest value: $X_{\text{out}} = 2.5 \times 10^{-10}$. This high value of the HDO abundance in the W33A source's outer envelope could be explained by a snow zone (Marseille and Cazaux 2011). Sublimation and condensation of water on dust particles has been considered to occur at the so-called snow line position, *i.e.*, where the temperature in the protostellar

environment is around 100 K. New results show that the condensation of water is not optimal near this position. Protostellar environments are known to be turbulent (*e.g.*, Padoan and Nordlund 2002, Mac Low *et al.* 2004), leading to the idea of an extended zone where bare and icy dust grains coexist, creating the so-called snow border. More precisely, the snow border allows a non-negligible abundance of water and HDO in the gas phase to exist even at cold temperatures. HDO is also partially reformed by ion-molecule reactions (Coutens *et al.* 2014). At later times, the abundances of HDO in the outer envelope are increased *via* turbulence and chemical processes.

7. Summary

This paper has shown that ground-state HDO transition at 464.925 GHz is a very good probe of a cold, outer envelope. We derive HDO abundances of $X_{\text{in}} = (0.6\text{--}3.5) \times 10^{-8}$ (for $T \geq 100$ K) and $X_{\text{out}} = (0.1\text{--}25) \times 10^{-11}$ (for $T < 100$ K) in the five high-mass star forming regions (Table 8). The inner HDO abundances are consistent with recent studies of high-mass protostars (Coutens *et al.* 2014, Liu *et al.* 2013, Kulczak–Jastrzębska in preparation).

The model has a simple geometry and physical structure, it does not take into account radiative pumping or the turbulent velocity field, which is responsible for the line width. Nevertheless, the model is successful in reproducing the observed HDO integrated line intensities. In addition, it is easy to implement and it is not CPU time consuming.

Acknowledgements. This work was partly supported by the Science and High Education Ministry of Poland grant DEC-2011/01/B/ST9/02229. This research is based on observations from the Caltech Submillimeter Observatory, which is operated by the California Institute of Technology under cooperative agreement with the National Science Foundation (AST-0838261). The author is grateful to Maryvonne Gerin and Darek Lis for helpful discussion and an anonymous referee for his comments.

REFERENCES

- André, R.I., Ward-Thompson, D., and Barsony, M. 2000, in: “Protostars and Planets IV”, Ed. V.Mannings, A.P. Boss, p. 59.
- Araya, E.D., Kurtz, S., Hofner, P., and Linz, H. 2009, *ApJ*, **698**, 1321.
- Bergin, E.A., and Tafalla, M. 2007, *Ann. Rev. Astron. Astrophys.*, **45**, 339.
- Beuther, H., Schilke, P., Menten, K.M., Motte, F., Shidharan, T.K., and Wyrowski, F. 2002, *ApJ*, **566**, 945.
- Cazaux, S., Caselli, P., and Spaans, M. 2011, *ApJ*, **741**, L34.
- Coutens, A., *et al.* 2012, *A&A*, **539**, 132.
- Coutens, A., *et al.* 2014, *MNRAS*, **445**, 1299.

- de Wit, W.J., Hoare, M.G., Oudmaijer, R.D., and Mottram, J.C. 2007, *ApJ*, **671**, 169.
- de Wit, W.J., *et al.* 2009, *A&A*, **494**, 157.
- Draine, B.T. 2003, *Ann. Rev. Astron. Astrophys.*, **41**, 241.
- Faundez, S., Bronfman, L., Garay, G., Chini, R., Nyman, L.-A., and May, J. 2004, *A&A*, **426**, 97.
- Faure, A., Wiesenfeld, L., Scribano, Y., and Ceccarelli, C. 2012, *MNRAS*, **420**, 699.
- Fraser, H.J., Collins, M.P., McCoustra, M.R., and Williams, D.A. 2001, *MNRAS*, **327**, 1165.
- Fraser, H.J., Bissshop, S.E., Pontoppidan, K.M., Tielens, A.G.G.M., and van Dishoeck, E.F. 2005, *MNRAS*, **356**, 1283.
- Gensheimer, P.D., Mauersberger, R., and Wilson, T.L. 1996, *A&A*, **314**, 281.
- Goldsmith, P.F., Snell, R.L., Hagesawa, T., and Ukita, N. 1987, *ApJ*, **314**, 525.
- Gordon, K.D., *et al.* 2010, *A&A*, **518**, L89.
- Hatchell, J., and van der Tak, F.F.S. 2003, *A&A*, **409**, 589.
- Helmich, F.P., van Dishoeck, E.F., and Jansen, D.J. 1996, *A&A*, **313**, 657.
- Hildebrand, R.H. 1983, *Quarterly Journal of the Royal Astronomical Society*, **24**, 267.
- Hill, T., Thompson, M.A., Burton, M.G., Walsh, A.J., Minier, V., Cunningham, M.R., and Pierce-Price, D. 2006, *MNRAS*, **368**, 1223.
- Iben, J. 1965, *A&A*, **141**, 933.
- Jacq, T., Wamsley, C.M., Henkel, C., Baudry, A., Mauersberger, R., and Jewell, P.R. 1990, *A&A*, **228**, 447.
- Lis, D.C., Goldsmith, P.F., Carlstrom, J.E., and Scoville, N.Z. 1993, *ApJ*, **402**, 238.
- Liu, F.C., Parise, B., Wyrowski, F., Zhang, Q., and Gusten, R. 2013, *A&A*, **550**, A37.
- Mac Low, M.-M., de Avillez, M.A., and Korpi, M.J. 2004, *Astrophysics and Space Science Library*, **315**, 339.
- Mangnum, J.G., Wootten, A., and Mundy, L.G. 1992, *ApJ*, **388**, 467.
- Marseille, M.G., van der Tak, F.F.S., Herpin, F., and Jacq, T. 2010, *A&A*, **522**, 40.
- Marseille, M.G., and Cazaux, S. 2011, *A&A*, **532**, 60.
- Millar, T.J., Bennett, A., and Herbst, E. 1989, *ApJ*, **340**, 906.
- Minier, V., Burton, M.G., Hill, T., Pestalozzi, C.R., Purcell, C.R., Garay, G., Walsh, A.J., and Longmore, S. 2005, *A&A*, **429**, 945.
- Padoan, P., and Nordlund, A. 2002, *ApJ*, **576**, 870.
- Parise, B., *et al.* 2005, *A&A*, **431**, 547.
- Pety, J. 2005, SF2A-2005: Semaine de l'Astrophysique Francaise, Eds. F. Casoli, T. Contini, J.M. Hameury and L. Pagani. *EdP-Sciences, Conference Series* p. 721.
- Pickett, H.M., Poynter, R.L., Cohen, E.A., Delitsky, M.L., Pearson, J.C., and Muller, H.S.P. 1998, *Journal of Quantitative Spectroscopy and Radiative Transfer*, **60**, 883.
- Phillips, T.G., and Vastel, C. 2003, in: "Chemistry as Diagnostic of Star Formation", Eds. C. Curry and M. Finch, p. 3.
- Reid M.J., Menten, and K.M., Zheng, X.W., Brunthaler, A., and Xu, Y. 2009, *ApJ*, **705**, 1548.
- Rybicki, G.B., and Hummer, D.G. 1991, *ApJ*, **245**, 171.
- Rygl, K.L.J., *et al.* 2012, *A&A*, **539**, 79.
- Sanna, A., *et al.* 2014, *ApJ*, **781**, 108.
- Scoville, N.Z., Solomon, P., and Penzias, A.A. 1975, *ApJ*, **201**, 352.
- Shu, F.H. 1977, *ApJ*, **214**, 488.
- Sollis, P.K. 2005, in PhDT: "Accretion and outflow in massive star formation: Observational studies at high angular resolution".
- Solomon, P.M., and Woolf, N.J. 1973, *ApJ*, **180**, 89.
- Taquet, V., *et al.* 2013, *A&A*, **550**, 127.
- Thompson, M.A., Hatchell, J., Walsh, A.J., Macdonald, G.H., and Millar, T.J. 2006, *A&A*, **453**, 1003.
- van der Tak, F.F.S., van Dishoeck, E.F., Evans, N.J., and Blake, G.A. 2000, *ApJ*, **537**, 283.
- Vastel, Ch., Phillips, T.G., Ceccarelli, C., and Pearson, J. 2003, *ApJ*, **593**, L97.
- Vastel, Ch., Phillips, T.G., and Yoshida, H. 2004, *ApJ*, **606**, L127.
- Viti, S., and Williams, D.A. 1999, *MNRAS*, **305**, 755.

- Walmsley, C.M., and Schilke, P. 1992, in: "Astrochemistry of Cosmic Phenomena", *Proceedings of the International Astronomical Union*, p. 251.
- Wiesenfeld, L., Scribano, Y., and Faure, A. 2011, *Physical Chemistry Chemical Physics*, **13**, 8230.
- Wright, M., Sandell, G., Wilner, D.J., and Plambeck, R.L. 1992, *ApJ*, **393**, 225.
- Zapata, L.A., Schmid-Burgk, J., and Menten, K.M. 2011, *A&A*, **529**, 24.
- Zmuidzinas, J., Blake, A., Carlstrom, J., Keene, J., and Miller, D. 1995, *ApJ*, **447**, L125.

Appendix \mathcal{B}

*Analysis of Low Excitation Transition
toward the High-mass Star-forming Regions
G34.26+0.15, W51e₁/e₂ and W49N*



Analysis of Low Excitation HDO Transitions toward the High-mass Star-forming Regions G34.26+0.15, W51e₁/e₂, and W49N

Magda Kulczak-Jastrzebska

Astronomical Observatory of the Jagiellonian University, 30-244 Orla 171, Kraków, Poland; kulczak@oa.uj.edu.pl

Received 2015 May 6; revised 2016 December 10; accepted 2016 December 13; published 2017 January 23

Abstract

We present observations of the ground state $1_{0,1}-0_{0,0}$ rotational transition of HDO at 464.925 GHz and the $1_{1,0}-1_{0,1}$ transition at 509.292 GHz, toward three high-mass star-forming regions: G34.26+0.15, W49N, and W51e₁/e₂, carried out with the Caltech Submillimeter Observatory. For the first time, the latter transition is observed from the ground. The spectra are modeled, together with observations of higher-energy HDO transitions, as well as submillimeter dust continuum fluxes from the literature, using a spherically symmetric radiative transfer model to derive the radial distribution of the HDO abundance in the target sources. The abundance profile is divided into an inner hot core region, with kinetic temperatures higher than 100 K, and a cold outer envelope with lower kinetic temperatures. The derived HDO abundance with respect to H₂ is $(0.3-3.7) \times 10^{-8}$ in the hot inner region ($T > 100$ K) and $(7.0-10.0) \times 10^{-11}$ in the cold outer envelope. We also used two H₂¹⁸O fundamental transitions to constrain the H₂O abundances in the outer envelopes. The HDO/H₂O ratios in these cold regions are found to be $(1.8-3.1) \times 10^{-3}$ and consequently are higher than in the hot inner regions of these sources.

Key words: ISM: abundances – ISM: molecules – stars: massive – stars: protostars

1. Introduction

During the cold phase preceding the formation of stellar objects, molecules freeze-out onto dust grains, forming H₂O-dominated ice mantles mixed with other less-abundant species. The low temperature and disappearance of most molecules, especially CO, from the gas phase trigger a peculiar chemistry leading to high abundances of deuterated species. Molecules tend to attach a D atom rather than an H atom because deuterated species have larger reduced masses and consequently lower binding energies, arising from lower zero-point vibrational energies. Ion–molecule reactions in the gas phase (Brown & Millar 1989) and reactions on the grain surfaces (Tielens 1983) are the two possible mechanisms responsible for deuterium enrichments in heavy molecules. The reactions involved are exothermic, which is why significant deuteration levels can be expected in the cold ISM. In the warmer phase, very little fractionation is expected to occur because the energy barrier could be overcome by the elevated temperature. However, at the temperatures deduced for the hot core regions (100–200 K) the ice mantles evaporate and the gas again becomes enriched in deuterated species, with abundances elevated compared to the cosmic D/H ratio for a short period, before the chemistry reaches steady-state. These enhancements in the hot cores reflect, to some degree, the grain mantle composition in the earlier, colder cloud phases. Although the processes leading to the water deuteration are not fully understood, they are clearly related to the grain-surface chemistry, and the observed HDO/H₂O ratio reveals the chemical and physical history of the protostellar materials (Codella et al. 2010; Cazaux et al. 2011). A recent review of water chemistry can be found in van Dishoeck et al. (2013) and a review of the latest observational results from *Herschel* in van Dishoeck et al. (2014).

Early studies of water deuterium fractionation in high-mass hot cores were performed almost twenty years ago, when the submillimeter spectrum was largely inaccessible (Petuchowsky & Bennett 1988; Jacq & Wamsley 1990; Schulz et al. 1991;

Gensheimer et al. 1996; Helmich et al. 1996). The HDO abundance has been recently determined toward the high-mass hot core G34.26+0.15 and the intermediate-mass protostar NGC7129 FIRS2 (Fuente et al. 2012; Liu et al. 2013; Coutens et al. 2014). Here, we present the new observations of the ground state rotational transition of HDO at 464.925 GHz and the first excited transition at 509.292 GHz toward three high-mass star-forming regions: G34.26+0.15, W51e₁/e₂, and W49N. The combination of data taken with the same telescope of both the ground state transition ($1_{0,1}-0_{0,0}$) and the first excited line ($1_{1,0}-1_{0,1}$) provide better constraints on the source structure. These HDO transitions are studied for the first time, to probe the structure of the envelope of the W51e₁/e₂ and W49N hot cores. In this paper, we aim at determining the HDO fractional abundances relative to H₂ in the inner and outer region of the core in our target sources, using the static radiative transfer code of Zmuidzinas et al. (1995). We also used two H₂¹⁸O fundamental transitions observed by Flagey et al. (2013) to constrain the H₂O abundance and the HDO/H₂O ratio in the outer envelopes.

2. Observations

Water is difficult to study from the ground, due to its strong presence in the Earth's atmosphere. However, many HDO lines, including the ground state $1_{0,1}-0_{0,0}$ rotational transition and the $1_{1,0}-1_{0,1}$ excited transition studied here, lie in atmospheric windows, where observations are possible from high sites, under good weather conditions. Table 1 lists the HDO transitions included in the present study and the H₂¹⁸O transitions which we use to constrain the HDO/H₂O ratio in the outer envelope.

2.1. Source Description

The $1_{0,1}-0_{0,0}$ ground-state rotational transition of HDO at 465 GHz and the $1_{1,0}-1_{0,1}$ transition at 509 GHz were observed toward three high-mass star-forming regions are listed in

Table 1
Observed and Modeled HDO and H₂¹⁸O Rotational Transitions

Species	Transition	Frequency (GHz)	E_{up} (K)	A_{ul} (s ⁻¹)	Telescope	FWHM (")
HDO	1 _{0,1} –0 _{0,0}	464.925	22.3	1.69×10^{-4}	CSO	15.7
	1 _{1,0} –1 _{0,1}	509.292	47.0	2.30×10^{-3}	CSO	15.7
	2 _{1,1} –2 _{1,2}	241.562	95.2	1.18×10^{-5}	IRAM	12.0
	3 _{1,2} –2 _{2,1}	225.897	167.6	1.31×10^{-5}	IRAM	13.0
	4 _{2,2} –4 _{2,3}	143.727	319.2	2.80×10^{-6}	IRAM	17.0
	5 _{2,3} –4 _{3,2}	255.050	437.2	1.78×10^{-5}	IRAM	12.0
p-H ₂ ¹⁸ O	1 _{1,1} –0 _{0,0}	1101.698	53.9	1.79×10^{-2}	HIFI	19.2
o-H ₂ ¹⁸ O	2 _{1,2} –1 _{0,1}	1655.868	114.0	1.26×10^{-2}	HIFI	12.8

Note. Spectroscopic data from the JPL spectral line catalog (Pickett et al. 1998), <http://www.spec.jpl.nasa.gov>. CSO data: this work; IRAM data from Jacq & Wamsley (1990); *Herschel*/HIFI data from Flagey et al. (2013).

Table 2
Source Sample

Source	α (J2000)	δ (J2000)	D (kpc)
G34.26+0.15	18 53 18.6	+01 14 57.7	3.8 ^a
W51e ₁ /e ₂	19 23 43.9	+14 30 25.9	5.4 ^b
W49N	19 10 13.2	+09 06 12.0	11.4 ^c

Notes.

^a Fish et al. (2003).

^b Sato et al. (2010).

^c Gwinn et al. (1992).

Table 2. All the sources are characterized by strong millimeter continuum and mid-infrared emission, characteristic of the early stage of high-mass star formation.

G34.26+0.15 is one of the best studied high-mass star-forming regions in the Milky Way. Embedded within this molecular cloud is a hot core, which exhibits strong H₂O maser emission and high abundances of saturated molecules (Macdonald et al. 1996); two unresolved UCHII regions, labeled A and B; a more evolved H II region with a cometary shape; and an extended, ring-like H II region (Reid & Ho 1985). Based on narrow-band mid-infrared imaging of the complex, Campbell et al. (2000) concluded that the same star is responsible for ionization of the cometary H II component (C) and heating the dust, but is not interacting with the hot core seen in the molecular emission. At a 12'' resolution, Hunter et al. (1998) also found the peak of the 350 μ m emission to coincide with the component C of the UCHII region.

The radio continuum emission of W51 shows three separate components: W51 IRS1, W51 IRS2, and W51 Main. W51 Main is defined by a group of OH and H₂O masers near several UCHII regions. The continuum emission from ultra-compact H II regions was resolved into compact components labeled W51e₁ to W51e₈ (Zhang & Ho 1997). Of these, e₁ and e₂ are the brightest in high-resolution continuum maps.

The star-forming region W49N contains at least a dozen UCHII regions powered by OB-type stars arranged in a ring 2 pc in diameter (De Pree et al. 2000). Evidence that star formation is still in progress within W49N comes from strong H₂O maser emission and strong millimeter continuum emission attributed to dust condensations (Sievers et al. 1991).

2.2. Observations

Observations of the 465 and 509 GHz HDO transitions presented here were carried out in 2012 June–August, using the 10.4 m Leighton Telescope of the Caltech Submillimeter Observatory (CSO) on Mauna Kea, Hawaii. We used the new wideband 460 GHz facility SIS receiver and the FFTS backend that covers the full 4 GHz intermediate frequency (IF) range with a 270 kHz channel spacing. Pointing of the telescope was checked by performing five-point continuum scans of planets and strong dust continuum sources. The spectra were obtained in antenna temperature units T_A^* , and then converted to the main beam brightness temperature, T_{mb} , via the relation $T_A^* = \eta_{\text{mb}} T_{\text{mb}}$; η_{mb} is the CSO main-beam efficiency, which is found to be $\sim 37\%$ at 460 GHz from total power observations of planets. The absolute calibration uncertainty of the individual measurements is $\sim 20\%$.

In addition to the new CSO data, we included in our analysis previously published observations of higher-energy transitions (Jacq & Wamsley 1990) toward our target sources. We used the reduced HIFI data of the H₂¹⁸O transitions at 1101.698 and 1655.868 GHz. The HDO and H₂¹⁸O lines parameters are listed in Table 3. The H₂¹⁸O ground state transitions have been previously presented by Flagey et al. (2013).

The data processing was done using the IRAM GILDAS software package (Pety 2005). We measured the line parameters: central velocity V_{LSR} , the full-width at half maximum (FWHM) ΔV , peak intensity T^{peak} , by fitting a single Gaussian profile to the data (in T_{mb} units). The integrated line intensity is equal to $W_i = \int T_i dV$, where i either refers to observations (obs) or models (mod).

We also used *Herschel*/HIFI data at 893 GHz (C. Vastel et al. 2016, in preparation) obtained by the PRISMAS guaranteed time key program, and the SCUBA data at 353 GHz that provide an accurate determination of the source continuum flux.

The PRISMAS continuum observations were obtained in the double beam switching mode. At 800 GHz, the HIFI beam size is 26''5 and the instrument gain is 469 Jy K⁻¹ (Roelfsema et al. 2012).

3. Determination of the HDO and H₂O Abundance

3.1. Modeling

The goal of this study is to determine the HDO fractional abundance in three high-mass stars formation regions. To

Table 3
HDO and H₂¹⁸O Lines Parameters

Source	Species	Frequency (GHz)	V_{LSR} (km s ⁻¹)	ΔV (km s ⁻¹)	$T_{\text{obs}}^{\text{peak}}$ (K)	W_{obs} (K km s ⁻¹)	W_{mod} (K km s ⁻¹)
G34.26	HDO	143 ^a	57.7 (0.2)	6.9 (0.4)	0.4	2.6 (0.2)	1.7
		225 ^a	57.4 (0.3)	6.6 (0.4)	1.2	8.4(0.7)	11.4
		241 ^a	57.7 (0.3)	7.0 (0.6)	1.8	13.2(1.0)	12.0
		255 ^a	57.7 (0.9)	8.8 (3.0)	0.6	6.0 (0.6)	3.4
		465 ^b	58.0 (0.1)	6.4 (0.2)	1.8	12.1(0.3)	13.2
		509 ^b	58.4 (0.2)	6.0 (0.7)	0.8	5.5 (0.8)	10.4
	H ₂ ¹⁸ O	1102 ^c	61.1 (0.1)	3.5 (0.2)	-0.9	-3.4(0.2)	-2.6
		1656 ^c	61.1 (0.2)	6.5(0.0)	-1.7	-11.7 (0.9)	-13.5
W51e ₁ /e ₂	HDO	225 ^a	55.0 (0.4)	9.2 (0.9)	0.6	6.2(0.6)	4.5
		241 ^a	55.6 (1.6)	5.7 (1.6)	0.8	4.7(1.1)	5.5
		255 ^a	53.9 (2.0)	15.6 (6.0)	0.3	5.6(2.0)	2.1
		465 ^b	57.1 (0.2)	6.4 (0.4)	1.3	8.7(0.4)	10.7
		509 ^b			<0.9 ^d	<3.5 ^e	4.1
	H ₂ ¹⁸ O	1102 ^c	58.3 (0.1)	6.1 (0.3)	-0.9	-5.8(0.3)	-5.7
		1656 ^c	58.7 (0.1)	8.3(0.3)	-2.1	-18.3 (0.6)	-20.0
W49N	HDO	465 ^b	8.5(0.2)	12.0 (0.5)	0.8	10.8 (0.4)	9.4
		509 ^b	8.1 (0.7)	12.9 (1.5)	0.7	10.2 (1.2)	8.9
	H ₂ ¹⁸ O	1102 ^c	10.3 (0.2)	9.6 (0.4)	-0.7	-7.5(0.3)	-7.7
		1656 ^c	10.4 (0.1)	12.0(0.1)	-2.3	-30.2 (0.3)	-26.4

Notes.

^a Jacq & Wamsley (1990).

^b This work.

^c Flagey et al. (2013).

^d $3 \times r_{\text{ms}}$ upper limit.

^e 3σ (K kms⁻¹) = $3 \times \text{rms} \times \sqrt{2} \times d\nu \times \Delta V$ with rms (root mean square) in K, $d\nu$, the channel width in km s⁻¹ and ΔV , the FWHM in km s⁻¹. We assumed $\Delta V = 6.4$ km s⁻¹, which is the 465 GHz emission line width.

reproduce the observed line intensities (Table 3), the static radiative transfer code of Zmuidzinas et al. (1995) is used. The model cloud is divided into 200 radial shells, and the code uses a multilevel accelerated lambda-iteration method (Rybicki & Hummer 1991) to solve for the HDO-level populations and the line and continuum radiative transfer in a self-consistent fashion. This radiative transfer program takes into account the excitation of HDO molecules by collisions, line radiation, and dust continuum radiation at the HDO line frequencies. However, IR radiative pumping through HDO vibrationally excited levels and the large-scale velocity field, characteristic of infall or expansion, are not included. The HDO collisional rates used in this study were recently computed by Faure et al. (2012) and Wiesenfeld et al. (2011) for ortho-H₂ and para-H₂ in the temperature range 5–300 K and for all rotational transitions with an upper energies less than 444 K. In the modeling, we assumed a constant ortho-to-para ratio (OPR) of H₂ equal to 3. The ortho and para H₂O collisional rates with ortho and para H₂ were taken from the LAMDA data base (Schröier et al. 2005; Daniel et al. 2011). These rates were calculated for temperatures in the range from 5 to 1500 K including energy levels up to 2000 K above ground. The same

collisional rates are used for the H₂¹⁸O isotopologue. The limitation imposed by the radiative transfer code is to use a single collisional partner in the calculations. We assume that all hydrogen is in the ortho state.

We carried out model calculations from the inner core radius, r_{min} , to the outer radius, r_{max} (with $r_{\text{max}}/r_{\text{min}} \sim 100$ for all sources; Hatchell & van der Tak 2003). The distance of the edge of the core from the star is set at $r_{\text{min}} \sim 2.0 \times 10^{16}$ cm or ~ 1000 au, with no dust emission seen at the smaller radii. The lack of submillimeter emission in the core centers could be due to optical depth effects or a central cavity (van der Tak et al. 2000). We adopted a dust-to-gas ratio of 1:100 and a power-law H₂ density distribution of the form:

$$n(r) = n_0 \left(\frac{r}{r_{\text{min}}} \right)^{-1.5}, \quad (1)$$

where n_0 is the H₂ density at the reference radius ($r_{\text{min}} = 1000$ au). The power-law index was set to 1.5, in accordance with the static infall theory in the inner part of the object (Shu 1977; van der Tak et al. 2000; Beuther et al. 2001; Marseille et al. 2010). We assumed that the gas and dust radial

temperature profiles follow a power law (Viti & Williams 1999):

$$T(r) = T_0 \left(\frac{r}{r_{\min}} \right)^{-0.5}, \quad (2)$$

where T_0 represents the maximum temperature of dust grains. We assumed that, at densities found in the hot cores, the gas temperature is equal to the dust temperature.

3.2. Dust Emissivity Index β

When molecules deplete inside prestellar cores, dust emission may represent the best tracer of the gas density distribution just prior to the onset of gravitational collapse. The dust continuum optical depth is described by a power-law frequency dependence, $\tau \propto \nu^\beta$, and to fit the observed spectral energy distribution, the knowledge of the grain emissivity spectral index, β , is required. The dust emissivity index depends on the dust grain composition, size, and temperature (Hildebrand 1983; Goldsmith et al. 1997). Details of the dust-modeling process can be found in the reviews by Draine (2013) and Li & Greenberg (2003). Observationally, there have been many attempts at determining and explaining β . Typical values of β range between 1 and 2, with further support for $\beta = 1.5$ – 2.0 coming from observations: Wright et al. (1992), Minier et al. (2005), and Gordon et al. (2010). Planck Collaboration XIV (2014) used *Planck* HFI data with ancillary radio data to study the emissivity index. They computed a median value of far-infrared spectral index $\beta_{\text{FIR}} = 1.88 \pm 0.08$ at the high-frequency *Planck* channels ($\nu \geq 353$ GHz) and a median value of spectral index $\beta_{\text{mm}} = 1.6 \pm 0.06$ at millimeter wavelengths ($\nu < 353$ GHz). We can estimate the dust grain emissivity exponent from observations at two frequencies ν_1 and ν_2 (Hill et al. 2006):

$$\beta = \frac{\log \frac{F_{\nu_2}}{F_{\nu_1}} + \log \frac{(e^{h\nu_2/kT_{\text{dust}}} - 1)}{(e^{h\nu_1/kT_{\text{dust}}} - 1)}}{\log \frac{\nu_2}{\nu_1}} - 3, \quad (3)$$

where F_ν is the source flux density, ν the frequency of the observations, and T_{dust} the dust temperature. In this work, the dust grain emissivity index β is determined for G34.26 using the millimeter ($\lambda_1 = 1.2$ mm; $\nu_1 = 250$ GHz) data obtained with SIMBA and submillimeter ($\lambda_2 = 450$ μm ; $\nu_2 = 660$ GHz) SCUBA data. We derive $\beta = 1.6 \pm 0.48$. The uncertainty in β is typically 30% for the 20–50 K temperature range (Hill et al. 2006). The spectral index for the other sources is taken from literature: Ward-Thompson & Robson (1990) for W49N and from Gordon & Jewell (1987) for W51. The HDO lines studied here are seen in emission, and the model intensities are not sensitive to the exact value of β , especially for $T > 30$ K. That is why the dust grain emissivity index is fixed, and not a free parameter, in the fits.

The values of β in our target sources, as well as the continuum fluxes from SCUBA and *Herschel*/HIFI observations, are listed in Table 4. These are used to constrain the density and temperature distributions as input to the line modeling.

Table 4
Continuum Flux Densities and Grain Emissivity Exponents

Source	$F_{353}^{\text{a,b}}$ (Jy/beam)	F_{509}^{c} (Jy/beam)	F_{893}^{c} (Jy/beam)	β
G34.26+0.15	56.1	310	1320	1.6 ^d
W51e ₁ /e ₂		400	1490	1.7 ^e
W49N		320	1450	1.8 ^f

Notes.

^a F_ν , the source flux density, ν the frequency of the observations in GHz.

^b SCUBA; the accuracy is about 6% (Thompson et al. 2006).

^c *Herschel*; the accuracy is about 10%.

^d SIMBA and SCUBA observations (Hill et al. 2006).

^e Ward-Thompson & Robson (1990).

^f Gordon & Jewell (1987).

3.3. Modeling Procedure

We approximated the radial variation of the HDO fractional abundance, $X = n(\text{HDO})/n(\text{H}_2)$, as a step function with an enhanced abundance X_{in} in the inner region where $T \geq 100$ K, and a lower value X_{out} for the outer envelope where $T < 100$ K. Laboratory studies indicate that the evaporation temperature lies in the 90–110 K range, depending on the ice composition and structure (Fraser et al. 2005). In this work, the sublimation temperature of water, $T = 100$ K (Fraser et al. 2001), is applied as the jump temperature. The model uses the following free parameters: n_0 , T_0 and X_{in} (for $T \geq 100$ K), and X_{out} (for $T < 100$ K). We determine the continuum flux density per beam at 353 GHz (850 μm), 509 GHz (590 μm), and 893 GHz (336 μm) from the model.

Finally, the synthetic spectra and continuum emission are convolved to the appropriate telescope beam size for comparison with the observations. We minimize the “figure of merit” (FOM) with the method of Jacq & Wamsley (1990) to find the best model of the source. The FOM is computed from the observed and modeled spectra and continuum fluxes according to the following formula:

$$\text{FOM} = \text{FOM}_1 + \text{FOM}_2$$

$$= \sum_n \frac{(T_{\text{obs}} - T_{\text{mod}})^2}{(T_{\text{obs}})^2} + \sum_m \frac{(F_{\text{obs}} - F_{\text{mod}})^2}{(F_{\text{obs}})^2} \quad (4)$$

for a set of n spectral lines and m continuum flux densities. The inner and outer HDO abundances are constrained by the spectral line data (FOM₁), whereas model parameters describing the density and temperature distribution are constrained primarily by the continuum SED (FOM₂). To determine the uncertainty of X_{in} and X_{out} , we performed χ^2 analysis. In analogy to the Lampton method (Lampton et al. 1976), we define $S \equiv \text{FOM}_1/\sigma^2 = \sum_n \frac{(T_{\text{obs}} - T_{\text{mod}})^2}{(\sigma T_{\text{obs}})^2}$, where n is the number of spectral lines. The σ within analysis χ^2 includes a calibrations uncertainty of 20% for all individual measurements. The difference, $\Delta S \equiv S_{\text{true}} - S_{\text{min}}$ is distributed as χ^2 with p degrees of freedom (here: $p = 2$; X_{in} and X_{out}). By $\Delta S \sim \chi_p^2$ (“ \sim ”—“is distributed as”) we mean for any number L probability: $\text{Prob}(\Delta S > L) = \text{Prob}(\chi_p^2 > L)$. With the limiting contour value S_L defined as $S_{\text{min}} + L$, $\text{Prob}(\Delta S > S_L - S_{\text{min}}) = \text{Prob}(S_{\text{true}} > S_L) = \text{Prob}(\chi_p^2 > S_L - S_{\text{min}})$. $\text{Prob}(S_{\text{true}} > S_L)$ is the probability α of the contour

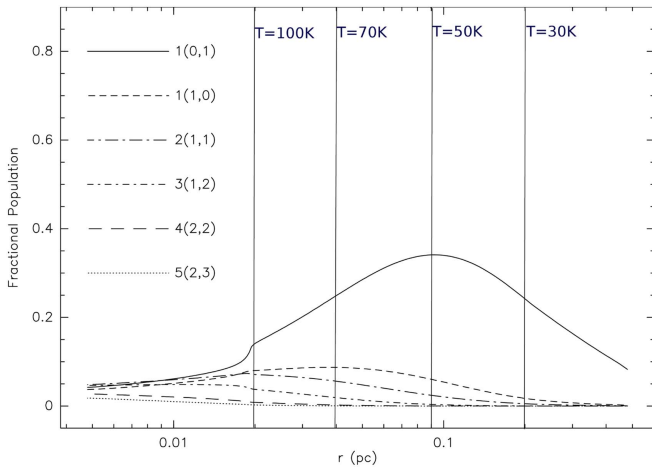


Figure 1. Fractional population of the HDO energy levels as a function of the radius of the cloud.

failing to enclose the true value, hence $\alpha = \text{Prob}(\chi_p^2 > S_L - S_{\min})$. The α -point of χ^2 distribution is defined by $\alpha \equiv \text{Prob}[\chi_p^2 > \chi_p^2(\alpha)]$. Significance α is $S_L = S_{\min} + \chi_p^2(\alpha)$. In this expression, $\chi_p^2(\alpha)$ is the tabulated value of χ^2 distribution for p degrees of freedom and significance α . Equivalently, any one observation's contour has a confidence $C = 1 - \alpha$ of enclosing the true parameter vector. The required contours for significance are 1σ , 2σ , and 3σ , which respectively represent a confidence of 68.3%, 95.4%, and 99.7% of enclosing the true value of X_{in} and X_{out} . The contours correspond to $S_L = S_{\min} + 2.17$, $S_L = S_{\min} + 6.17$, and $S_L = S_{\min} + 11.8$.

We used models with the same physical parameters as those used for HDO in the analysis of the H_2^{18}O data. The two H_2^{18}O fundamental transitions were modeled independently and the resulting ortho/para ratio of water is consistent with the high temperature value, given the modeling uncertainties.

3.4. Results

3.4.1. Origin of the Lines

Figure 1 shows fractional population of the HDO levels of the relevant features of our data set calculated in our model. The high-energy transitions are sensitive to changes in X_{in} . Indeed, the bulk of emission in the high-energy transitions is produced in the inner hot-core region where $T > 100$ K. In the G34.26 source, this region has a radius equal to $1''0$, which corresponds to 0.02 pc. This is in agreement with the interferometric observations of the HDO lines at 225 and 241 GHz by Liu et al. (2013). That is the reason why the high-energy transitions are sensitive to changes in X_{in} . On the other hand, the 465 and 509 GHz HDO transitions are sensitive primarily to X_{out} . The 509 GHz line arises predominantly in the region between the warm envelope and the cold region ($T \sim 50$ –100 K), whereas the 465 GHz transition is produced in the cold envelope ($T < 50$ K). The ground-state rotational transition of HDO at 465 GHz is consequently a very good probe of the abundance in the cold outer envelope, which is consistent with the results of Parise et al. (2004) for the solar-

type protostar IRAS 16293-2422. The 509 GHz transition provides particularly good constraints on the HDO abundance profile in the transition region between the hot core and the envelope, and should be included in future, more advanced models of HDO in high-mass star-forming regions. The model reproduces the observed intensities of different transitions in our target sources, with the exception of the 509 GHz line in G34.26. Although the signal-to-noise ratio of the observed 509 GHz spectrum is limited, it is clear that the best-fit model does not reproduce this line profile. The 509 GHz transition is formed in the part of the cloud where, within the scenario proposed by Rolfs et al. (2010), various feedback: thermal, radiative, or turbulent mechanisms are expected during the process of massive stars formation. In particular, it should be noted that, with the inclusion of velocity fields in their model, Coutens et al. (2014) successfully reproduced the 509 GHz line observed with *Herschel*/HIFI toward this same source. Other possibility is an accretion disk that is fed by the infalling envelope. This is also supported by observations made by Keto et al. (1987) of G34.26. The size of this possible disk is about 9000 au (0.05 pc) (Garay & Rodriguez 1990; Hajigholi et al. 2016) and agrees well with the place where the 509 GHz line arises (see Figure 1). This model of the G34.26 source (Hajigholi et al. 2016) neither confirms nor refutes the presence of an expansion in the inner parts of the envelope (Coutens et al. 2014). We concluded that the geometry and physical structure of our model is too simplistic, and that is why we could not to reproduce the 509 GHz line.

3.4.2. Target Sources

G34.26+0.15: Observed spectra (black line) and Gaussian fit (blue line) of the 465 and 509 GHz HDO transitions toward G34.26+0.15 along with the best-fit model (red line) are shown in Figure 2.

Model results are presented in Table 5. We obtain the best-fit model for: $T_0 = 200$ K, $n_0 = 1.0 \times 10^8 \text{ cm}^{-3}$, $X_{\text{in}} = 3.7 \times 10^{-8}$, and $X_{\text{out}} = 7.8 \times 10^{-11}$. We calculated continuum flux densities at 353, 509, and 893 GHz. The resulting uncertainties of X_{in} and X_{out} are shown in Figure 3 and listed in Table 8.

Observed and modeled spectra of the para- H_2^{18}O line at 1102 GHz and the ortho- H_2^{18}O line at 1656 GHz are shown in Figure 2. The derived OPR in G34.26 is 1.9. The total (ortho+para) H_2^{18}O abundance in the envelope X_{out} is 4.9×10^{-11} . The recommended isotopic abundance ratio between ^{16}O and ^{18}O is 500 (Lodders 2003). Using this value, the H_2O outer abundance is 2.5×10^{-8} and the outer HDO/ H_2O ratio is 3.1×10^{-3} in the envelope. Considering the results with a 20% calibration uncertainty, the outer abundance ratio is $(2.5\text{--}3.7) \times 10^{-3}$.

W51e1/e2: Observed spectra and Gaussian fit of the 465 GHz and 509 GHz HDO transitions toward W51e1/e2, along with the best-fit model, are shown in Figure 4 by black, blue, and red lines, respectively. Model results for W51 are presented in Table 6. We obtain the best fit for: $T_0 = 230$ K, $n_0 = 1.8 \times 10^8 \text{ cm}^{-3}$, $X_{\text{in}} = 1.7 \times 10^{-8}$, and $X_{\text{out}} = 7.0 \times 10^{-11}$. The resulting uncertainties of X_{in} and X_{out} are shown in Figure 5 and listed in Table 8.

Model flux densities per beam at 509 GHz and 893 GHz for W51 are also listed in Table 6.

Observed and modeled spectra of the para- H_2^{18}O line at 1102 GHz and the ortho- H_2^{18}O line at 1656 GHz are shown in

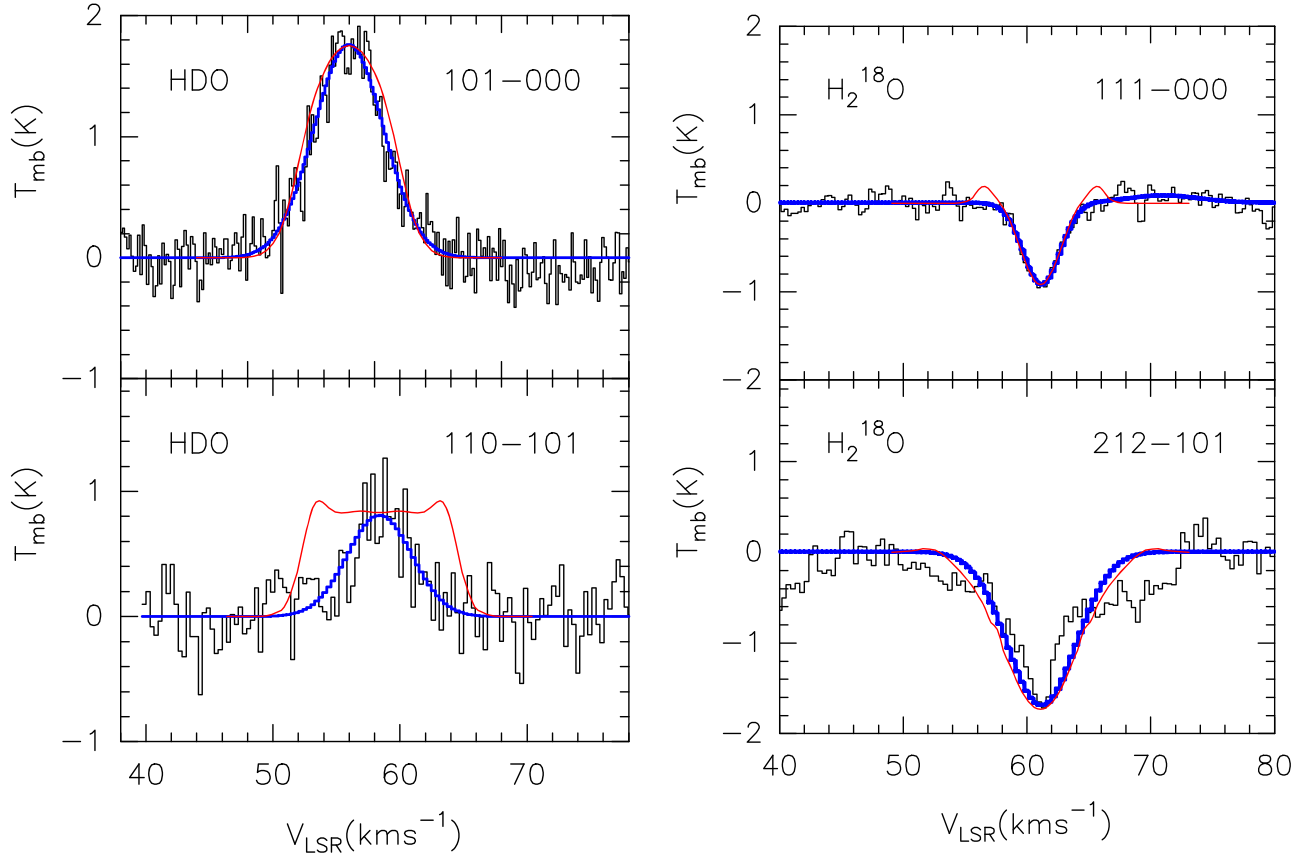


Figure 2. Observed spectra of the 465 and 509 GHz HDO lines and 1102 and 1656 GHz H_2^{18}O lines toward G34.26+0.15. The Gaussian fits are shown in blue, the best-fit model in red.

Table 5

Line Intensities and Continuum Fluxes for the Best-fit Model of G34.26+0.15

HDO Transitions	Freq (GHz)	T_{obs} (K)	T_{mod} (K)	FOM ₁
$1_{0,1}-0_{0,0}$	464.925 ^a	1.8	1.8	0.00
$1_{1,0}-1_{0,1}$	509.292 ^a	0.8	0.8	0.00
$2_{1,1}-2_{1,2}$	241.562 ^b	1.8	1.6	0.01
$3_{1,2}-2_{2,1}$	225.897 ^b	1.2	1.4	0.03
$4_{2,2}-4_{2,3}$	143.727 ^b	0.4	0.5	0.06
$5_{2,3}-4_{3,2}$	255.050 ^b	0.6	0.4	0.11
Flux (Jy/beam)	F_{353} ^c	$F_{353\text{mod}}$		FOM ₂
	56.1	56.4		0.00
	F_{509} ^d	$F_{509\text{mod}}$		
	310	376		0.05
	F_{893} ^d	$F_{893\text{mod}}$		
	1320	1525		0.02
FOM = 0.28				

Notes.

^a This work.

^b Jacq & Wamsley (1990).

^c CSO.

^d *Herschel*.

Figure 4. The total H_2^{18}O abundance (OPR = 2.9) in the envelope X_{out} is 5.5×10^{-11} . The H_2O outer abundance is 2.8×10^{-8} and outer HDO/ H_2O ratio is 2.5×10^{-3} .

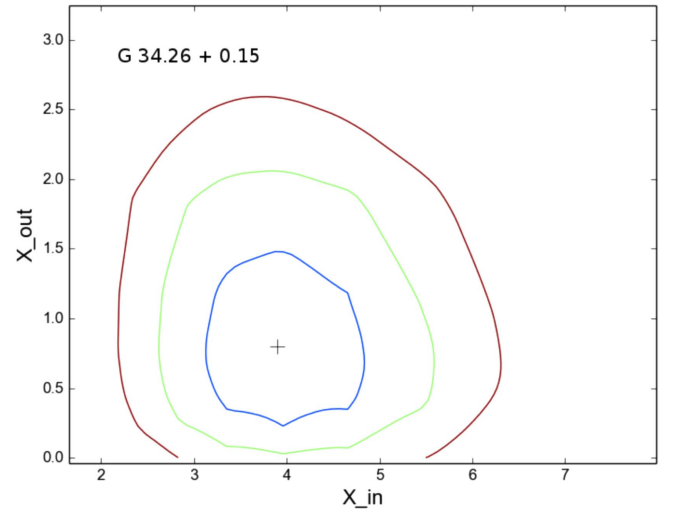


Figure 3. X_{in} and X_{out} HDO abundance contours at 1σ , 2σ , 3σ for χ^2 . The best-fit model is represented by the symbol “+” ($X_{\text{in}} = a \times 10^{-8}$, $X_{\text{out}} = b \times 10^{-10}$).

Considering the results with a 20% calibration uncertainty, the outer ratio is $(2.0-3.0) \times 10^{-3}$.

W49N: Observed spectra and Gaussian fit of the 465 GHz and 509 GHz HDO transitions toward W49N, along with the best-fit model are shown in Figure 6 by black, blue, and red lines, respectively. Model results for W49N are presented in Table 7. We obtain the best fit for: $T_0 = 300$ K, $n_0 = 2.5 \times 10^8 \text{ cm}^{-3}$, $X_{\text{in}} = 0.3 \times 10^{-8}$, and $X_{\text{out}} = 10 \times 10^{-11}$. The resulting

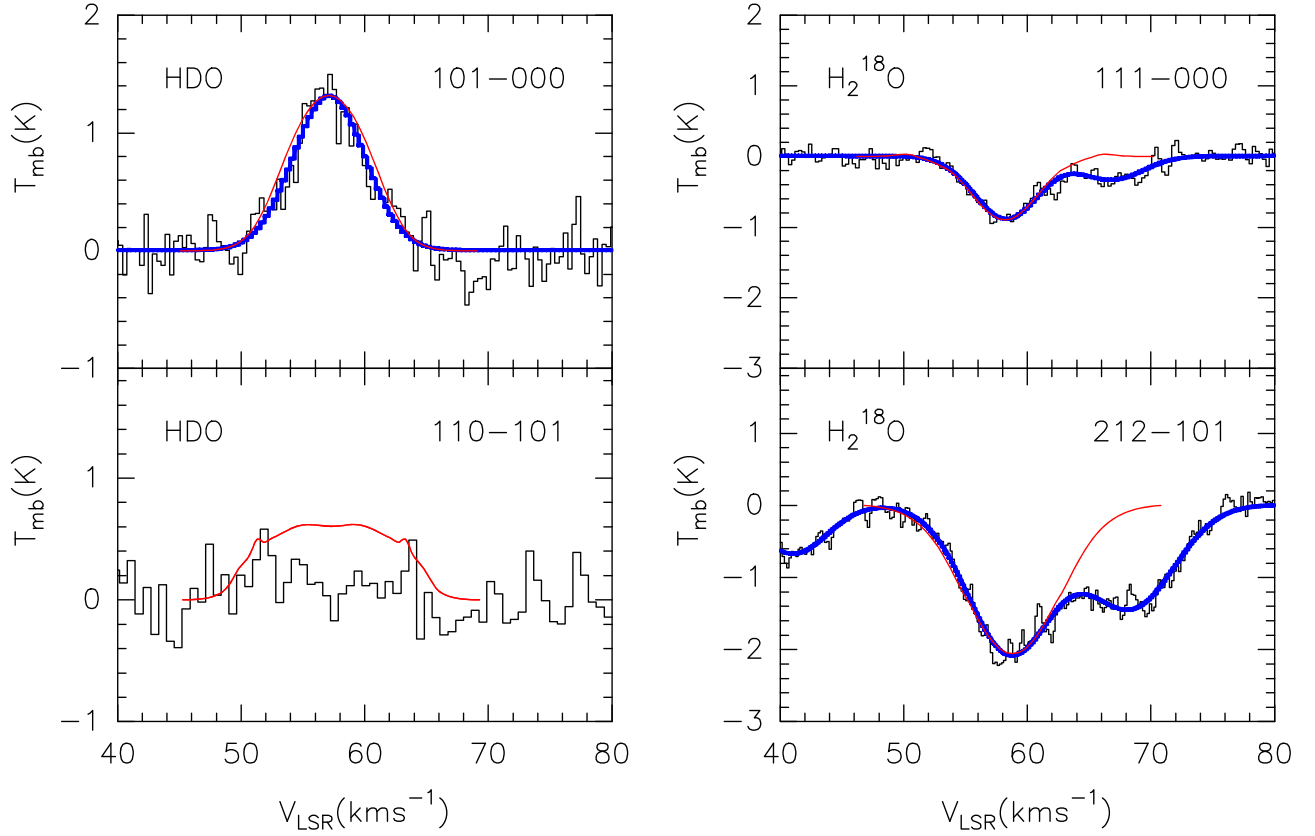


Figure 4. Observed spectra of the 465 and 509 GHz HDO lines and 1102 and 1656 GHz H_2^{18}O lines toward W51e₁/e₂. The Gaussian fits are shown in blue, the best-fit model in red.

Table 6

Line Intensities and Continuum Fluxes for the Best-fit Model of W51e₁/e₂

HDO Transitions	Freq (GHz)	T_{obs} (K)	T_{mod} (K)	FOM ₁
$1_{0,1}-0_{0,0}$	464.925 ^a	1.3	1.3	0.00
$2_{1,0}-1_{0,1}$	509.292 ^a	<0.9	0.6	
$2_{1,1}-2_{1,2}$	241.562 ^b	0.8	0.8	0.00
$3_{1,2}-2_{2,1}$	225.897 ^b	0.6	0.67	0.01
$5_{2,3}-4_{3,2}$	255.050 ^b	0.3	0.2	0.11
Flux (Jy/beam)	F_{509}^c	$F_{509\text{mod}}$		FOM ₂
	400	350		0.02
	F_{893}^c	$F_{893\text{mod}}$		
	1490	1509		0.00
				FOM = 0.14

Notes.

^a This work.

^b Jacq & Wamsley (1990).

^c *Herschel*.

uncertainties of X_{in} and X_{out} are shown in Figure 7 and listed in Table 8. As data on the high excitation lines are missing for W49N, the inner abundance X_{in} is not as well-constrained as in the other sources.

Observed and modeled spectra of the para- H_2^{18}O line at 1102 GHz and the ortho- H_2^{18}O line at 1656 GHz are shown in Figure 6. The total H_2^{18}O (OPR = 3.1) abundance in the envelope X_{out} is 1.1×10^{-10} . The H_2O outer abundance is 5.5×10^{-8} and the outer HDO/ H_2O ratio is 1.8×10^{-3} .

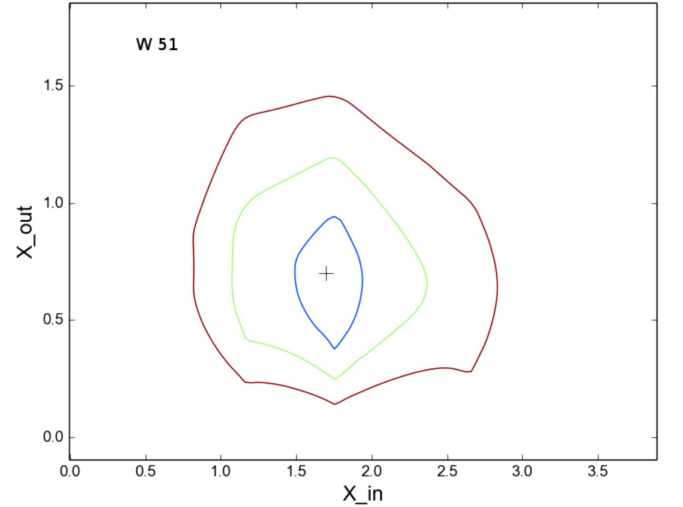


Figure 5. X_{in} and X_{out} HDO abundance contours at 1σ , 2σ , 3σ for χ^2 . The best-fit model is represented by the symbol “+” ($X_{\text{in}} = a \times 10^{-8}$, $X_{\text{out}} = b \times 10^{-10}$).

Considering the results with a 20% calibration uncertainty, the outer abundance ratio is $(1.4-2.2) \times 10^{-3}$.

4. Discussion

4.1. Comparison with Previous Studies

Previous observations of the high-mass star-forming regions indicate an HDO abundance in the hot cores ($T > 100$ K) but not in the outer, cooler envelopes ($T < 100$ K) (Jacq &

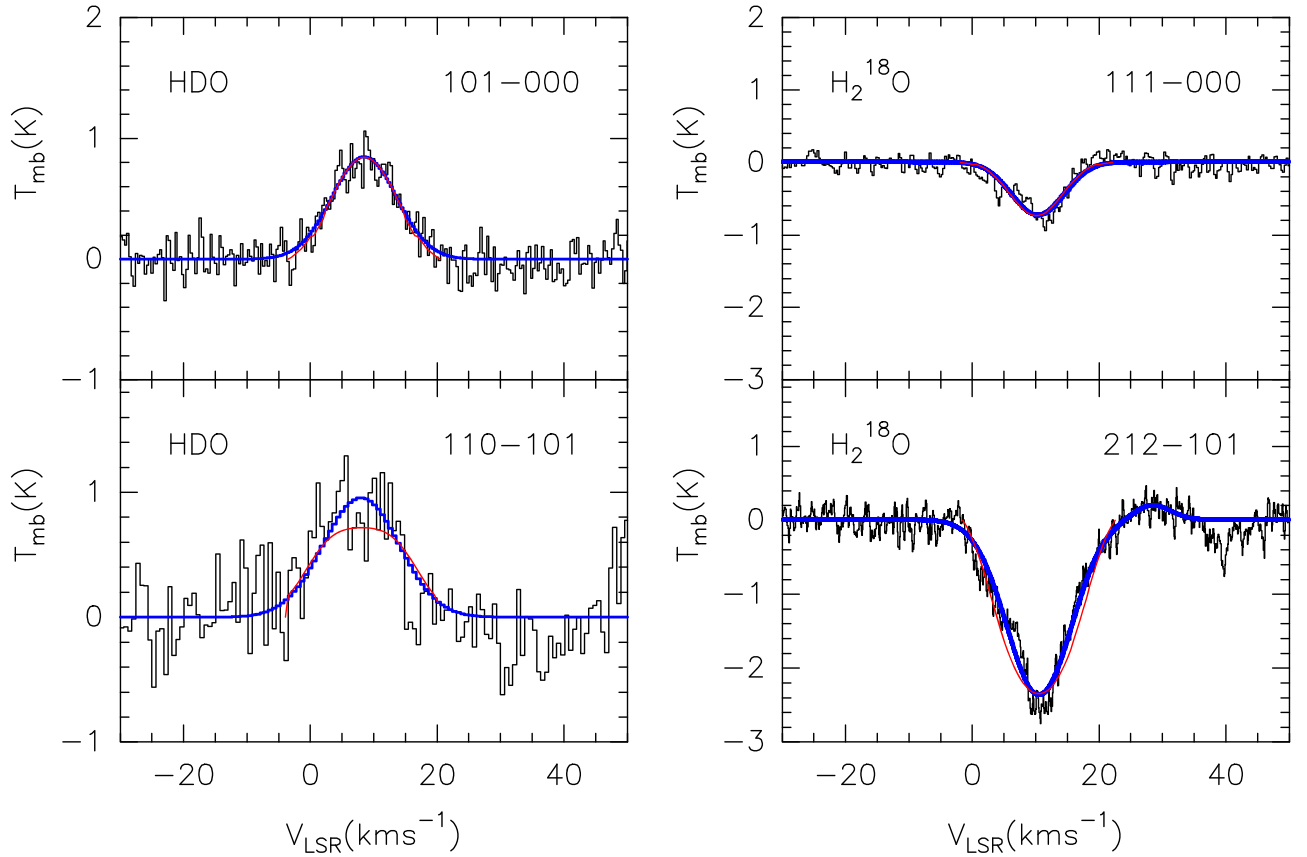


Figure 6. Observed spectra of the 465 and 509 GHz HDO lines and 1102 and 1656 GHz H_2^{18}O lines toward W49N. The Gaussian fits are shown in blue, the best-fit model in red.

Table 7

Line Intensities and Continuum Fluxes for the Best-fit Model of W49N

HDO Transitions	Freq (GHz)	T_{obs} (K)	T_{mod} (K)	FOM ₁
$1_{0,1}-0_{0,0}$	464.925 ^a	0.8	0.8	0.00
$2_{1,0}-1_{0,1}$	509.292 ^a	0.7	0.6	0.02
Flux (Jy/beam)	F_{509}^b	$F_{509\text{mod}}$		FOM ₂
	320	310		0.00
	F_{893}^b	$F_{893\text{mod}}$		0.01
	1450	1410		FOM = 0.03

Notes.

^a This work.

^b *Herschel*.

Wamsley 1990; Gensheimer et al. 1996, Pardo et al. 2001; see Table 9). We could find variations in the derived HDO abundances in the hot cores between 1.5×10^{-9} and 2.0×10^{-7} . Jacq & Wamsley (1990) believed that, independent of all modeling, a value much lower than 3.0×10^{-8} for HDO/ H_2 in the hot core is very unlikely. For the first time, Comito et al. (2003, 2010) estimated the HDO abundance in both the inner and outer regions of the high-mass source Sgr B2(M). These are, respectively: 3.5×10^{-9} ($T > 200$ K), 1.5×10^{-9} ($100 \text{ K} < T < 200 \text{ K}$), and 2.5×10^{-11} ($T < 100$ K). The singly deuterated form of water has been also observed in the massive source AFGL 2591, with abundance varying

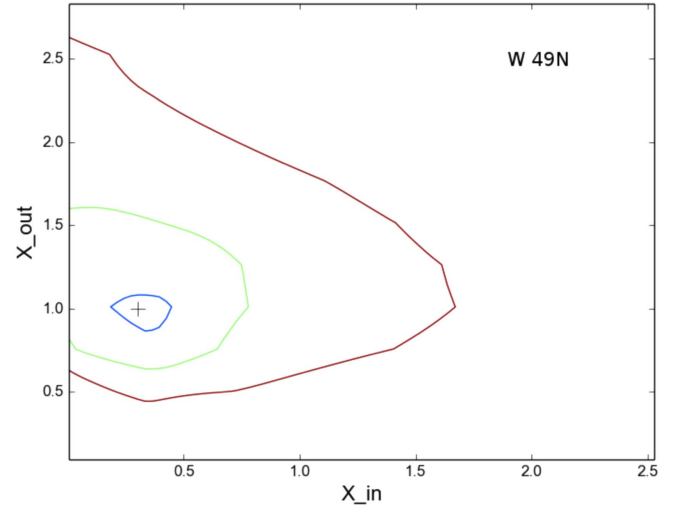


Figure 7. X_{in} and X_{out} HDO abundance contours at 1σ , 2σ , and 3σ for χ^2 . The best-fit model is represented by the symbol “+” ($X_{\text{in}} = a \times 10^{-8}$, $X_{\text{out}} = b \times 10^{-10}$).

from 1×10^{-7} in the hot core and 4×10^{-9} in the outer envelope (van der Tak et al. 2006). Liu et al. (2013) and Coutens et al. (2014) determined the HDO abundance and HDO/ H_2O ratio in the inner and outer region of G34.26 (see Table 9). We derived the HDO abundances of X_{in} and X_{out} in three high-mass star-forming regions: G34.26, W49N, and W51. We found a difference between our $X_{\text{in}}(\text{HDO})$ and $X_{\text{out}}(\text{HDO})$ values for G34.26 and those reported by Coutens et al. (2014) and Liu et al. (2013), respectively. This is likely

Table 8
Best-fit Model Parameters

Source	n_0 (cm $^{-3}$)	T_0 (K)	$X_{\text{in}}(\text{HDO})$	Range (2σ)	$X_{\text{out}}(\text{HDO})$	Range (2σ)
G34.26+0.15	1.0×10^8	200	3.7×10^{-8}	$2.7\text{--}5.6 \times 10^{-8}$	7.8×10^{-11}	$0.2\text{--}2.1 \times 10^{-10}$
W51e $_1$ /e $_2$	1.8×10^8	230	1.7×10^{-8}	$1.1\text{--}2.4 \times 10^{-8}$	7.0×10^{-11}	$0.3\text{--}1.1 \times 10^{-10}$
W49N	2.5×10^8	300	0.3×10^{-8}	$0.2\text{--}0.5 \times 10^{-8\text{a}}$	1.0×10^{-10}	$0.8\text{--}1.6 \times 10^{-10}$

Note.

^a Range (1σ).

Table 9
Comparison of HDO Abundance between Different Sources

Source	$X_{\text{in}}(\text{HDO})$ (Best Fit)	$X_{\text{out}}(\text{HDO})$ (Best Fit)	$(\text{HDO}/\text{H}_2\text{O})_{\text{in}}$	$(\text{HDO}/\text{H}_2\text{O})_{\text{out}}$	References
Low-mass protostars					
L1448-mm	$\sim 4.0 \times 10^{-7}$	$\leq 3.0 \times 10^{-9}$	1
IRAS 16293-2422	1.0×10^{-7}	1.5×10^{-10}	3×10^{-2}	$\leq 2 \times 10^{-3}$	2
	1.7×10^{-7}	8.0×10^{-11}	3.4×10^{-2}	5.0×10^{-3}	3
	$(9.2 \pm 2.6) \times 10^{-4}$...	4
NGC 1333-IRAS2A	8.0×10^{-8}	7.0×10^{-10}	$\geq 1.0 \times 10^{-2}$	$\sim 7 \times 10^{-2}$	5
	$(3.0\text{--}80) \times 10^{-3}$...	6
	1.0×10^{-3}	...	7
	$(7.4 \pm 2.1) \times 10^{-4}$...	8
NGC 1333-IRAS4B	$\leq 6.0 \times 10^{-4}$...	9
	1.0×10^{-8}	1.2×10^{-10}	$(1.0\text{--}37) \times 10^{-4}$...	10
	$(5.9 \pm 1.7) \times 10^{-4}$...	8
NGC 1333-IRAS 4A-NW	$(19.1 \pm 5.4) \times 10^{-4}$...	8
	7.5×10^{-9}	1.2×10^{-11}	$(4.0\text{--}30) \times 10^{-4}$...	10
	$(5.0\text{--}30) \times 10^{-3}$...	6
Intermediate-mass protostar					
NGC 7192 FIRS2	4.0×10^{-8}	11
High-mass hot cores ^a					
G34.26+0.15	3.7×10^{-8}	7.8×10^{-11}	3.7×10^{-4}	3.1×10^{-3}	12
	6.0×10^{-8}	5.0×10^{-12}	3.0×10^{-4}	$(1.9\text{--}4.9) \times 10^{-4}$	13
	2.0×10^{-7}	8.0×10^{-11}	$(3.5\text{--}7.5) \times 10^{-4}$	$(1.0\text{--}2.2) \times 10^{-3}$	14
	4.6×10^{-9}	...	1.1×10^{-4}	...	15
	$\sim 2.7 \times 10^{-8}$...	4.0×10^{-4}	...	16
W51e $_1$ /e $_2$	1.7×10^{-8}	7.0×10^{-11}	1.7×10^{-4}	2.8×10^{-3}	12
W49N	3.0×10^{-9}	1.0×10^{-10}	3.0×10^{-5}	1.8×10^{-3}	12
	1.5×10^{-9}	...	6.3×10^{-5}	...	15
	$\sim 2.2 \times 10^{-8}$...	3.0×10^{-4}	...	16
W 33A	2.0×10^{-7}	1.0×10^{-8}	17
NGC 6334 I	1.3×10^{-10}	...	2.1×10^{-4}	...	18
W3(OH)/(H $_2$ O)	$(2.0\text{--}6.0) \times 10^{-4}$...	19
AFGL 2591	1.0×10^{-7}	2.0×10^{-8}	17
NGC 7538 IRS1	1.0×10^{-7}	4.0×10^{-9}	5.0×10^{-4}	$(4.0\text{--}400.0) \times 10^{-3}$	17
Sgr B2(M)	1.5×10^{-9}	1.3×10^{-11}	20
	2.0×10^{-9}	...	1.8×10^{-4}	...	15
Orion KL	$\sim 4.5 \times 10^{-8}$...	3.0×10^{-3}	...	21
Earth's oceans HDO/H $_2$ O:	3.0×10^{-4}	22			

Note.

^a The fractional abundances of water in the hot core: $X_{\text{in}}(\text{H}_2\text{O}) \sim 1.0 \times 10^{-4}$ (e.g., Snell et al. 2000; Boonman et al. 2003; Herpin et al. 2012, Emprechtinger et al. 2013) are taken in the inner HDO/H $_2$ O ratio estimation.

References. (1) Codella et al. (2010), (2) Parise et al. (2005), (3) Coutens et al. (2012), (4) Persson et al. (2014) on scale ≤ 300 au, (5) Liu et al. (2011), (6) Taquet et al. (2013), (7) Visser et al. (2013), (8) Persson et al. (2014), on scale ≤ 300 au; (9) Jørgensen et al. (2010), on scale ≤ 50 au; (10) Coutens et al. (2013), (11) Fuente et al. (2012), (12) This work; (13) Liu et al. (2013), (14) Coutens et al. (2014), (15) Gensheimer et al. (1996), (16) Jacq & Wamsley (1990), (17) van der Tak et al. (2006), (18) Emprechtinger et al. (2013), (19) Helmich et al. (1996), (20) Comito et al. (2010), (21) Neill et al. (2013), (22) Lecuyer et al. (1998).

because the first authors used different model structures and a higher jump temperature, and the second authors did not check the higher value of $X_{\text{out}}(\text{HDO})$ in their model. The obtained

HDO abundances of our target sources in the hot cores and the cooler envelopes are relatively consistent with the values found in the other high-mass star-forming regions (Kulczak-

Jastrzębska 2016). These results show that the HDO abundance is enriched in the inner regions of high-mass protostars because of the sublimation of the ice mantles, in the same way as for other studies low- and high-mass sources (e.g., NGC 1333 IRAS2A, IRAS 162923-2422, AFGL 2591, G34.26; Table 9). Observations of sites of high-mass star formation show in general the lower HDO abundances than observations of low-mass star-forming cores. Possibly for high-mass protostars, the very cold and dense pre-collapse phase where CO freeze-out onto the grain mantles lasts only a short time, and the chemical reactions leading to the enhancement of deuterium abundance are strongly depressed when the temperature increases (Caselli et al. 2008).

4.2. Variation of the HDO/H₂O Ratios with the Radius

Based on observations of two H₂¹⁸O fundamental transitions, we found that the H₂O abundances in our target sources are $(2.5\text{--}5.5) \times 10^{-8}$. Similar values were found for the other high-mass protostars: $5 \times 10^{-10} - 4 \times 10^{-8}$ (Marseille et al. 2010; van der Tak et al. 2010; Herpin et al. 2012; Choi et al. 2015). The H₂O abundance in the cold envelope agrees fairly well with the model predictions for cold regions where freeze-out takes place (Ceccarelli et al. 1996; van der Tak et al. 2013).

The water–deuterium fractionation in the inner and outer envelope of the high-mass star-forming region G34.26 was previously estimated by Liu et al. (2013) and Coutens et al. (2014). We determined the outer HDO/H₂O ratio in G34.26 to be 3.1×10^{-3} , this value is relatively consistent with Coutens et al. (2014) (see Table 9). To estimate the inner HDO/H₂O ratio for the target sources, we used an inner H₂O abundance value as high as 10^{-4} from observations of other high-mass star-forming-regions (Snell et al. 2000; Boonman et al. 2003; Chavarría et al. 2010; Herpin et al. 2012; van der Tak et al. 2013). However, a lower value of $\sim 10^{-6}$ was found in NGC 6334 I (Emprechtinger et al. 2013). A possible explanation for the low water abundance in this source is a time-dependent effect; water molecules may not have had enough time to fully desorb from the dust grain. Our derived HDO/H₂O ratios are consequently not well-constrained. We estimated that the inner HDO/H₂O ratio is about $(1\text{--}4) \times 10^{-4}$ within the range found in other high-mass star-forming regions (Jacq & Wamsley 1990; Gensheimer et al. 1996; Emprechtinger et al. 2013; Liu et al. 2013).

The HDO/H₂O ratio varies between the inner and outer regions of high-mass protostars. The water deuterium fractionation decreases from the cold outer regions to the warm inner regions. The same trend is also present in low-mass protostars (Coutens et al. 2013, 2014). The difference could be explained by the gradient of deuteration within interstellar ices. Only the external ice layers evaporate in the cold envelope through non-thermal processes, whereas the inner part of ice mantles evaporates only in the hot core (Taquet et al. 2014). The HDO/H₂O ratio in the bulk of ice mantle preserves the past physical and chemical conditions that materials experienced, whereas the HDO/H₂O ratio in active surface layers reflects local physical and chemical conditions (Furuya et al. 2016). The enrichment of deuterium in ice should mostly occur in the latter prestellar core and/or protostellar phases, where interstellar UV radiation is heavily attenuated and CO is frozen out. Another possibility for the decrease of water deuterium fractionation toward the inner regions would be the additional water vapor formation at

high temperatures ($T > 200\text{--}300$ K) thorough reactions: $\text{O} + \text{H}_2 \rightarrow \text{OH} + \text{H}$ and $\text{OH} + \text{H}_2 \rightarrow \text{H}_2\text{O} + \text{H}$, which would decrease the HDO/H₂O ratios. However, it requires that a large amount of oxygen is in atomic form, rather than in molecules, in the high-density inner regions.

5. Summary

Using CSO observations of HDO low-excitation transitions, as well as previous observations of HDO high excitations and H₂¹⁸O low-excitation transitions from the literature, we determined the inner and outer HDO abundances, as well as the HDO/H₂O outer ratios toward three high-mass star-forming regions: G34.26+0.15, W51e1/e2, W49N. We derived HDO abundances of $X_{\text{in}} = (0.3\text{--}3.7) \times 10^{-8}$ (for $T \geq 100$ K) and $X_{\text{out}} = (7.0\text{--}10.0) \times 10^{-11}$ (for $T < 100$ K), (see Table 8), and HDO/H₂O outer ratios of $(1.8\text{--}3.1) \times 10^{-3}$ (see Table 9). With this study, we showed that the 509 GHz transition can provide good constraints on the HDO abundance in the transition region between the hot core and colder envelope, and that the 465 GHz HDO transition is a very good probe of the outer envelope of massive protostars. These transitions could help for more advanced modeling of water in high-mass sources. The HDO/H₂O ratios were also found to be higher in the cold outer envelopes than in the hot cores, as already determined for two high-mass sources. What is important is that the model is very simple, easy to implement, not GPU-intensive, and provides a starting point for more sophisticated analysis.

The author thanks the referee very much for the highly constructive comments and suggestions. The author is grateful to N. Flagey for providing the reduced HIFI data of H₂¹⁸O. M. K. would like to thank Maryvonne Gerin and Darek Lis for fruitful discussions and a careful reading of the manuscript. I acknowledge support from the grant 2016/21/B/ST9/01626 from the National Science Centre, Poland. This research is based on observations from the Caltech Submillimeter Observatory, which is operated by the California Institute of Technology under cooperative agreement with the National Science Foundation (AST-0838261).

References

- Avalos, M., Lizano, S., Franco-Hernandez, R., et al. 2009, *ApJ*, **690**, 1084
- Baulch, D. L., Cobos, C. J., & Cox, R. A. 1992, *JPCRD*, **21**, 441
- Bergin, E. A., Phillips, T. G., Comito, C., et al. 2010, *A&A*, **521**, 20
- Beuther, H., Schilke, P., & Menten, K. M. 2001, *ApJ*, **566**, 945
- Boonman, A. M. S., Doty, S., & van Dishoeck, E. F. 2003, *A&A*, **406**, 937
- Brown, P. D., & Millar, T. J. 1989, *MNRAS*, **237**, 661
- Campbell, M. F., Garland, C. A., & Deutsh, L. K. 2000, *ApJ*, **536**, 816
- Caselli, P., Vastel, C., Ceccarelli, C., et al. 2008, *A&A*, **492**, 703
- Cazaux, S., Caselli, P., & Spaans, M. 2011, *ApJ*, **741**, 34
- Ceccarelli, C., Hollenbach, D. J., & Tielens, A. G. G. M. 1996, *ApJ*, **471**, 400
- Chavarría, L., Herpin, F., Jacq, T., et al. 2010, *A&A*, **521**, 37
- Choi, Y., van der Tak, F. F. S., van Dishoeck, E. F., et al. 2015, *A&A*, **576**, 85
- Codella, C., Ceccarelli, C., Nisini, B., et al. 2010, *A&A*, **522**, L1
- Comito, C., Schilke, P., Gerin, M., et al. 2003, *A&A*, **402**, 635
- Comito, C., Schilke, P., Rolfs, R., et al. 2010, *A&A*, **521**, L38
- Coutens, A., Vastel, C., & Cabrit, S. 2013, *A&A*, **560**, 39
- Coutens, A., Vastel, C., Caux, E., et al. 2012, *A&A*, **539**, 132
- Coutens, A., Vastel, C., Hincelin, U., et al. 2014, *MNRAS*, **445**, 1299
- Daniel, F., Dubernet, M.-L., & Grosjean, A. 2011, *A&A*, **536**, A76
- De Pree, C. G., Wilner, D. J., & Goss, W. M. 2000, *ApJ*, **540**, 308
- Dislaire, V., Hily-Blant, P., Faure, A., et al. 2012, *A&A*, **537**, A20
- Draine, B. T. 2013, *ARA&A*, **41**, 241
- Emprechtinger, M., Lis, D. C., Rolfs, R., et al. 2013, *ApJ*, **761**, 61

- Faure, A., Wiesenfeld, L., Scribano, Y., et al. 2012, *MNRAS*, **420**, 699
- Fish, V. L., Reid, M. J., Wilner, D. J., et al. 2003, *ApJ*, **587**, 701
- Flagey, N., Goldsmith, P. F., Lis, D. C., et al. 2013, *ApJ*, **762**, 11
- Flower, D. R., Pineau Des Forets, D. R. G., & Walmsley, C. M. 2006, *A&A*, **456**, 215
- Fontani, F., Palau, A., & Caselli, P. 2011, *A&A*, **529**, L7
- Fraser, H. J., Bisshop, S. E., Pontoppidan, K. M., et al. 2005, *MNRAS*, **356**, 1283
- Fraser, H. J., Collins, M. P., McCoustra, M. R., et al. 2001, *MNRAS*, **327**, 1165
- Fuente, A., Caselli, P., & Coey, C. M. 2012, *A&A*, **540**, 75
- Furuya, K., van Dishoeck, E. F., & Aikawa, Y. 2016, *A&A*, **586**, 127
- Garay, G., & Rodriguez, L. F. 1990, *ApJ*, **362**, 191
- Gensheimer, P. D., Mauersberger, R., & Wilson, T. L. 1996, *A&A*, **314**, 281
- Genzel, R., Downes, D., Schneps, M. H., et al. 1981, *ApJ*, **247**, 1039
- Goldsmith, P. F., Bergin, E. A., & Lis, D. C. 1997, *ApJ*, **491**, 615
- Gordon, K. D., Galliano, F., Hony, S., et al. 2010, *A&A*, **518**, L89
- Gordon, M. A., & Jewell, P. R. 1987, *ApJ*, **323**, 766
- Gwinn, C. R., Moran, J. M., & Reid, M. J. 1992, *ApJ*, **393**, 149
- Hajigholi, M., Persson, C. M., Wirstrom, E. S., et al. 2016, *A&A*, **585**, 158
- Hatchell, J., & van der Tak, F. F. S. 2003, *A&A*, **409**, 589
- Helmich, F. P., van Dishoeck, E. F., & Jansen, D. J. 1996, *A&A*, **313**, 657
- Herpin, F., Chavarría, L., van der Tak, F., et al. 2012, *A&A*, **542**, 76
- Hildebrand, R. H. 1983, *QJRAS*, **24**, 267
- Hill, M. A., Thompson, M. G., & Burton, A. J. 2006, *MNRAS*, **368**, 1223
- Hunter, T. R., Neugebauer, G., & Benford, D. J. 1998, *ApJL*, **493**, L97
- Jacq, T., & Wamsley, C. M. 1990, *A&A*, **228**, 447
- Jørgensen, J. K., & van Dishoeck, E. F. 2010, *ApJL*, **710**, L72
- Keto, E. R., Ho, P. T. P., & Reid, M. J. 1987, *ApJL*, **323**, L117
- Kuchar, T. A., & Bania, T. M. 1994, *ApJ*, **436**, 117
- Kulczak-Jastrzębska, M. 2016, *AcA*, **66**, 239
- Lampton, M., Margon, B., & Bowyer, S. 1976, *ApJ*, **208**, 177
- Lecuyer, C., Gillet, P., & Robert, F. 1998, *ChGeo*, **145**, 229
- Le Gal, R., Hily-Blant, P., Faure, A., et al. 2014, *A&A*, **562**, 83
- Li, A., & Greenberg, J. M. 2003, in *Solid State Astrochemistry*, ed. V. Pirronello, J. Krelowski, & G. Manico (Dordrecht: Kluwer), **37**
- Lis, D. C. 2000, in *ASP Conf. Ser. 217, Imaging at Radio through Submillimeter Wavelengths*, ed. J. G. Magnum & S. E. Radford (San Francisco, CA: ASP), **100**
- Liu, F. C., Parise, B., Kristensen, L., et al. 2011, *A&A*, **527**, A19
- Liu, F. C., Parise, B., Wyrowski, F., et al. 2013, *A&A*, **550**, A37
- Lodders, K. 2003, *ApJ*, **591**, 1220L
- Macdonald, G. M., Gibb, A. G., & Habing, R. J. 1996, *A&AS*, **119**, 333
- Marseille, M. G., van der Tak, F. F. S., & Herpin, F. 2010, *A&A*, **522**, 40
- Minier, V., Burton, M. G., Hill, T., et al. 2005, *A&A*, **429**, 945
- Mumma, M. J., Weaver, H. A., & Larson, H. P. 1987, *A&A*, **187**, 419
- Neill, J. L., Wang, S., Bergin, E. A., et al. 2013, *ApJ*, **770**, 142
- Pagani, L., Vastel, C., Hugo, E., et al. 2009, *A&A*, **494**, 623
- Parise, B., Caux, E., Castets, A., et al. 2004, *A&A*, **431**, 547
- Pardo, J. R., Cernicharo, J., Herpin, F., et al. 2001, *ApJ*, **562**, 799
- Persson, M. V., Jørgensen, J. K., & van Dishoeck, E. F. 2013, *A&A*, **549**, L3
- Persson, M. V., Jørgensen, J. K., van Dishoeck, E. F., et al. 2014, *A&A*, **563**, 74
- Petuchowsky, S. J., & Bennett, C. L. 1988, *ApJ*, **326**, 376
- Pety, J. 2005, in *SF2A Semaine de l'Astrophysique Française*, ed. F. Casoli, T. Contini, J. M. Hameury, & L. Pagani (Strasbourg: EdP-Sciences), **721**
- Pickett, H. M., Poytner, R. L., Cohen, E. A., et al. 1998, *JQSRT*, **60**, 883
- Planck Collaboration XIV 2014, *A&A*, **564**, 45
- Reid, M. J., & Ho, P. T. P. 1985, *ApJL*, **288**, L17
- Roberts, H., Herbst, E., & Millar, T. J. 2003, *ApJL*, **591**, L41
- Roberts, H., & Millar, T. J. 2000, *A&A*, **361**, 780
- Roelfsema, P. R., Helmich, F. P., Yeyssier, D., et al. 2012, *A&A*, **537**, A17
- Rolffs, R., Schilke, P., Comito, C., et al. 2010, *A&A*, **521**, L46
- Rybicki, G. B., & Hummer, D. G. 1991, *A&A*, **245**, 171
- Sato, M., Reid, M. J., Brunthaler, A., et al. 2010, *ApJ*, **720**, 1055
- Schröier, F. L., van der Tak, F. F. S., & van Dishoeck, E. F. 2005, *A&A*, **432**, 369
- Schulz, A., Gusten, R., Walmsey, C. M., et al. 1991, *A&A*, **246**, 55
- Shu, F. H. 1977, *ApJ*, **214**, 488
- Sievers, A. W., Mezger, P. G., & Bordeon, M. A. 1991, *A&A*, **251**, 231
- Snell, R. L., Howe, J. E., Ashby, M. L. N., et al. 2000, *ApJL*, **539**, L97
- Stier, M. T., Jaffe, D. T., & Rengarajan, C. W. 1984, *ApJ*, **283**, 573
- Taquet, V., Charnley, S. B., & Sipilä, O. 2014, *ApJ*, **791**, 1
- Taquet, V., López-Sepulcre, A., Ceccarelli, C., et al. 2013, *A&A*, **550**, 127
- Thompson, M. A., Hatchell, J., Walsh, A. J., et al. 2006, *A&A*, **453**, 1003
- Tielens, A. G. G. M. 1983, *A&A*, **119**, 177
- van der Tak, F. F. S. 2011, in *Proc. IAU Symp. 280, The Molecular Universe* (Cambridge: Cambridge Univ. Press), **449**
- van der Tak, F. F. S., Black, J. H., Schröier, F. L., et al. 2007, *A&A*, **468**, 627
- van der Tak, F. F. S., Chavarría, L., Herpin, F., et al. 2013, *A&A*, **554**, 83
- van der Tak, F. F. S., Marseille, M. G., Herpin, F., et al. 2010, *A&A*, **518**, 107
- van der Tak, F. F. S., van Dishoeck, E. F., Evans, N. J., et al. 2000, *ApJ*, **537**, 283
- van der Tak, F. F. S., Walmsley, C. M., Herpin, F., et al. 2006, *A&A*, **447**, 1011
- van Dishoeck, E. F., Bergin, E. A., Lis, D. C., et al. 2014, in *Protostars and Planets VI*, ed. D. C. Beuther et al. (Tucson, AZ: Univ. Arizona Press), **835**
- van Dishoeck, E. F., Herbst, E., & Neufeld, D. A. 2013, *ChRv*, **113**, 9043
- Visser, R., Jørgensen, J. K., Kristensen, L. E., et al. 2013, *ApJ*, **769**, 19
- Viti, S., & Williams, D. A. 1999, *MNRAS*, **305**, 755
- Ward-Thompson, D., & Robson, E. I. 1990, *MNRAS*, **244**, 458
- Watanabe, N., Nagaoka, A., & Kouchi, A. 2010, *ApJL*, **714**, L233
- Watt, S., & Mundy, L. G. 1999, *ApJS*, **125**, 143
- Wiesenfeld, L., Scribano, Y., & Faure, A. 2011, *PCCP*, **13**, 8230
- Wright, M., Goeran, S., Wilner, D. J., et al. 1992, *ApJ*, **393**, 225
- Zapata, L. A., Schmid-Burgk, J., & Menten, K. M. 2011, *A&A*, **529**, 24
- Zhang, Q., & Ho, P. T. P. 1997, *ApJ*, **488**, 241
- Zmuidzinas, J., Blake, A., & Carlstrom, J. 1995, *ApJL*, **447**, L125

Appendix C

Deuterated Molecules in Star-Forming Regions

Deuterated Molecules in Star-Forming Regions

M. Kulczak-Jastrzębska

Astronomical Observatory of the Jagiellonian University, 30-244 Orla 171, Kraków,
Poland

e-mail:kulczak@oa.uj.edu.pl

Received March 1, 2018

ABSTRACT

Imaging the spatial distribution of deuterated molecules in several nearby low-mass star forming regions, as traced by the DCO^+ (3–2) emission, suggest that the deuterated material is often displaced with respect to the highest column density regions, as traced by submillimeter dust continuum emission and sometimes appears to be associated with the high-velocity CO (2–1) emission, tracing outflow activity. High deuteration levels in isolated prestellar cores can be explained by gas-phase or grain-surface chemistry in dense, cold regions, where abundant gas-phase species are frozen onto dust grains – a process that is now relatively well understood. We argue that an alternative mechanism may operate in dense gas in the vicinity of embedded young stellar objects, where slow C-type shocks associated with molecular outflows may produce conditions favorable for deuterium fractionation either by increasing the gas volume density in the post-shock gas and thus shortening the depletion and gas-phase reaction time-scales, or by evaporating grain mantle ices.

Key words: *astrochemistry – abundances – individual (B1, LDN 1641, LDN 1251, LDN 1630, NGC 1333, S 68) – jets and outflows – stars formation*

1. Introduction

The protostellar sources are deeply embedded in dense molecular envelopes, giving rise to an active chemistry (Ceccarelli *et al.* 2000). Molecular differentiation in starless cores is established observationally (*e.g.*, Bergin *et al.* 2002, Bergin and Tafalla 2007). During this cold phase preceding the formation of stellar objects, molecules freeze-out onto dust grains, forming H_2O -dominated ice mantles mixed with other less-abundant species. The low temperature and disappearance of most molecules, especially CO, from the gas-phase trigger a peculiar chemistry leading to high abundances of deuterated species. Nitrogen-bearing species, ammonia in particular, and deuterated species do not seem to participate in this freeze-out (Crapsi *et al.* 2007). Chemical calculations (*e.g.*, Walmsley *et al.* 2004, Flower *et al.* 2004, Aikawa *et al.* 2005), suggest that at densities in excess of 10^6 cm^{-3} even the N-bearing species should eventually condense onto grain mantles. Under such “complete freeze-out” conditions, the H_3^+ ion and its deuterated isotopologues: H_2D^+ , D_2H^+ and D_3^+ (Phillips and Vastel 2003, Roberts *et al.* 2003, Vastel *et al.* 2004) become the only tracers of molecular hydrogen.

The discovery of multiply-deuterated molecules (Roueff *et al.* 2000, Ceccarelli 2002, Millar 2005) and in particular triply-deuterated ammonia, ND_3 (Lis *et al.* 2002b, van der Tak *et al.* 2002), has had important ramifications for low-temperature ion-molecule chemistry. Ion-molecule reactions in the gas-phase (Brown and Millar 1989) and reactions on the grain surfaces (Tielens 1983) are the two possible mechanisms responsible for deuterium enrichments in heavy molecules. The discussion of the respective contributions of grain and gas-phase processes in the deuteration of various interstellar molecules is active and no definite solution is yet available. For instance ammonia deuteration is straightforward to understand in the framework of gas-phase chemistry (Roueff *et al.* 2005) but recent laboratory experiment by Fedoseev *et al.* (2015) suggests that formation of ammonia and its deuterated isotopologues through successive addition of hydrogen and deuterium atoms in CO-rich interstellar ice analogues is also efficient at temperature below 15 K. That is why finding optimum tracers of the densest regions, in the immediate vicinity of newly-forming stars, is of utmost importance for understanding the initial stages of the star-formation process. Thanks to the depletion and deuteration processes, deuterated molecules are of particular interest. It is therefore important to study and understand their distribution in the ISM.

We know that high deuteration levels are present in dense, cold prestellar cores (*e.g.*, Vastel *et al.* 2006, Pagani *et al.* 2007) where depletion is rampant. However, high abundances of deuterated species are also observed in sources such as L1689N. The combined single-dish and interferometric observations of the prestellar core in L1689N presented by Lis *et al.* (2016) show clear evidence of an interaction between the prestellar core seen in the dust continuum and line emission of deuterated molecular tracers, notably NH_2D , ND_3 and DCN , and molecular outflow emanating from the nearby solar-type protostar IRAS 16293. Lis *et al.* (2002a, 2016) argued that slow C-type shocks may produce conditions favorable deuterium fractionation reactions in star forming regions.

The goal of this paper is to determine whether similar interactions as in L1689N source take place in other nearby star-forming regions, by comparing the spatial distribution of deuterated species, as traced by the DCO^+ emission, with the H_2 column density distribution traced by the dust continuum emission and the high-velocity CO emission tracing the outflow activity. The summary of available data for each target source is given and compared with results from this work in Section 3, followed by a discussion and a summary in Section 4.

2. Observations

The DCO^+ (3–2) rotational transition at 216.112 GHz and the CO (2–1) transition at 230.538 GHz presented here were observed in 2002–2007 using the 230 GHz facility receiver and spectrometers of Caltech Submillimeter Observatory (CSO) on Mauna Kea, Hawaii, as backups to various high-frequency programs. The data were taken in weather conditions with the 225 GHz zenith opacity of ≈ 0.1 – 0.2 .

The CSO beam size at 230 GHz is $\approx 30''$ and the main beam efficiency is $\approx 60\%$. All maps were taken in the on-the-fly mode, and the deep integrations in the beam-switched mode with a secondary chopper throw of $240''$. The velocity resolution of the high-resolution CSO spectrometer at the frequencies studied here is ≈ 0.15 km/s. The $350\ \mu\text{m}$ continuum observations were carried out in 2003 using the SHARC II bolometer camera. The weather conditions were characterized by the 225 GHz zenith opacity of ≈ 0.05 and the SHARC II beam size at $350\ \mu\text{m}$ is $\approx 8''$.

3. Results for Individual Sources

3.1. Barnard 1

Barnard 1 is a nearby (230 pc, Černis and Straizys 2003) star-forming region in the Perseus Molecular Cloud, one of five nearby star-forming clouds mapped by IRAC and MIPS as a part of the Spitzer Legacy program “c2d” (Evans *et al.* 2003). IC 348 and NGC 1333 are the best studied star-forming clusters in this region, but ongoing star formation is occurring throughout the cloud (*e.g.*, Jørgensen *et al.* 2006, Rebull *et al.* 2007).

The distribution of the (sub)millimeter dust continuum emission has been mapped by Walawender *et al.* (2005), Hatchell *et al.* (2005) and Enoch *et al.* (2006). Walawender *et al.* (2005) identify 12 dust cores in the B1 cluster. The best studied ones are B1-a, B1-b (N and S), B1-c, and B1-d (Hirano *et al.* 1999, Matthews and Wilson 2002, Walawender *et al.* 2005, Hiramatsu *et al.* 2010, Gerin *et al.* 2015) – see Table 1.

Table 1

YSOs and starless cores within the mapped region B1

Source	Outflow (y/n)	Class	Ref.
B1-a /SMM 6 / IRAS 03301+3057	y	I	Hirano <i>et al.</i> (1999)
B1-bS /SMM 1	y	0/FHSC?	Hirano and Liu (2014)
B1-bN /SMM 1	y	0/FHSC	Gerin <i>et al.</i> (2015)
B1-c /SMM 2	y	0	Hirano <i>et al.</i> (1999)
B1-d /SMM 3	y?	0	Hirano <i>et al.</i> (1999)
B1-SMM 11	y	I	Hirano <i>et al.</i> (1999)

In order to study how outflows from protostars influence of the parent molecular cloud we have observed the Barnard 1 in the CO (2–1) and DCO⁺ (3–2) lines. The integrated line intensity¹ of the DCO⁺ (3–2) emission in B1 is shown in Fig. 1 (color image and yellow contours). The blue and red solid contours outline the distribution of high-velocity CO (2–1) emission.

¹The integrated intensity is expressed as the brightness temperature (in Kelvin) integrated over the radial velocity [km/s] variation encompassed by the emission line profile.

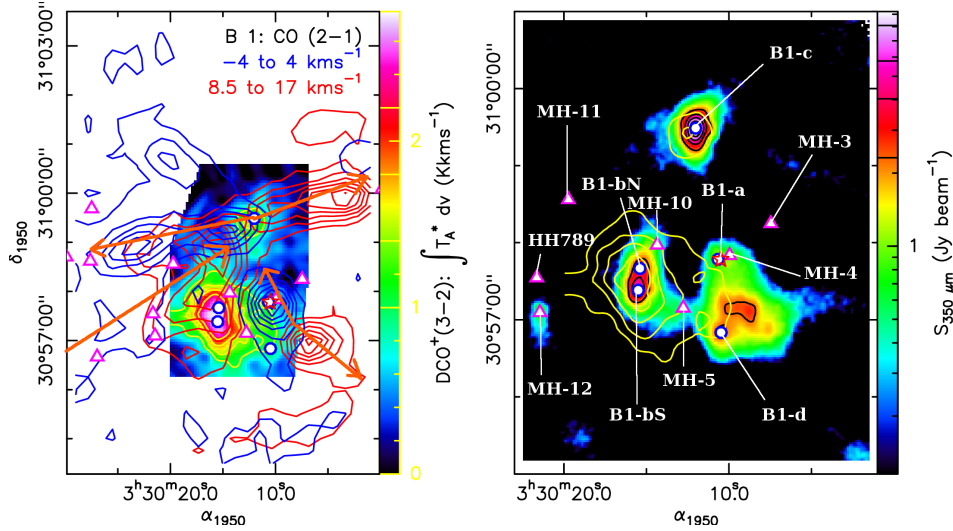


Fig. 1. *Left*: Integrated intensity of DCO^+ (3–2) emission in Barnard 1 (color image and yellow contours) with overlaid contours of high-velocity CO (2–1) emission. Velocity ranges for the blue-shifted and red-shifted emission (blue and red contours respectively) are -4 km/s to 4 km/s and 8.5 km/s to 17 km/s, respectively. Contour levels for DCO^+ are 1 K km/s to 2.5 K km/s, with an interval of 0.5 K km/s. For CO, contour levels are 4 K km/s to 16 K km/s with an interval of 4 K km/s. Arrows show the directions of the outflows. *Right*: Distribution of the $350\ \mu\text{m}$ dust continuum emission (color image and black contours) with overlaid yellow contours of DCO^+ (3–2) emission. Red star marks the location of IRAS 03301+3057. Magenta triangles mark locations of HH objects (Walawender *et al.* 2005) and blue circles mark compact continuum sources B1-a to d (Hirano *et al.* 1999, Hatchell *et al.* 2005).

At least three molecular outflows can be identified in this region. The YSO in the submillimeter clump SMM 2 (also referred as B1-c) is a driving source of the most prominent outflow that is extending along the E-W direction. The extend of the westward redshifted component is $120''$ (0.13 pc, Walawender *et al.* 2005). The other bipolar outflow from protostar, hosts in the submillimeter clump SMM 6 (also referred as B1-a), is more compact. The blueshifted emission is slightly extended ($40''$, 0.04 pc) to N-E, and there is a redshifted component which peaks at $65''$ (0.07 pc) S-E of SMM 6. B1-a appears to power a string of H_2 knots to the West, designated as MH 4 and MH 3. The SMM 3 clump (also referred as B1-d) lies in the confused region and it is difficult to confidently associate any shocks with this source (Hiramatsu *et al.* 2010). The MH 5 shock, however, lies nearby and its morphology suggests that Barnard 1-d may be the source of the roughly N–S outflow. The SMM 1 clump (also referred as B1-b) appears to be more quiet, although its western edge is interacting with an outflow that is possibly arising from sources B1-a or B1-d (Hatchell *et al.* 2007). The eastern edge of this core is interacting with the western, blueshifted lobe of the giant outflow from Class I YSO in SMM 11 clump. In the H_2 image, the western lobe of the SMM 11 outflow extends to MH 10 and MH 3 (Walawender *et al.* 2009).

The B1-b core (in SMM 1) contains two submillimetre/millimeter continuum source B1-bN and B1-bS. The SEDs and the outflow properties suggest that B1-bN and B1-bS are in earlier evolutionary stage than the Class 0 stars *e.g.*, the first hydrostatic core (FHSC, Hirano and Liu 2014, Gerin *et al.* 2015).

The lobe of the SMM 11 outflow encompasses the main DCO^+ peak which is associated with B1-b. Additionally, Barnard 1-b shows the high values of the deuterium fractions. The emission of multiply deuterated molecules, such as ND_3 (Lis *et al.* 2002b) and D_2CS (Marcelino *et al.* 2005) was observed. The secondary peak of DCO^+ to the North is associated with B1-c and the next is associated with B1-a and B1-d.

3.2. NGC 1333

The source NGC 1333 (distance 235 pc, Hirota *et al.* 2008) is the next star-forming region in the Perseus Molecular Cloud – Table 2 and Fig. 2 show the distribution of the DCO^+ (3–2) emission in NGC 1333 (color image and yellow contours) with overlaid red and blue contours of high-velocity CO emission.

Table 2

YSOs and starless cores within the mapped region NGC 1333

Source	Outflow (y/n)	Class	Ref.
IRAS 4A	y	0	Hatchell <i>et al.</i> (2007)
IRAS 4B	y	0	Hatchell <i>et al.</i> (2007)
IRAS 4C	y?	0/FHSC	Koumpia <i>et al.</i> (2017)
IRAS 2A	y	0	Hatchell <i>et al.</i> (2007)
IRAS 2B	y	I	Hatchell <i>et al.</i> (2007)
SVS 13A	y	I	Hatchell <i>et al.</i> (2007)
SVS 13B	y	0	Hatchell <i>et al.</i> (2007)
SK 14	y	0	Hatchell <i>et al.</i> (2007)
SK 15	y?	I	Hatchell <i>et al.</i> (2007)
SK 16	y?	S	Hatchell <i>et al.</i> (2007)

The best know outflow in this region is powered by SVS 13 (A) source, located at the center of symmetry between the lobes. It is associated with Herbig-Haro objects: HH 7-11. This most prominent feature shows a series of high-velocity, blueshifted knots. The chain of high-velocity peaks follows a wavy, sinusoidal pattern, indicating a strongly precessing outflow (Hodapp and Chini 2014). In the S-E, the narrow but extended blue- and red- outflows lobes is associated to the binary source IRAS 4A (Tobin *et al.* 2016). The next two perpendicular outflows, directed N-S and E-W, both originating from IRAS 2A (binary source). The almost parallel bipolar outflow (toward N-S) is associated with IRAS 2B (Plunkett *et al.* 2013).

The main and bright DCO^+ peak is at the edge of the blue lobe of the powerful molecular outflow produced by SVS 13 (A) which coincides with SK 16 a starless region (Sandell and Knee 2001). We do not observe the dust continuum peak close to this region. The bright emission of DCO^+ , coinciding with lobes of high-velocity CO emission rather than dust continuum peaks, marking the locations of embedded protostars Lis *et al.* (2016). The second, bright DCO^+ ridge is located in close proximity of IRAS 4A where ND_3 was first detected (van der Tak *et al.* 2002).

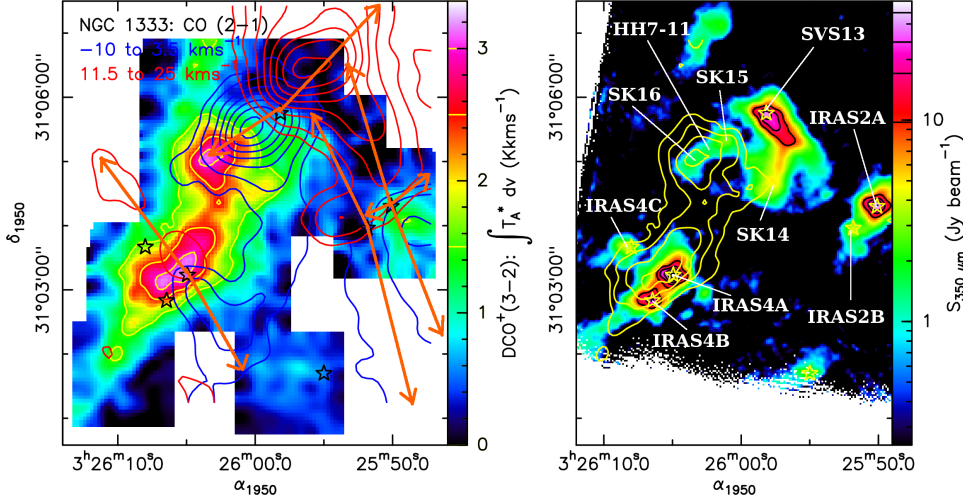


Fig. 2. *Left*: Integrated intensity of DCO^+ (3–2) emission in NGC 1333 (color image and yellow contours) with overlaid contours of high-velocity CO (2–1) emission. Velocity ranges for the blue-shifted and red-shifted emission (blue and red contours respectively) are -10 km/s to 3.5 km/s and 11.5 km/s to 25 km/s, respectively. Contour levels for DCO^+ are 0.5 K km/s to 1.4 K km/s, with an interval of 0.3 K km/s. For CO, contour levels are 4.5 K km/s to 10.5 K km/s with an interval of 1.5 K km/s. Arrows show the directions of the outflows. *Right*: Distribution of the $350\ \mu\text{m}$ dust continuum emission (color image and black contours) with overlaid yellow contours of DCO^+ (3–2) emission.

3.3. LDN 1251

LDN 1251B is located at 300 ± 50 pc (Kun and Prusti 1993) and lies within LDN 1251E, the densest C^{18}O core in LDN 1251 cloud (Sato *et al.* 1994). LDN 1251B harbors a small group of starless and protostellar objects (Table 3). Fig. 3 shows the distribution of the DCO^+ (3–2) emission in LDN 1251B (color image and yellow contours) with overlaid red and blue contours of high-velocity CO emission.

The IRS 1 source is the most luminous object. The IRS 2 protostar is located to the S-E and the IRS 4 Young Stellar Object to the West of IRS 1. The 1.3 mm dust continuum observations of L 1251B with the SMA (Lee *et al.* 2006) reveals two starless objects named as SMA-N (the northern one) and SMA-S (the southern one). The sources: IRS 1, IRS 2, IRS 4 (probably even SMA-S) all have outflows, some of which interact with each other. If SMA-S indeed has an outflow, it may harbor

Table 3

YSOs and starless cores within the mapped region LDN 1251

Source	Outflow (y/n)	Class	Ref.
IRS 1	y	0/I	Lee <i>et al.</i> (2007)
IRS 2	y	0/I	Lee <i>et al.</i> (2007)
IRS 3	n	II	Lee <i>et al.</i> (2007)
IRS 4	y	0/I	Lee <i>et al.</i> (2007)
IRS 5	n	II	Lee <i>et al.</i> (2007)
SMA-N	n	–	Lee <i>et al.</i> (2007)
SMA-S	y?	0?	Lee <i>et al.</i> (2007)

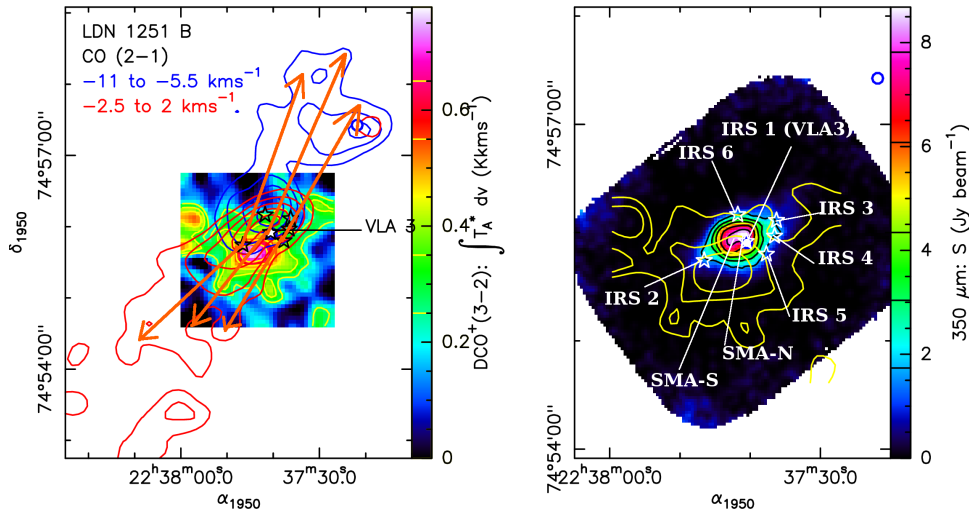


Fig. 3. *Left*: Integrated intensity of DCO^+ (3–2) emission in LDN 1251 (color image and yellow contours) with overlaid contours of high-velocity CO (2–1) emission. Velocity ranges for the blue-shifted and red-shifted emission (blue and red contours respectively) are -11.0 km/s to 5.5 km/s and -2.5 km/s to 2.0 km/s , respectively. Contour levels for DCO^+ are 0.5 K km/s to 1.4 K km/s , with an interval of 0.3 K km/s . For CO, contour levels are 4.5 K km/s to 10.5 K km/s with an interval of 1.5 K km/s . Arrows show the directions of the outflows. *Right*: Distribution of the $350 \mu\text{m}$ dust continuum emission (color image and black contours) with overlaid yellow contours of DCO^+ (3–2) emission.

a very low luminosity protostellar object. The significant outflow appears to be associated with IRS 1 with blueshifted emission to the N-W and redshifted emission to the S-E. This emission, however, may also include a component from SMA-S. For IRS 2, a redshifted feature extends to its S-E and the blueshifted emission lies in a NW-SE direction as red-shifted emission from IRS 1.

The main and bright DCO^+ peak is encompassed by the red-shifted outflows lobes and it is offset to the South with respect to the dust continuum peak.

3.4. LDN 1630

The LDN 1630 (distance 400 pc, Anthony-Twarog 1982) is the southern part of the Orion B giant molecular cloud complex associated with young stellar objects (YSOs) – Table 4. Fig. 4 shows the distribution of the DCO^+ (3–2) emission in LDN 1630 (color image and yellow contours) with overlaid red and blue contours of the high-velocity CO emission.

Table 4

YSOs and starless cores within the mapped region LDN 1630

Source	Outflow (y/n)	Class	Ref.
IRAS 26IR	y	I	Phillips <i>et al.</i> (2001)
SSV 59	y	I	Phillips <i>et al.</i> (2001)
HH 25 MMS	y	0	Phillips <i>et al.</i> (2001)
SSV 61	n	II/T Tau	Phillips <i>et al.</i> (2001)
HH 24 MMS	y	0	Phillips <i>et al.</i> (2001)
SSV 63 E/W	y	I	Phillips <i>et al.</i> (2001)

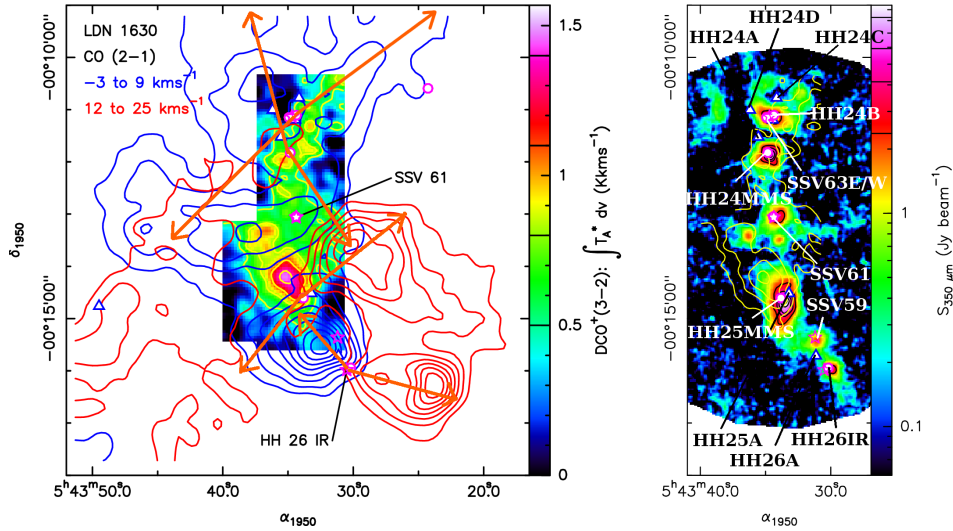


Fig. 4. *Left*: Integrated intensity of DCO^+ (3–2) emission in LDN 1630 (color image and yellow contours) with overlaid contours of high-velocity CO (2–1) emission. Velocity ranges for the blue-shifted and red-shifted emission (blue and red contours respectively) are -3 km/s to 9 km/s and 12 km/s to 25 km/s, respectively. Contour levels for DCO^+ are 0.5 K km/s to 1.4 K km/s, with an interval of 0.3 K km/s. For CO, contour levels are 8 K km/s to 43 K km/s, with an interval of 5 K km/s. Symbols mark locations of embedded infrared continuum sources (stars), HH sources (triangles), and compact VLA sources (circles). Arrows show the directions of the outflows. *Right*: Distribution of the $350\ \mu\text{m}$ dust continuum emission (color image and black contours) with overlaid yellow contours of DCO^+ (3–2) emission.

This field is centred on the very young source HH 25MMS (Gibb and Davis 1998) and contains the infrared objects SSV 59 and HH 26 IR (Davis *et al.* 1997). The HH 26IR is the source of the significant outflow with blueshifted emission to the N-E and redshifted emission to the S-W. The next outflow is centered on HH 25MMS, although the blue-shifted emission is confused with the lobe of the HH 26IR flow. The source SSV 59, which also drives a molecular outflow (Gibb and Davis 1998) makes this region more complex. The HH 24 region is well known as a site of very dynamic outflow activity. This region is also complicated because of confusion from SSV 63 jets and compactness of the HH 24MMS outflow.

The first DCO^+ peak is located to the East of the source HH 25MMS, at the ridge of the two outflows and is encompassed by the blue-shifted lobe of HH 26IR. The next peak is close to SSV 63 source. A curious point is that the radio continuum source and origin for the HH 25MMS molecular outflow is not coincident with the submillimetre continuum peak, being offset by $\approx 6''$ in declination. If genuine, this observation may indicate the presence of a second submillimetre source which may be younger than HH 25MMS (on account of there being no observable outflow, Phillips and Little 2000).

3.5. LDN 1641

LDN 1641 is at a distance of 460 pc (Hester *et al.* 1998) and it is known as a region of low- and intermediate-mass star-forming region of the Orion A cloud South of the Orion Nebula Cluster (ONC). Table 5 contains YSOs and starless cores within the mapped region. Fig. 5 shows the distribution of the DCO^+ (3–2) emission in LDN 1641 (color image and yellow contours) with overlaid red and blue contours of high-velocity CO emission. The study by Moro-Martin *et al.* (1999) suggests the existence of four molecular outflows in the region: (a) a molecular outflow associated with the optical bipolar system HH 1-2 driven by VLA 1, (b) an outflow driven by HH 147MMS, which excites the HH 147 optical flow, (c) an outflow powered by VLA 2, which drives the HH 144 optical flow, and (d) an outflow powered by VLA 3. The latter, N-S outflow is clearly outlined in the

Table 5

YSOs and starless cores within the mapped region LDN 1641

Source	Outflow (y/n)	Class	Ref.
VLA 1	y	0	Cernicharo <i>et al.</i> (2000)
VLA 2	y	0	Cernicharo <i>et al.</i> (2000)
VLA 3	y	I	Cernicharo <i>et al.</i> (2000)
VLA 4	n	I	Cernicharo <i>et al.</i> (2000)
C-S Star	y	T Tauri	Cernicharo <i>et al.</i> (2000)
HH 147 MMS	y	I	Cernicharo <i>et al.</i> (2000)

data of Correia *et al.* (1997). The HH 147 and VLA 3 outflows are clearly seen in our lower angular resolution data.

The DCO^+ is located to the West of the red lobe of the VLA 3 outflow, near the edge of the redshifted high-velocity emission. The source driving the HH 1–2 flow is the embedded object VLA 1 (Rodríguez *et al.* 1990), which powers a highly collimated atomic/ionic jet that interacts with the surrounding medium. Another source, VLA 2, also very young and only a few arc seconds from VLA 1, drives an additional bipolar outflow nearly perpendicular to that emerging from VLA1. The DCO^+ emission peaks to the S-E of the VLA 3 source. The second DCO^+ peak is close to the VLA 1 + VLA 2.

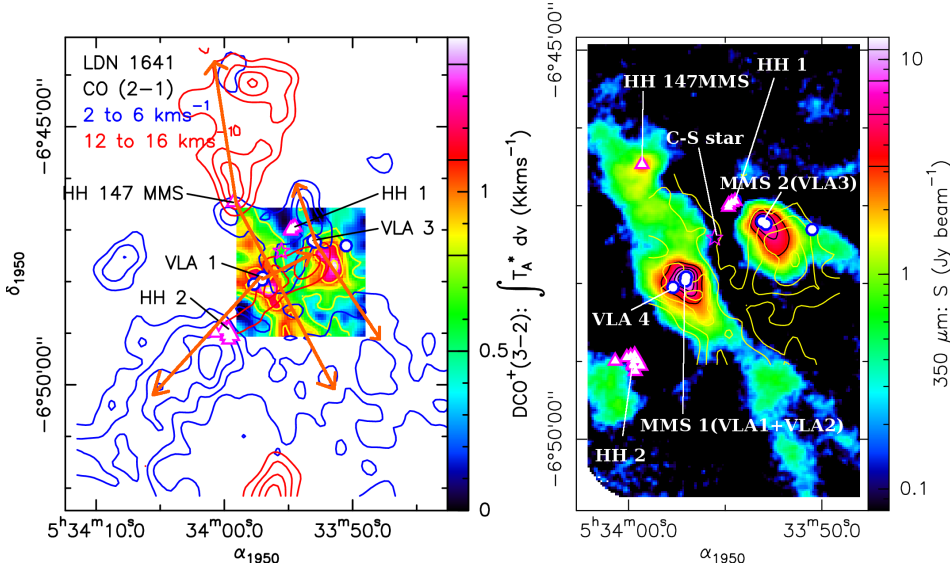


Fig. 5. *Left*: Integrated intensity of DCO^+ (3–2) emission in LDN 1641 (color image and yellow contours) with overlaid contours of high-velocity CO (2–1) emission. Velocity ranges for the blue-shifted and red-shifted emission (blue and red contours respectively) are 2 km/s to 6 km/s and 12 km/s to 16 km/s, respectively. Contour levels for DCO^+ are 1.5 K km/s to 3 K km/s, with an interval of 0.5 K km/s. For CO, contour levels are 5, 10, 20, ... 60 K km/s. Stars mark locations of embedded infrared continuum sources. Arrows show the directions of the outflows. *Right*: Distribution of the 350 μm dust continuum emission (color image and black contours) with overlaid yellow contours of DCO^+ (3–2) emission.

3.6. S 68

The Serpens cloud core is a much-studied region of low-mass star formation located at a distance of 230 pc (Eiroa *et al.* 2008). Fig. 6 shows the integrated line intensity of the DCO^+ (3–2) emission in S 68 (color image and yellow contours) with overlaid red and blue contours of the high-velocity CO emission.

The Serpens central cloud core reveal two “clusters” of embedded young stellar objects separated NW-SE by roughly 200'' (0.2 pc) (Casali *et al.* 1993), Table 6. The CO (2–1) velocity structure is extremely complex and identifying outflows

Table 6

YSOs and starless cores within the mapped region S 68

Source	Outflow (y/n)	Class	Ref.
MMS 1 /FIRS 1	y	0	Eiroa <i>et al.</i> (2008)
SMM 2	y	0/I	Dionatos <i>et al.</i> (2010)
SMM 3	y	0/I	Dionatos <i>et al.</i> (2010)
SMM 4	y	0	Eiroa <i>et al.</i> (2008)
SMM 5	y	0/I	Dionatos <i>et al.</i> (2010)
SMM 6	y	0/I	Dionatos <i>et al.</i> (2010)
SMM 9 /S 68N	y	0/I	Dionatos <i>et al.</i> (2010)
SMM 10	y	0/I	Dionatos <i>et al.</i> (2010)
SMM 11	y	0/I	Dionatos <i>et al.</i> (2010)

from the CO emission alone is extremely difficult. Specifically around objects: SMM 6, 3 and 4, in the centre of the map, at least two overlapping outflows can be seen. The blue-shifted contours show two peaks, one at the SMM 4 clump and one around the clumps: SMM 6 and SMM 3. Also at least four distinct red-shifted lobes are seen: one to the East of SMM3, one to the N-E of SMM6, one to the West of SMM1, and one to the South and West of SMM4 and SMM2. However,

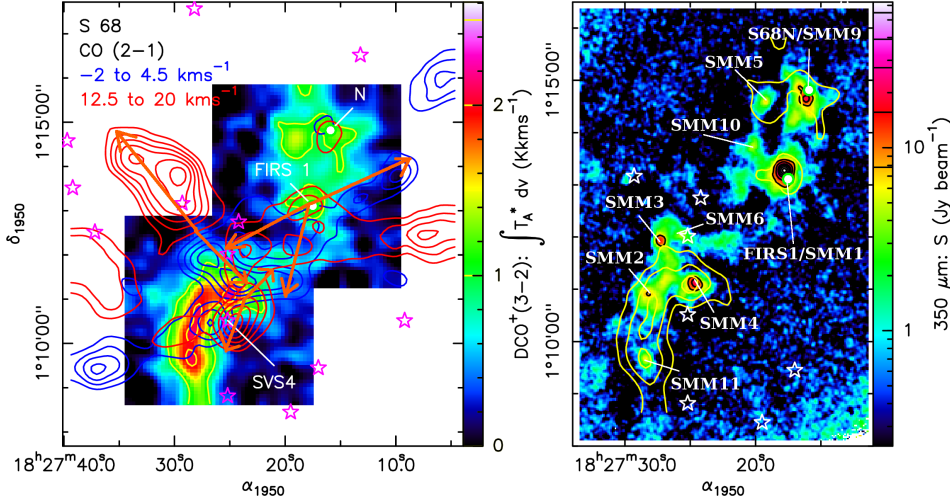


Fig. 6. *Left*: Integrated intensity of DCO^+ (3–2) emission in S 68 (color image and yellow contours) with overlaid contours of high-velocity CO (2–1) emission. Velocity ranges for the blue-shifted and red-shifted emission (blue and red contours respectively) are -2 km/s to 4.5 km/s and 12.5 km/s to 20 km/s, respectively. Contour levels for DCO^+ are 1.5 K km to 3 K km/s, with an interval of 0.5 K km/s. For CO, contour levels are $5, 10, 20 \dots 60$ K km/s. Stars mark locations of embedded infrared continuum sources. Arrows show the directions of the outflows. *Right*: Distribution of the $350 \mu\text{m}$ dust continuum emission (color image and black contours) with overlaid yellow contours of DCO^+ (3–2) emission.

corresponding the blueshifted lobes that may form a bipolar flow are seen to be less distinct. There is one blue-shifted lobe to the West of SMM1. In the vicinity of SMM4, blueshifted emission occurs to the North of SMM4 and to the South and East of SMM2.

The main DCO^+ peak lies between the SMM 6 and SMM 4 sources in a very confused region with the overlapping lobes, at the edge of the bow shock from FIRS 1 (Dionatos *et al.* 2010).

4. Discussion and Summary

According to current theory of low-mass star formation, the first object to be formed in the collapse of the prestellar cores is the first hydrostatic core (FHSC). The important theoretical prediction of the FHSC stage is the presence of compact, slow, and poorly collimated outflow (Hennebelle and Fromang 2008, Machida 2014). When the protostar is formed starts driving a high-velocity (optical) jet which is enclosed by a low-velocity (molecular) outflow with a wide opening angle (Arce and Goodman 2002, Velusamy *et al.* 2007).

The impact of the ejected material on the surrounding cloud causes shock fronts which play a crucial role in the chemical evolution of star-forming clouds because they induce large variations of temperature and density in the surrounding medium (Arce *et al.* 2007). Lis *et al.* (2002, 2016) argued that slow C-type shocks may produce conditions favorable deuterium fractionation reactions in star forming regions by (i) increasing the gas volume density and thus shortening the depletion and gas-phase reactions time scale. The shock-compressed, dense gas cools efficiently to low temperature which sets the initial conditions for gas-phase chemistry to be re-established at a much higher density compared to the pre-shock gas. The gas-phase chemistry may thus subsequently drive up the abundances of deuterated molecules species or (ii) evaporating the grain mantle material that is released into gas-phase. In this case, CO would also be released into the gas-phase resulting in a quick destruction of at least deuterated ions. This could thus be a rather short-lived phase in the evolution of a dense core, overrun by an outflow.

An example of a molecule that arises in the gas-phase deuteration process associated with shocks is DCO^+ . An enhancement of DCO^+ abundance requires an enhancement of H_2D^+ abundance and presence of CO in the gas-phase since it is produced through reaction: $\text{H}_2\text{D}^+ + \text{CO} \rightarrow \text{DCO}^+ + \text{H}_2$. H_2D^+ is enhanced in very cold conditions (≈ 20 K). Under the observed conditions CO freezes out though. To explain the observed DCO^+ abundance enhancement toward the shock position we conclude that this emission is dominated by deuterated species originally formed in the gas-phase after removal of CO from grains at low kinetic temperature (< 20 K). Such release of CO into the gas-phase at such low temperatures can occur during the passage of shock waves. This process may be especially efficient close to the jet impact region. Thus the DCO^+ emission possibly delineates inter-

action regions between the outflows and nearby pre-stellar cores. On the other hand DCO^+ may also form independently of H_2D^+ through gas-phase reactions with CH_2D^+ . This primary ion is mainly formed by: $\text{CH}_3^+ + \text{HD} \rightarrow \text{CH}_2\text{D}^+ + \text{H}_2 + 654 \text{ K}$ and the CH_2D^+ can become enhanced even at temperatures as high as 300 K (Roueff *et al.* 2013). The shock-compressed, dense gas cools efficiently and under warmer conditions ($T > 50 \text{ K}$) are active following reactions: $\text{CH}_2\text{D}^+ + \text{O} \rightarrow \text{DCO}^+ + \text{H}_2$ and $\text{CH}_4\text{D}^+ + \text{CO} \rightarrow \text{DCO}^+ + \text{CH}_4$.

We studied the morphology and kinematics of the dense molecular gas in several low-mass star-forming regions: B1, NGC 1333, LDN 1630, LDN 1641, LDN 1251, S 68. Maps of the DCO^+ (3–2), CO (2–1) transitions, and 350 μm dust continuum emission were obtained using the facility instruments of the Caltech Submillimeter Observatory.

Interferometric observations of Bernard 1 b reveal that this compact core hosts two young stellar objects: B1b-N and B1b-S (Huang and Hirano 2013). These sources are proposed as the first hydrostatic core (Pezzuto *et al.* 2012, Gerin *et al.* 2015) and the compact outflow is associated with B1b-S. From the chemical point of view B1b is characterized by a rich chemistry and additionally, B1 b shows a high degree of deuterium fractionation and has been associated with first detection of multiply deuterated molecules such as ND_3 (Lis *et al.* 2002b) or D_2CS (Marcelino *et al.* 2005). The emission of the DCO^+ is concentrated in the elongated filaments that contain B1b-N and B1b-S. On its eastern side B1b is impacted by the pronounced outflow associated with Class I source, hosted in SMM 11 clump. The B1b source has been previously interacting with the shock associated with the red lobe of this outflow. The outflows are energetically important and provide sufficient energy to sustain turbulence early in the protocluster formation process, without disrupting the entire cluster. The level of turbulence in B1 is higher than in some other cores: L 1544, TCM-1 or L 134 N (Fuente 2016). Sputtering induced by collision may be efficient in this turbulence environment to erode the icy mantle and release to the gas-phase deuterated species (among others) that were formed earlier, either on the gas-phase and then depleted onto dust grain or formed directly on dust grain surface (*e.g.*, ND_3), during the cold cloud collapse phase (Cernicharo 2012). On the other hand the interaction of the compact outflow associated with B1b-S with the surrounding material could enhance the DCO^+ abundance through release CO from grain mantles and reaction with H_2D^+ ion.

NGC 1333 IRAS 4 is the second region with the maximum of DCO^+ emission in close vicinity of compact cores which host Class 0 protostars and also in the proximity of the more evolved protostar SVS 13A with the pronounced outflow. Koumpia *et al.* (2017) found higher DCO^+ abundance around the surrounding gas covering the outflow toward the North of IRAS 4A and it reflects the strong deuteration occurring at those early embedded stages of star formation. van der Tak *et al.* (2002) detected the ND_3 species toward the DCO^+ peak. To explain the observed DCO^+ abundance toward the shock position we conclude that this emission

is dominated by deuterated species originally formed in the gas-phase after the removal from grains at low gas kinetic temperature during the passage of a shock wave.

As mentioned earlier on, the high deuteration levels require a low temperature, high density and consequently high CO depletion. Such conditions are found in isolated prestellar cores which are characterized by a centrally peaked density distribution that can be traced well by dust continuum emission. However our map of NGC 1333 (SK16 region) does not reveal any bright compact dust continuum source. SK 16 is impacted by the outflow associated with SVS 13A, Class I protostar. The shock-compressed, dense gas then cools efficiently to low temperatures, and the gas-phase chemistry quickly drives up abundances of deuterated molecular species. The compressed, high-density, cold post-shock gas, is relatively uniformly distributed and not yet fragmenting to form new stars. The emission of DCO^+ is more widespread and not limited to the shock-impact region probably because it could also form via reaction with CH_2D^+ .

The 1.3 mm dust continuum observations of LDN 1251 B with the SMA (Lee *et al.* 2006) reveals two starless objects named as SMA-N (the northern one) and SMA-S (the southern one). If SMA-S indeed has an outflow, it may harbor a very low luminosity protostellar object. The Class 0/I objects in LDN 1251B might help to form new stars of a second generation.

The dust continuum emission is typically taken as a measure of the H_2 column density, indicating the location of the densest central parts of prestellar cores. However, possible variations in the dust temperature may strongly affect the interpretation. While the average dust temperature in a single-dish beam, this may be dominated by the outer surface layers and the dust temperature in the central, most shielded regions may be significant lower (Bacmann *et al.* 2016). That is why it could be a reason of the observed offset between the dust continuum peak and the emission of deuterated molecules tracer DCO^+ . On the other side Roueff *et al.* (2005) pointed out that deuterated molecules *e.g.*, NH_2D and ND_3 emission often does not peak at the location of embedded protostars, but instead at offset positions where outflow interactions may occurs. Such kind of offset is found in the observed regions: LDN 1251, LDN 1630, LDN 1641, S 68. These DCO^+ sources have not been studied in enough detail to determine whether they are true interactions, or whether they in fact harbor prestellar cores, as is the case in L1689N (Lis *et al.* 2016). In summary Lis *et al.* (2016) concluded that the bright DCO^+ emission, assumed to trace cold, dense gas, coinciding with the tips of CO outflow emission rather than the dust continuum peaks, marking the location of embedded protostars. We need observations with higher precision to determine the offset nature in our sources.

Acknowledgements. This research has been supported by NSF grant AST-0540882 to the Caltech Submillimeter Observatory. M.K. would like to thank

Darek Lis, Maryvonne Gerin and Evelyne Roueff for fruitful discussions and a careful reading of the manuscript and the referee for the valuable comments that helped in improving the original manuscript.

REFERENCES

- Aikawa, Y., Herbst, E., Roberts, H., and Caselli, P. 2005, *ApJ*, **620**, 330.
- Anthony-Twarog, B.J. 1982, *AJ*, **87**, 1213.
- Arce, H.G., and Goodman, A.A. 2002, *ApJ*, **575**, 928.
- Arce, H.G., Shepherd, D., Gueth, F., Lee, C.-F., Bachiller, R., Rosen, A., and Beuther, H. 2007, in "Protostars and Planets V", Tucson, AZ, Univ.Arizona Press, p. 245.
- Bacmann, A., Daniel, F., Caselli, P., Ceccarelli, C., et al. 2016, *A&A*, **587**, 26.
- Bergin, E., Alves, J., Huang, T., and Lada, C.J. 2002, *ApJ*, **570**, L101.
- Bergin, E., and Tafalla, M. 2007, *Ann. Rev. Astron. Astrophys.*, **45**, 339.
- Brown, P.D., and Millar, T.J. 1989, *MNRAS*, **237**, 661.
- Casali, M.M., Eiroa, C., and Duncan, W.D. 1993, *A&A*, **275**, 195.
- Ceccarelli, C., Loinard, L., Castets, A., Tielens, A.G.G.M., and Caux, E. 2000, *A&A*, **357**, L9.
- Ceccarelli, C. 2002, *Planetary and Space Science*, **50**, 1267.
- Cernicharo, J., Noriega-Crespo, A., Cesarsky, D., Lefloch, B., González-Alfonso, E., Najarro, F., Dartois, E., and Cabrit, S. 2000, *Science*, **288**, 649.
- Cernicharo, J. 2012, *EAS Publication Series*, **58**, 251.
- Černis, K., and Straizys, V. 2003, *Baltic Astronomy*, **12**, 301.
- Correia, J.C., Griffin, M., and Saraceno, P. 1997, *A&A*, **322**, L25.
- Crapsi, A., Caselli, P., Walmsley, M.C., and Tafalla, M. 2007, *A&A*, **470**, 221.
- Davis, C.J., Ray, T.P., Eisloffel, J., and Corcoran, D. 1997, *A&A*, **324**, 263.
- Dionatos, O., Nisini, B., Cabrit, S., Kristensen, L., and Pineau Des Forêts, G. 2010, *A&A*, **521**, 7.
- Eiroa, C., Djupvik, A.A., and Casali, M.M. 2008, in: "Handbook of Star Forming Regions", Volume II: The Southern Sky ASP Monograph Publications, Ed.B.Reipurth, Vol. 5, p 693.
- Enoch, M.L., et al. 2006, *ApJ*, **638**, 293.
- Evans, N.J., et al. 2003, *PASP*, **115**, 965.
- Fedoseev, G., Ioppolo, S., and Linnartz, H. 2015, *MNRAS*, **446**, 449.
- Flower, D., Pineau Des Forêts, G., and Walmsley, C.M. 2004, *A&A*, **427**, 887.
- Fuente, A., et al. 2016, *A&A*, **593**, 94.
- Gerin, M., Pety, J., Fuente, A., Cernicharo, J., Commerçon, B., and Marcelino, N. 2015, *A&A*, **577**, L2.
- Gibb, A.G., and Davis, C.J. 1998, *MNRAS*, **298**, 644.
- Hatchell, J., Richer, J.S., Fuller, G.A., Quattrough, C.J., Ladd, E.F., and Chandler, C.J. 2005, *A&A*, **440**, 151.
- Hatchell, J., Fuller, G.A., and Richer, J.S. 2007, *A&A*, **472**, 187.
- Hennebelle, P. and Fromang, S. 2008, *A&A*, **477**, 9.
- Hester, J.J., Stapefeldt, K.R., and Scowen, P.A. 1998, *AJ*, **116**, 372.
- Hiramatsu, M., Hirano, N., and Takakuwa, S. 2010, *ApJ*, **712**, 778.
- Hirano, N., Kamazaki, T., Mikami, H., Ohashi, N., and Umemoto, T. 1999, in: "Star Formation 1999", Ed. T.Nakamoto, p. 181.
- Hirano, N., and Liu, F.-c. 2014, *ApJ*, **789**, 50.
- Hirota, T., et al. 2008, *PASJ*, **60**, 37.
- Hodapp, K.W., and Chini, R. 2014, *ApJ*, **794**, 169.
- Huang, Y.-H., and Hirano, N. 2013, *ApJ*, **766**, 131.
- Jørgensen, J.K., et al. 2006, *ApJ*, **645**, 1246.
- Koumpia, E., Semenov, D.A., van der Tak, F.F.S., Boogert, A.C.A., and Caux, E. 2017, *A&A*, **603**, 88.

- Kun, M., and Prusti, T. 1993, *A&A*, **272**, 235.
- Lee, J.-E., *et al.* 2006, *ApJ*, **648**, 491.
- Lee, J.-E., Di Francesco, J., Tyler, L., Evans, N.J., II, and Wu, J. 2007, *ApJ*, **671**, 1748.
- Lis, D.C., Gerin, M., Phillips, T.G., and Motte, F. 2002a, *ApJ*, **569**, 322.
- Lis, D.C., Roueff, E., Gerin, M., Phillips, T.G., Coudert, L.H., van der Tak, F.F.S., and Schilke, P. 2002b, *ApJ*, **571**, L55.
- Lis, D.C., Wootten, H.A., Gerin, M., Pagani, L., Roueff, E., van der Tak, F.F.S., Vastel, C., and Walmsley, C.M. 2016, *ApJ*, **827**, 133.
- Machida, M.N. 2014, *ApJ*, **796**, L17.
- Marcelino, N., Cernicharo, J., Roueff, E., Gerin, M., and Mauersberger, R. 2005, *ApJ*, **620**, 308.
- Matthews, B.C., and Wilson, C.D. 2002, *ApJ*, **574**, 822.
- Millar, T.J. 2005, *Astronomy & Geophysics*, **46**, 29.
- Moro-Martin, A., Cernicharo, J., Noriega-Crespo, A., and Martin-Pintado, J. 1999, *ApJ*, **520**, L111.
- Pagani, L., Bacmann, A., Cabrit, S., and Vastel, C. 2007, *A&A*, **467**, 179.
- Pezzuto, S., *et al.* 2012, *A&A*, **547**, A54.
- Phillips, T.G., and Vastel, C. 2003, in: “Chemistry as a Diagnostic of Star Formation”, Eds. Curry, C.L., and Fich, M., NRC Press, p. 3.
- Phillips, R.R., and Little, L.T. 2000, *MNRAS*, **317**, 179.
- Phillips, R.R., Gibb, A.G., and Little, L.T. 2001, *MNRAS*, **326**, 927.
- Plunkett, A.L., Arce, H.G., Corder, S.A., Mardones, D., Sargent, A.I., and Schnee, S.L. 2013, *ApJ*, **774**, 22.
- Rebull, L.M., *et al.* 2007, *ApJS*, **171**, 447.
- Roberts, H., Herbst, E., and Millar, T.J. 2003, *ApJ*, **591**, L41.
- Rodriguez, L.F., Ho, P.T.P., Torrelles, J.M., Gurriel, S., and Gómez, Y. 1990, *AJ*, **352**, 645.
- Roueff, E., Tiné, S., Coudert, L.H., Gerin, M., and Goldsmith, P.F. 2000, *A&A*, **354**, L63.
- Roueff, E., Lis, D.C., van der Tak, F.F.S., *et al.* 2005, *A&A*, **438**, 585.
- Roueff, E., Gerin, M., Lis, D.C., Wootten, A., Marcelino, N., Cernicharo, J., and Tercero, B. 2013, *Journal of Physical Chemistry*, **117**, 9959.
- Sandell, G., and Knee, L.B.G. 2001, *ApJ*, **546**, L49.
- Sato, F., Mizuno, A., Nagahama, T., Onishi, T., Yonekura, Y., and Fukui, Y. 1994, *ApJ*, **435**, 279.
- Tielens, A.G.G.M. 1983, *A&A*, **119**, 177.
- Tobin, J.J., *et al.* 2016, *ApJ*, **831**, 36.
- van der Tak, F.F.S., Schilke, P., Miller, H.S.P., Lis, D. C., Phillips, T.G., Gerin, M., and Roueff, E. 2002, *A&A*, **388**, L53.
- Vastel, C., Phillips, T.G., Ceccarelli, C., and Pearson, J., 2003, *ApJ*, **593**, L97.
- Vastel, C., Caselli, P., Ceccarelli, C., Phillips, T., Wiedner, M.C., Peng, R., Houde, M., and Dominik, C. 2006, *ApJ*, **645**, 1198.
- Velusamy, T., Langer, W.D., and Marsh, K.A. 2007, *ApJ*, **668**, L159.
- Walawender, J., Bally, J., Kirk, H., and Johnstone, D. 2005, *AJ*, **130**, 1795.
- Walawender, J., Reipurth, and Bally, J. 2009, *AJ*, **137**, 3254.
- Walmsley, C.M., Flower, D.R., Pineau des Forets, G. 2004, *A&A*, **418**, 1035.